ABSTRACT

Title of dissertation: ULTRACOLD MIXTURES OF RUBIDIUM AND YTTERBIUM FOR OPEN QUANTUM SYSTEM ENGINEERING

Creston David Herold,
Doctor of Philosophy, 2014

Dissertation directed by: Dr. James Porto and Professor Steven Rolston
Joint Quantum Institute,
University of Maryland Department of Physics
and
National Institute of Standards and Technology

Exquisite experimental control of quantum systems has led to sharp growth of basic quantum research in recent years. Controlling dissipation has been crucial in producing ultracold, trapped atomic samples. Recent theoretical work has suggested dissipation can be a useful tool for quantum state preparation. Controlling not only how a system interacts with a reservoir, but the ability to engineer the reservoir itself would be a powerful platform for open quantum system research.

Toward this end, we have constructed an apparatus to study ultracold mixtures of rubidium (Rb) and ytterbium (Yb). We have developed a Rb-blind optical lattice at $\lambda_{\text{zero}} = 423.018(7)$ nm, which will enable us to immerse a lattice of Yb atoms (the system) into a Rb BEC (superfluid reservoir). We have produced Bose-Einstein condensates of ^{170}Yb and ^{174}Yb, two of the five bosonic isotopes of Yb, which also has two fermionic isotopes. Flexible optical trapping of Rb and Yb was achieved

with a two-color dipole trap of 532 and 1064 nm, and we observed thermalization in ultracold mixtures of Rb and Yb.

Using the Rb-blind optical lattice, we measured very small light shifts of ^{87}Rb BECs near the λ_{zero} wavelengths adjacent the $6p$ electronic states, through a coherent series of lattice pulses. The positions of the λ_{zero} wavelengths are sensitive to the electric dipole matrix elements between the $5s$ and $6p$ states, and we made the first experimental measurement of their strength. By measuring a light shift, we were not sensitive to excited state branching ratios, and we achieved a precision better than 0.3%.

Ultracold Mixtures of Rubidium and Ytterbium for Open Quantum System Engineering

by

Creston David Herold

Dissertation submitted to the Faculty of the Graduate School of the
University of Maryland, College Park in partial fulfillment
of the requirements for the degree of
Doctor of Philosophy
2014

Advisory Committee:
Professor Steven L. Rolston, Chair/Co-Advisor
Dr. James V. Porto, Co-Chair/Advisor
Professor Christopher Jarzynski
Professor Christopher Monroe
Professor Luis A. Orozco

to CEH

Acknowledgments

This thesis would not have been possible without the contributions of the other graduate students who have worked on this project. Dan Schwartz was instrumental to the construction of the Rb laser systems, the Rb source, and the vacuum chamber. Varun Vaidya built the current control and magnet coil water cooling with a nearly flawless record for leak-free soldering. And in all our subsequent work together, Varun has demonstrated an uncanny ability to seek out and destroy sources of noise, be it on the current supplies, the atomic locks, or the BEC number stability. I have also had the pleasure of working with our postdoc Xiao "Sean" Li. Sean quickly assembled and tested our Yb 2D-MOT design, and he has continued to be a valuable asset to the lab. Jiraphat "Joe" Tiamsuphat has carefully designed and tested many electronic circuits, and I must also thank him for making the many hours spent commiserating over LabVIEW programming more enjoyable.

Many thanks go to the members of the RbLi team, especially Subhadeep De, Dan Campbell, Abby Perry, and Ryan Price, with whom we shared laboratory space, for sharing optics, lasers, and whatever other equipment was needed to keep forward progress; I hope we have been as generous of our time and tools. Similarly, I need to acknowledge the support and assistance of all my colleagues at JQI. We have benefited greatly from uninhibited collaboration: sharing circuits, mechanical designs, simulation and control code, specialized instruments, etc.

Thank you to my parents for nurturing an early love of math and graciously enabling me to attend Williams College where my love of physics took off. While the

entire physics department faculty fostered my new found passion, I am especially grateful to Tiku Majumder and Sarah Bolton for introducing me to atomic and optical physics through both coursework and research.

The mentoring I have received from both Trey and Steve has been exemplary. Their research styles are often complementary: one of many skills, Steve has a knack for judicious application of force, and Trey's methodical approach has quashed numerous stubborn problems with the apparatus. They have both have been a frequent, helpful presence in the lab—which cannot be said of all advisors!—and I thank them for their dedication to my education.

I owe the biggest thanks of all to my wife, Carrie, who has stoically endured these years of graduate school and encouraged me to strike a work-life balance. Without her love and support, I could never have achieved this PhD. Finally, I must thank my daughter, Charlotte, for unconditionally brightening my day regardless on what happened in the lab.

Table of Contents

List of Tables

List of Figures

List of Abbreviations

ac	alternating current
AOM	acousto-optic modulator
AR	anti-reflection
APP	anamorphic prism pair
ASE	amplified spontaneous emission
BEC	Bose-Einstein condensate
BN	beatnote
CCD	charge-coupled device
CF	ConFlat®-compatible
dc	direct current
DDS	direct digital synthesizer
ECDL	extended-cavity diode laser
FBG	fiber-Bragg grating
FSR	free spectral range
FPGA	field-programmable gate array
HCL	hollow-cathode lamp
HDD	hard disk drive
HEPA	high-efficiency particulate absorption
HVAC	heating, ventillation and air conditioning
HWP	half-wave plate
ID	inner diameter
IF	interference filter
JQI	Joint Quantum Institute
Li	lituium
MOT	magneto-optical trap
NA	numerical aperture
NIR	near-infrared
NIST	National Institute of Standards and Technology
NPT	national pipe thread, tapered plumbing thread standard
OFR	optical Feshbach resonance
PBS	polarizing beam splitter
PCB	printed circuit board
PI(D)	proportional-integral(-derivative)
PLL	phase-locked loop
PM	polarization maintaining
PPLN	periodically poled lithium niobate

PVC	polyvinyl chloride
QWP	quarter-wave plate
Rb	rubidium
rf	radiofrequency
SHG	second-harmonic generation
SSR	solid-state relay
TA	tapered amplifier
TEC	thermoelectric cooler (Peltier)
Ti-sub	titanium sublimation pump
TOF	time-of-flight
TTL	tranisitor-transistor logic
UHV	ultra-high vacuum
UV	ultraviolet
VAV	variable air volume
Yb	ytterbium

Chapter 1: Dissipative Physics with Cold Atomic Mixtures

1.1 Motivation

Since the first demonstrations of Bose-Einstein condensation (BEC) in 1995 [1, 2], the number of experiments on ultracold neutral atoms has grown rapidly. Atoms present well-defined quantum systems with narrow resonances that can be addressed with lasers, and researchers have demonstrated exquisite, coherent control over both their motion and internal degrees of freedom. Nature supplies copious indistinguishable copies, which is critical for observing many-body phenomena predicated on Bose or Fermi statistics. The applications of cold atom experiments are wide-reaching—including metrology, condensed matter physics, particle physics, hydrodynamics, astrophysics, and quantum information—to name a few. With our present work, we would like to add controlled dissipation to this list.

To study coherent quantum phenomena, the system of interest must be well isolated to prevent the environment from disturbing the potentially fragile quantum state. This is one of the primary impediments to building a useful quantum computer. Unwanted coupling to the environment typically causes decoherence within the system. This environment, often described as a bath or reservoir, could be the electro-magnetic spectrum, phonons or incoherent spins within a solid, or even patch potentials on an electrode. Researchers typically work to reduce or eliminate such sources of decoherence thereby preserving the coherent evolution of their system's carefully crafted Hamiltonian. However, control of system-bath interactions

can produce useful dissipation. A well-known example, laser cooling an atomic gas (the system) removes entropy by scattering near-resonant photons off the atoms; dissipation results from the spontaneous emission into unpopulated optical modes of the electro-magnetic spectrum (the reservoir). Our primary research interest is in design and control of novel system-reservoir interactions to explore new and useful applications of open quantum systems.

1.2 Superfluid immersion of atoms in a lattice

Zoller and colleagues published a series of theoretical proposals for engineering quantum baths using an atomic system immersed in a superfluid (BEC) reservoir [3–5]. Their early work demonstrated the possibilities of bath engineering for novel cooling schemes at the single-particle level. Subsequent articles have shown that such a system could be used to explore open quantum systems in very different regimes than available to standard quantum optics experiments. With appropriate system-bath engineering, superfluid immersion may be useful to prepare many-body states and entangled states with very high fidelity [6–9]. In addition, adding spin-orbit coupling to the reservoir BEC [10] could generate chiral (directional) interactions within a one dimensional system [11].

The common thread between these proposals is to draw analogies between laser cooling and quantum optics on the one hand and scattering of cold atoms on the other. The photon reservoir is replaced by excitations in a BEC. For temperatures well below the critical temperature, the condensate is macroscopically occupied and excitations are well approximated by Bogoliubov quasiparticles [12], which are phonons at low energies that transition to a particle-like dispersion at energies above the chemical potential. In each proposal, the system consists of tightly trapped particles, either a single atom or a collection of atoms occupying an optical lattice.

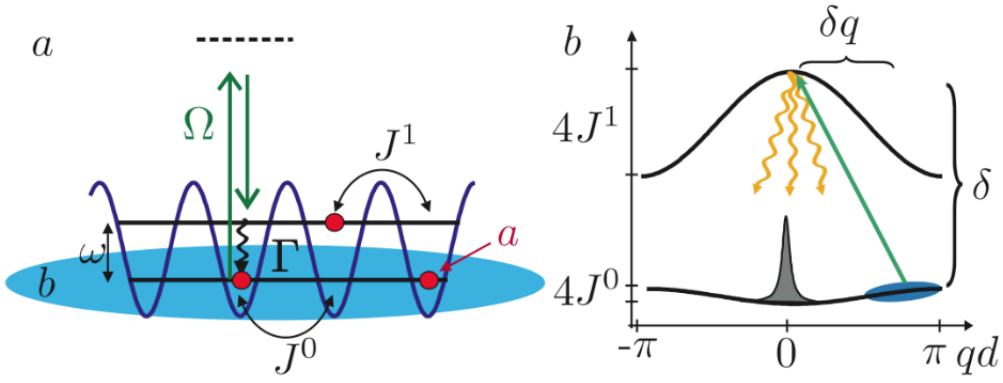

Figure 1.1: Figure from [4] depicting the superfluid immersion cooling scheme. (a) Real space cartoon of a 1D lattice containing a atoms (red) below unit filling immersed in a 3D condensate (blue b atoms). Raman excitation pulses (green) transfer ground band a atoms with large quasimomentum q to the first excited band. Subsequent collisions with b atoms cause decay back to the ground band with rate Γ. (b) Momentum space picture (1st Brillouin zone) of the excitation and decay steps. Repeated application of a series of Raman pulses followed by decay could lead to very narrow quasimomentum distributions for a atoms within the ground band (gray peak).

As a representative example of the required ingredients, I will summarize the key features of the scheme for cooling atoms within the ground band of a lattice [4]. Consider a one-dimensional (1D) lattice of a atoms immersed in a three-dimensional (3D) BEC of b atoms, as pictured in Fig. 1.1. Through careful engineering of the system-bath coupling, one can cool the atoms within the ground band to a temperature[1] well below that of the BEC. Cooling is accomplished through Raman excitation of ground band a atoms at high crystal momentum[2] to the first excited band of the lattice. Collisional interactions with the b atoms cause a atoms to decay back to the ground band, accompanied by the emission of an excitation in the BEC of b atoms. Repeated application of Raman pulses at different non-zero quasimomentum will result in a narrow final quasimomentum distribution for ground band atoms, provided the decay is predominately around $q = 0$. This cooling scheme

[1] Here, temperature is defined by the width of the quasimomentum distribution.

[2] As is common in atomic physics, I tend to use quasimomentum and crystal momentum synonymously. To be clear, the crystal momentum $\mathbf{q} = \hbar\mathbf{k}$ is a quasimomentum formed from the particle's wavevector $\mathbf{k}$ in the lattice.

is "sub-sympathetic" in that the predicted final temperature of a atoms is much colder than the BEC, which need only be cold enough that the excitation modes involved in decay are unoccupied "vacuum modes."

The ultimate temperature achievable in such a scheme will be limited by the total heating rate of lattice atoms. Neglecting technical noise, heating will be caused by photon scattering from the lattice and dipole trap lasers, which can be mitigated by choosing light far off-resonant. Additionally, the bath can heat the system directly. Absorption of energetic phonons from the bath could directly excite ground band atoms to the excited band; this can be suppressed by constantly cooling the reservoir to keep the thermally occupied phonon energies well below the band separation. Reabsorption of spontaneously emitted phonons will be negligible, provided the lattice is sparsely populated. Phonon absorption could also redistribute lattice atoms within the ground band increasing the overall quasimomentum width, however this can be mitigated by properly engineering the reservoir dispersion. The speed of sound of Bogoliubov particles within the BEC increases with b atom density, therefore a sufficiently large speed of sound breaks energy-momentum conservation removing intraband heating to first order (Fig. 1.2). The importance of higher order heating processes is an open question.

1.3 Other physics with ultracold mixtures

Rather than including bath effects on the lattice atoms through the collisionally induced "spontaneous emission" of a bath excitation, one can describe the a atoms as impurities within the condensate, dressed by the Bogoliubov excitations. From this point of view, the dressed impurities are polarons and have an increased effective mass [13–15]; this can have a dramatic effect on the transport of impurities. Even more interesting, the condensate can mediate attractive interactions for both attractive and repulsive bare atoms. The presence of an impurity causes a

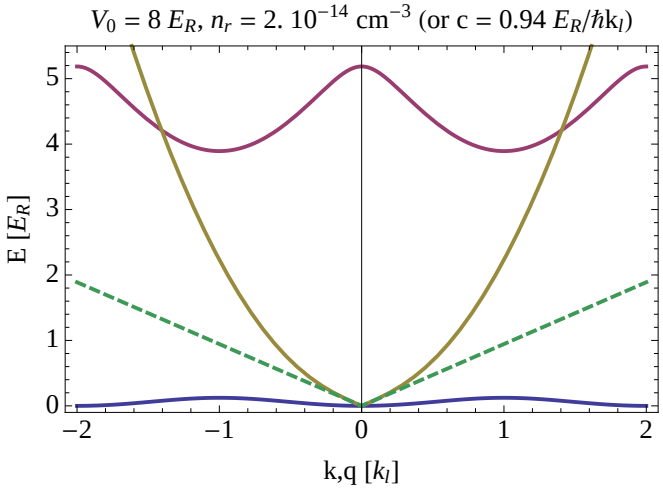

Figure 1.2: Comparison of lattice bands with BEC dispersion. Lattice ground (excited) band energy is in blue (purple) for a depth of 8 recoil energies. The Bogoliubov spectrum for high but realistic density of 2×10^{14} atoms per cm^3 is in yellow, with the linear (phonon-like) dispersion highlighted in green. Here, we've assumed the lattice atom mass is twice that of the BEC atoms; this mass imbalance means BEC excitations are particle-like before the edge of the first Brillouin zone ($q = 1$). The lack of overlap between the Bogoliubov and ground band dispersion shows lattice atoms are decoupled from the BEC (energy and momentum cannot be conserved in a first-order collisional process). Realistic implementations of superfluid immersion cooling require even deeper lattice depths making this decoupling more robust.

deformation of the condensate with characteristic size on the order of the healing length. Provided this deformation spans multiple lattice sites, the modified condensate density will create an attractive potential for nearby impurity atoms.

Mixtures of ultracold atoms also permit the study of cold molecules. Heteronuclear molecules can posses large, permanent electric dipole moments, and atomic calculations predict 0.2 to 1 Debye for rubidium-ytterbium (RbYb) molecules [16, 17]. While unpolarized particles interact with an R^{-6} scaling characteristic of van der Waals interaction, the R^{-3} interaction of dipoles is much longer range enabling studies of strongly interacting models. Furthermore, dipolar scattering can dominate typical s-wave scattering, enabling thermalization of spin-polarized fermions [18]. Basic spectroscopy of bound molecular states, even close to threshold, can refine the interatomic potentials used to calculate molecular properties. Photoassociation, the creation of molecules via resonant optical absorption, requires knowledge of the bound state energies. Additionally, the application of off-resonant laser light detuned near a molecular state can drastically modify the scattering between atoms. Both atomic and molecular states experience an ac Stark shift, also called a light shift, due to the electric field of the laser. Bringing the free atom states near resonance with a molecular state strongly changes the collision dynamics and is a laboratory "knob", commonly referred to as an optical Feshbach resonance (OFR), to tune the effective s-wave scattering length. For many species with a ground state magnetic moment, broad magnetic Feshbach resonances also exist, where the molecular and free atomic states are shifted through the Zeeman effect. (See the excellent review by Julienne [19].) Whereas magnetic Feshbach resonances are long lived, OFRs typically suffer from losses due to spontaneous emission, which can limit experiment times to less than a millisecond. Still, experimental input from molecular spectroscopy will enable theorists to calculate the most promising optical Feshbach resonances for experimental control over interspecies scattering.

Chapter 2: Rubidium and Ytterbium: Atomic Physics

2.1 Choosing the right mixture

Successful demonstration of the lattice cooling scheme introduced in Section 1.2 hinges on the judicious choice of atomic species for our mixture. Below, five key requirements of the scheme are summarized, and we demonstrate why mixtures of rubidium (Rb) and ytterbium (Yb) were selected. We require a:

(i) large, continuously cooled BEC reservoir

(ii) species selective lattice potential for lattice-free bath

(iii) near-degenerate lattice atoms

(iv) lattice ground band isolated from bath through dispersion mismatch

(v) compatible interspecies interactions

For the reservoir, we can readily satisfy (i) with rubidium, specifically ^{87}Rb. With numerous other ^{87}Rb BEC experiments at JQI, we leveraged our institutional knowledge about consistently and efficiently producing BECs with more than 10^6 atoms [20]. Certainly this number may be reduced when preparing a second species as well. Large Rb atom number permits sympathetic cooling of the Yb without exhausting the coolant, and during lattice immersion it allows constant evaporation to maintain a nearly pure BEC despite a moderate heating rate.

Independent control of the system and reservoir is essential to meet (ii). The earliest demonstration of ultracold mixtures used different hyperfine ground states

of the same atom [21]. While it is possible to create a spin-dependent lattice through a vector light shift, collisions and photon scattering can change the hyperfine state thereby allowing atoms to move between the system and reservoir. While this may allow for interesting physics when controlled [22, 23], it also introduces extra experimental complexity when it is not desired. In addition, spin-dependent optical potentials rely on a large fine structure splitting, limiting the laser detuning; as a result large scattering rates plague spin-dependent lattices in Rb. Using distinct atomic species involves significantly more overhead when constructing the experimental apparatus, much of which is detailed in this dissertation. However, the immutable identity of system and reservoir is guaranteed. Independent control of each species is also readily achieved by working at the "tune-out" wavelengths suggested by LeBlanc and Thywissen [24], where the light shift vanishes for one atomic species.[1] These first few wavelengths where Rb polarizability is exactly zero are shown in Fig. 2.1. The first zero at $\approx$ 790 nm will have a very large scattering rate for Rb as previously discussed. However, at the second zero between the $5p$ and $6p$ fine-structure doublets (purple vertical line in Fig. 2.1), the scattering rate is greatly reduced. This is due to the large detuning from the strong $5p$ states and, more importantly, a near-cancellation of the total scattering rate since coherences between $5p$ and $6p$ hyperfine states with the same total angular momentum can interfere destructively. Yb is a good complement to this Rb light shift zero at 423 nm as the lattice will have a reasonable red-detuning from the broad transition at 399 nm (see Fig. 2.2). And, with two-color dipole trapping at 532 and 1064 nm, trap depths for Rb and Yb can be independently controlled [25] as well.

To load only the ground band of the optical lattice, the lattice atoms must be cooled well below the band splitting, or about 1 μK. This can be accomplished in the usual self-evaporative way, or through thermalization with the Rb as both are

[1] Isotopic mixtures are also attractive since the same atomic source provides both species, but no useful "tune-out" wavelengths exist since isotope shifts are only GHz.

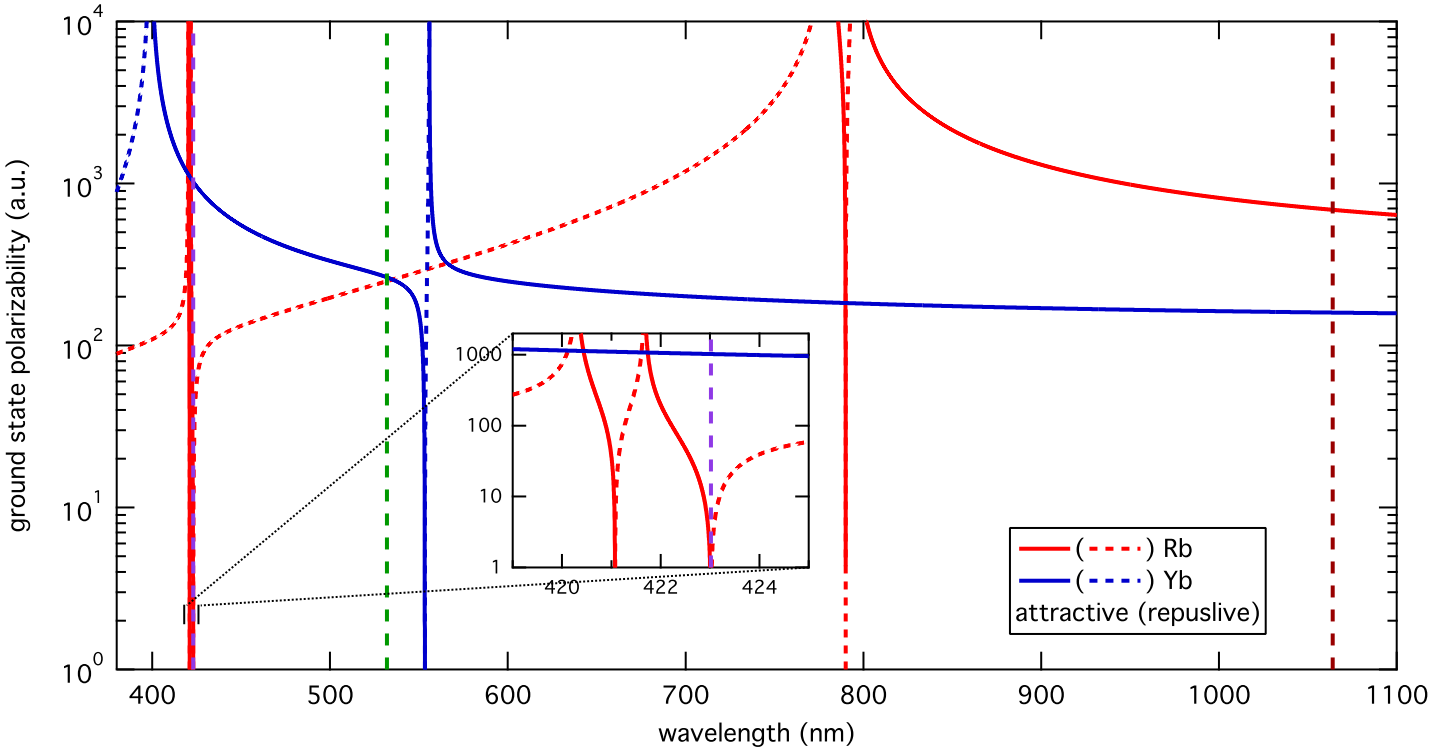

Figure 2.1: The ground state polarizability of Rb (red) and Yb (blue) in atomic units (a_0^3). To display the variation of the polarizability over many decades, the magnitude is plotted with attractive (repulsive) polarizability as a solid (dashed) line. The Yb-only lattice laser at the zero in Rb polarizability (423.018(7) nm) is shown in the inset (purple vertical line); dipole trap colors are shown at 532 nm (green), where the polarizabilities are nearly equal but with opposite sign, and 1064 nm (dark red), which is roughly 4 times stronger for Rb than Yb.

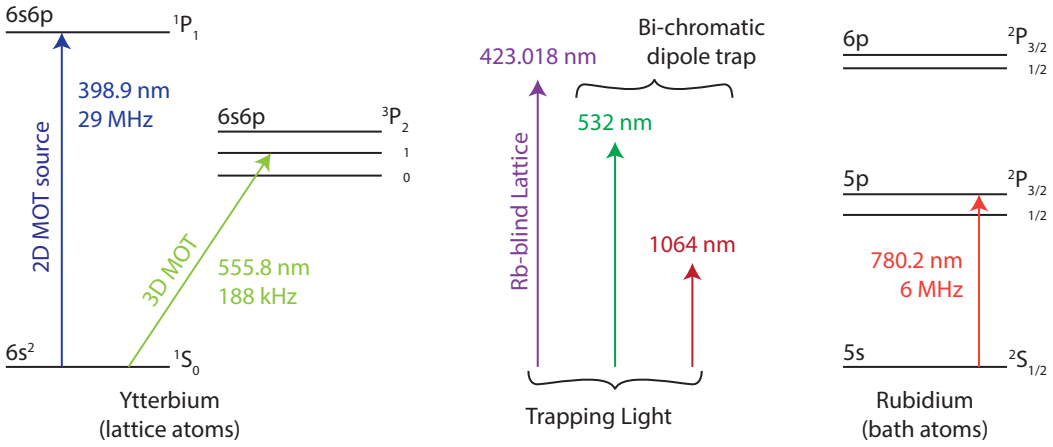

Figure 2.2: Level diagrams showing the relevant transitions in Rb and Yb as well as our chosen dipole trap and lattice wavelengths.

brought to degeneracy together. Most isotopes of ytterbium (Yb) have already been brought to quantum degeneracy, satisfying (iii). Yb is also twice as heavy as Rb so that dispersion mismatch (iv) is easy to achieve for typical densities spanning many orders of magnitude.

Finally, we need compatible interspecies interactions. When our experiment was first proposed in 2006, the Rb-Yb scattering lengths were unknown, except that ^{87}Rb and ^{174}Yb interacted strongly. As demonstrated when determining the scattering lengths for Yb-Yb isotopic combinations, the varying reduced mass is like a "tuneable" parameter [26]. The wide range of Yb isotopes means that Rb-Yb combinations have reduced masses spanning a couple atomic mass units. As a result, we expected that some combination would be likely to provide moderate, useful interactions with Rb. Last year, two groups independently calculated scattering lengths [27,28] from molecular photoassociation spectroscopy by the Göerlitz group [29,30]. Table 2.1 summarizes all Rb and Yb self and interspecies scattering lengths. Unfortunately, many Yb combinations with ^{87}Rb are untenable, making fulfilling (v) somewhat challenging. More details on the best combinations are given at the end of Section 2.4.1.

	Rel. Ab.	I	^{168}Yb	^{170}Yb	^{171}Yb	^{172}Yb	^{173}Yb	^{174}Yb	^{176}Yb		
^{168}Yb	0.13%	0	**252(3)**	117(2)	89(2)	65(2)	39(2)	2(3)	-359(30)		
^{170}Yb	3.0	0		**64(2)**	36(2)	-2(4)	-81(7)	-518(51)	209(2)		
^{171}Yb	14.3	1/2			**-3(4)**	-84(7)	-578(60)	429(13)	142(2)		
^{172}Yb	21.8	0				**-599(64)**	418(13)	200(2)	106(2)		
^{173}Yb	16.1	5/2					**199(2)**	139(2)	80(2)		
^{174}Yb	31.8	0						**105(2)**	54(2)		
^{176}Yb	12.8	0							**-24(4)**	^{85}Rb	^{87}Rb
^{85}Rb	72.2	5/2	230(12)	140(3)	117(2)	100(2)	84(2)	70(2)	39(2)	**-388(3)**	213(7)
^{87}Rb	27.8	3/2	39(2)	-12(3)	-59(4)	-161(11)	-626(88)	880(120)	217(5)		**98.98(4)**

Table 2.1: Yb-Yb [26], Yb-Rb [27], and Rb-Rb [31, 32] scattering lengths (in atomic units of a_0) with 1-σ error. Interspecies scattering lengths were independently calculated in [28], and they agree within the error above. Also, [27] gives the hyperfine correction, which is roughly ten times smaller than the reported error bar. The natural isotopic abundance and nuclear spin I are also given. Pauli exclusion prohibits s-wave scattering for identical fermions; here the scattering length given for fermions is that between different spins in a non-polarized mixture.

2.2 Rubidium

Our group approach to ^{87}Rb condensation is well documented by Lin [20]. The BEC is produced in a hybrid quadrupole plus single dipole beam trap, which defines the apparatus requirements for Rb (detailed discussion in Chapter 3). Instead of repeating the details of laser cooling here (see Metcalf [33] or Pethick and Smith [34] for excellent introductions), key contrasts with Rb are described when introducing the particulars of Yb laser cooling in Section 2.3.

In the interest of documenting all mixtures accessible with our apparatus, it is worth summarizing the difficulties of cooling the other stable isotope, ^{85}Rb. It was first condensed by Cornish *et al.* five years after ^{87}Rb [35] and more recently with a hybrid trap apparatus [36]. While a temperature independent scattering cross section works well for modeling other species, the s-wave scattering of ^{85}Rb goes to zero at a collisional energy of about 350 μK. This is problematic for typical evaporation sequences as this means thermalization is very slow. Combining this with anomalously strong inelastic collisional losses, evaporation is time consuming and inefficient. Ultimately, this limits the size of ^{85}Rb BECs to $< 10^5$ with an experimental cycle time of about 45 s in [36]. Despite these challenges, mixtures with ^{85}Rb are appealing. Moderate, repulsive interactions with ^{173}Yb and ^{174}Yb should allow degenerate mixtures of the most abundant Yb isotopes with ^{85}Rb, unlike with ^{87}Rb. Additionally, ^{85}Rb has a broad magnetic Feshbach resonance at 155 G allowing straightforward modification of Rb interactions [37]. Such control with ^{87}Rb is only possible using a narrow Feshbach resonance at 1007 G [38]. Achieving a field this large with the required stability to address the resonance is challenging.

2.3 Ytterbium

Ytterbium has seven stable isotopes: five spinless bosons and two fermions, whose natural abundances are given in Table 2.1. The Takahashi group created the first Yb BEC in 2003 with the most abundant boson, ^{174}Yb [39]. Ytterbium's two valence electrons make its level structure richer than the hydrogenic alkalis. However, with total electron spin $S = 0$, ground state Yb cannot be magnetically trapped, which also precludes typical rf evaporation. This section highlights the required lasers for cooling and trapping Yb as well as the contrasts with alkali laser cooling. Complete experimental details follow in Sections 3.3, 3.5.2, and 4.5.2.

We use the two laser cooling transitions as shown in Fig. 2.2. The broad $^1S_0$–$^1P_1$ at 398.9 nm excites one $6s$ electron to the $6p$ state without changing its spin, with a natural linewidth $\gamma(^1P_1) = 2\pi \times 29(1)$ MHz [40]. Despite the large capture velocity, MOTs formed on this transition do not work very well as there is significant branching to lower-lying ^3D and ^3P manifolds [41] that limit the lifetime without repumping. Initial cooling of the Yb source in a 2D-MOT as well as absorption imaging are done on this line. Following the Kyoto group [42], we directly load a 556 nm MOT on the $^1S_0$–$^3P_1$ line. This so-called *intercombination* line involves an electronic spin-flip making it spin forbidden to first order. However, LS-coupling is not exact and there is mixing between $^1P_1$ and $^3P_1$ resulting in a linewidth of $\gamma(^3P_1) = 2\pi \times 188(3)$ kHz [43]. To increase the capture velocity, we also artificially broaden the MOT laser. After loading, we turn off the broadening which substantially cools the atoms to 12 μK directly from the MOT, approaching the Doppler temperature $k_B T_D^{(\mathrm{Yb})} = \hbar\gamma(^3P_1)/2 = k_B \times 4.5\ \mu$K. In contrast, the Rb MOT, with its 32 times larger linewidth, has a Doppler-limited temperature of 144 μK. However, the additional hyperfine electronic structure of Rb allows for sub-Doppler cooling, typically to 40 μK with optical molasses. There is no sub-Doppler cooling of bosonic

Yb with its lack of nuclear spin and $J = 0$ ground state. Sub-Doppler cooling in the fermionic isotopes has been observed in Yb [44] as well as the alkaline earth atom strontium, which has a similar electronic structure [45].

The number of other groups working with ultracold Yb has grown steadily in recent years. Takahashi has demonstrated a degenerate Fermi gas with ^{173}Yb [46], optical Feshbach resonances [47] and photoassociation [26] on the 556nm line, metastable $^3P_2$ state trapping [48], isotopic mixtures [49, 50], and even direct evaporation to BEC of the 0.13% abundance ^{168}Yb [51]. NIST has an Yb optical lattice clock [52–54]; Natarajan makes precision measurements with Yb fountains [55–57]; Gupta has a degenerate mixture of Li and Yb [58–62]; and Sengstock demonstrated an Yb BEC apparatus with a 2D-MOT source [63].[2]

2.4 Fundamental mixture physics

Before diving into the detailed description of our apparatus, some fundamental physics of atomic mixtures is discussed. As we will show below, only certain combinations of Rb and Yb will mix at temperatures near degeneracy. This has a profound effect on interspecies thermalization as the overlap between species can be vanishing.

2.4.1 Miscibility

Even at ultracold temperatures, our trapped gasses are very dilute. On the high side of achievable densities, 10^{14} atoms per cm^3 gives a typical separation of 0.5 μm. Indeed, until the atoms' temperature approaches the chemical potential, the gas is essentially ideal. Therefore, any combination of isotopes will mix at high enough temperatures. Close to degeneracy, miscibility depends on the strength of

[2] Dispensers directly load a 2D-MOT in a glass cell with variable gradient magnetic field coils, making the design compatible with both Yb and Rb.

atomic interactions, characterized by their s-wave scattering length a. The stability of mixtures can be determined from simple energetics, and we will show that the condition for boson-boson miscibility involves only scattering lengths. Pauli exclusion makes boson-fermion miscibility depend on the fermion density as well.

Viverit *et al.* use a variational approach to examine the stability of the total energy of a given mixture configuration to changes in the density [64]. The total energy

$$\mathcal{E} = \int d\mathbf{r} E(n_\alpha(\mathbf{r}), n_\beta(\mathbf{r})) \tag{2.1}$$

is a functional of the densities n_α and n_β. The second order variation of $\mathcal{E}$ is minimized provided

$$\frac{\partial \mu_\alpha}{\partial n_\alpha}\frac{\partial \mu_\beta}{\partial n_\beta} - \frac{\partial \mu_\alpha}{\partial n_\beta}\frac{\partial \mu_\beta}{\partial n_\alpha} \geq 0 \tag{2.2}$$

and

$$\frac{\partial \mu_\alpha}{\partial n_\alpha} \geq 0, \ \frac{\partial \mu_\beta}{\partial n_\beta} \geq 0, \tag{2.3}$$

where the chemical potential $\mu_i = \partial E/\partial n_i$ is the derivative of the energy density with respect to atomic density. The conditions in Eq. (2.3) are required for single-species stability against collapse.

For a homogeneous, mixed set of bosons in a box of volume V, assuming mean-field interactions at zero temperature, the energy density,

$$E_{BB} = \frac{\mathcal{E}_{BB}}{V} = \frac{1}{2}g_r n_r^2 + g_{ry} n_r n_y + \frac{1}{2}g_y n_y^2 \tag{2.4}$$

where we've labeled the bosons r (y) for Rb (Yb), and

$$g_{ij} = \frac{2\pi\hbar^2}{\mu_{ij}} a_{ij}, \quad g_i = g_{ii}, \tag{2.5}$$

for reduced mass $\mu_{ij} = m_i m_j/(m_i + m_j)$.[3] The chemical potentials are

$$\mu_r = g_r n_r + g_{ry} n_y, \quad \mu_y^{(B)} = g_y n_y + g_{ry} n_r \tag{2.6}$$

and therefore, applying Eq. (2.2), the boson-boson mixture is stable provided

$$g_{ry}^2 \leq g_r g_y \,. \tag{2.7}$$

This miscibility condition is often given in terms of a instead [65], however with species of unequal mass we cannot simply replace g by a:

$$a_{ry}^2 \leq \frac{\mu_{ry}^2}{\mu_{rr}\mu_{yy}} a_r a_y = \frac{4 m_r m_y}{(m_r + m_y)^2} a_r a_y = \xi a_r a_y \tag{2.8}$$

The factor ξ which is ≤ 1, will reappear when we consider thermalization between species of unequal mass; for RbYb mixtures, $\xi \approx 8/9$ as Yb has about twice the mass of Rb. In effect, the miscibility condition on a is more stringent as the mass imbalance increases.

Eq. (2.7) shows that both repulsive and attractive boson-boson mixtures are stable, provided the interspecies interaction is not too strong. In deriving the condition, we assumed that the only phase present was mixed. To be complete, one must compare the mixed energy to a phase-separated configuration, under the constraints that each phase must have equal pressure and the chemical potentials must support equilibrium [64]. For bosonic mixtures, this leads to the identical condition. The addition of a trapping potential affords for much more complicated topologies [66, 67], and depending on interaction strengths, the minority component may split the majority condensate or be forced to the edge of the trap [68]. However, Eq. (2.7) *still* remains the condition for miscibility.

[3] To distinguish from the chemical potential (μ_α), the reduced mass will always have two labels (μ_{ry}).

Ultracold mixtures of bosons and fermions have a richer phase diagram. Spin-polarized fermions cannot have s-wave collisions due to Pauli exclusion, so their self-scattering length does not appear in the low temperature energetics. Rather than the mean-field self-interaction $g_y n_y$, the chemical potential is now driven by the local Fermi energy $\epsilon_F = A n_F^{2/3}$, with $A = (6\pi^2)^{2/3}\hbar^2/(2m_F)$. This 2/3 power law dependence on density (instead of linear) drastically changes the permitted phases. Again considering a zero temperature mixture in a box as in [64], the energy density is

$$E_{BF} = \frac{1}{2} g_r n_r^2 + g_{ry} n_r n_y + \frac{3}{5} \epsilon_F n_y, \tag{2.9}$$

where the bosons are labeled r and fermions y as only Yb has stable fermionic isotopes. Then the chemical potentials are

$$\mu_r = g_r n_r + g_{ry} n_y, \quad \mu_y^{(F)} = \epsilon_F + g_{ry} n_r \tag{2.10}$$

leading to the stability condition from Eq. (2.2) for a mixed phase:

$$n_y^{1/3} \leq \frac{2}{3} \frac{A g_r}{g_{ry}^2} \tag{2.11}$$

which now depends on the fermion *density*.

Comparing Eq. (2.11) to Eq. (2.7), it is natural to define an effective scattering length for the fermions $\tilde{a}_F \propto n_F^{-1/3}$ as though they were bosons with s-wave scattering. I find this helps with my intuition as it shows that the *larger* the fermion density, the *smaller* its effective self-interaction becomes, eventually making separate boson and fermion phases more favorable. Of course, physically this effective contact interaction is actually due to the fermions' kinetic energy which grows more slowly with density than the mean field boson-fermion interaction.

For repulsive interspecies interactions, $g_{ry} > 0$, full treatment of equilibrium

comparing mixed and separate phases shows it is energetically favorable to separate into a mixed phase and a pure fermion phase as the density approaches the stability limit, Eq. (2.11). And at the highest boson and fermion densities two separate phases also exist. However, for $g_{ry} < 0$ (as is the case for ^{87}Rb and fermionic Yb), the only stable phase is a homogeneous mixture, provided Eq. (2.11) holds. Above these densities, the attractive g_{ry} overwhelms the repulsion of ϵ_F and the fermions collapse,[4] presumably to a density so large mean-field expressions fail. Numeric studies have shown that for harmonically trapped boson-fermion mixtures, Eq. (2.11) is qualitatively correct [70], and we will use it when discussing feasible RbYb mixtures.

Having discussed miscibility for mean-field interactions near zero temperature, we are able to determine which isotopic combinations can form a co-degenerate mixture. Unfortunately, as we will see the majority of combinations of Yb with ^{87}Rb are untenable. Two of the bosonic isotopes, ^{172}Yb and ^{176}Yb, have attractive self-interactions (Table 2.1) and are unstable self-collapse. Numerical integration of the Gross-Pitaevskii equation has shown collapse occurs above a critical condensate number $N_c \approx 0.57 a_{ho}/|a|$ [71, 72], where the harmonic oscillator length $a_{ho} = \sqrt{\hbar/m\bar{\omega}}$ with mean trap frequency $\bar{\omega} = (\omega_x\omega_y\omega_z)^{1/3}$. For a very loose trap frequency $\bar{\omega} = 2\pi \times 10$ Hz, $N_c \approx 1100$ atoms for ^{176}Yb. It may be possible to look at how a second bosonic species could stabilize this collapse [71]. The most abundant isotope, ^{174}Yb is immiscible with ^{87}Rb, exhibiting separation even in a thermal gas [29] and is also known to exhibit large three-body losses, which scale as a^4. Both of the remaining bosonic species are miscible with ^{87}Rb, but with a scattering length of only $-12(3)$ a_0, there are very weak interspecies interactions for ^{170}Yb. The tiny natural abundance of ^{168}Yb (0.13%) makes it difficult to work with, although the scattering lengths are quite favorable. Impressively, the Kyoto

[4] This counterintuitive collapse has been observed experimentally in mixtures of ^{87}Rb and ^{40}K [69].

		^{87}Rb		^{85}Rb
^{168}Yb	✗	miscible, low abundance	✗	miscible for $a_{\mathrm{Rb}} > 235$
^{170}Yb	✗	miscible, small interspecies	✓	miscible for $a_{\mathrm{Rb}} > 345$
^{171}Yb	✓✓	miscible ($n_{\mathrm{Yb}} \lesssim 10^{19}$)	✓	miscible ($n_{\mathrm{Yb}} \lesssim 10^{17}$)
^{172}Yb		✗✗ Yb BEC collapse		
^{173}Yb	✓/ ✗	miscible for $n_{\mathrm{Yb}} \lesssim 5 \times 10^{12}$	✓	miscible ($n_{\mathrm{Yb}} \lesssim 10^{18}$)
^{174}Yb	✗✗	immiscible	✓	miscible ($a_{\mathrm{Rb}} > 53$)
^{176}Yb		✗ Yb BEC collapse		

Table 2.2: Prospects for ultracold mixtures of Rb and Yb. Scattering lengths are in Bohr and densities in cm^{-3}. The number of ✓(✗) are intended to denote how (im)possible each combination is.

group demonstrated direct evaporation to BEC, but the experimental cycle time was nearly two minutes [29].

From Eq. (2.11) the ytterbium density for ^{173}Yb in a mixture with ^{87}Rb is limited to $n_{^{173}\mathrm{Yb}} \lesssim 5 \times 10^{12}$ cm^{-3}. Fermi degeneracy with Yb at this density requires a very weak trap which lowers the Fermi temperature: 10^4 atoms in a trap with $\bar{\omega}$ of $2\pi \times 10$ Hz has $T_F \approx 20$ nK and a peak density of 8×10^{11} cm^{-3}. The enormous interspecies attraction would enable us observe the fermion collapse reported in [69]. Additionally, this density limit will inhibit loading ^{173}Yb into a 423 nm optical lattice via sympathetic cooling with ^{87}Rb as the unit cell volume in a cubic lattice is 10^{14} cm^{-3}. By far, the best combination with ^{87}Rb is ^{171}Yb. With a modest, attractive interspecies scattering length, mixtures will remain miscible over achievable fermion densities. However, even in an unpolarized spin mixture, the ^{171}Yb self interaction is very weak. Table 2.2 summarizes all isotopic combinations including those with ^{85}Rb, where the tunable self-scattering length comes at the cost of slow evaporation and smaller achievable BEC number as discussed in Section 2.2.

2.4.2 Thermalization

Sympathetic cooling—removing entropy from one species by placing it in thermal contact with a colder species—is a powerful tool for bringing difficult to cool

species to degeneracy. With a scattering length consistent with zero, ^{171}Yb must be cooled sympathetically. The rate of energy transfer W from gas 1 to gas 2 is determined by the collision rate, temperature difference, and the mass imbalance between species [73, 74]:

$$W = \Delta E_{1\to 2} \cdot \Gamma_{\text{coll}} = \Big(-\xi k_B \Delta T \Big) \left(\sigma_{12} \bar{v} \int d\mathbf{r} n_1(\mathbf{r}) n_2(\mathbf{r}) \right) \tag{2.12}$$

where, as we have already encountered in Eq. (2.8),

$$\xi = \frac{4 m_1 m_2}{(m_1 + m_2)^2} \tag{2.13}$$

and $\Delta T = T_2 - T_1$. The collision rate, given by the second term in Eq. (2.12), depends on the scattering cross section $\sigma_{12} = 4\pi a_{12}^2$ and

$$\bar{v} = \sqrt{\frac{8 k_B}{\pi} \left(\frac{T_1}{m_1} + \frac{T_2}{m_2} \right)} \tag{2.14}$$

is the mean thermal velocity difference for Maxwell-Boltzmann distributions at T_1 and T_2. Crucially, Γ_{coll} also depends on the overlap between species which is determined by the relative trapping potentials, gravitational sag, and miscibility. For thermalization within a single gas, all particles have the same mass and $\xi = 1$. It is well documented that it takes roughly three collisions per particle for the gas to reach thermal equilibrium for particles of equal mass [75–77]. The factor ξ accounts for the less efficient transfer of energy with mass imbalance so that thermalization now requires $\approx 3/\xi$ collisions or about 3.4 for Rb-Yb mixtures. It is important to note that for some species, the scattering cross section is *not* independent of temperature as assumed here; for example, cesium exhibits a zero-energy resonance in the scattering cross section and requires 10.7 collisions per atom as the majority of collisions are between low energy atoms and do not redistribute energy [78].

The equilibrium temperature, assuming ideal gas behavior, is given by the number-weighted sum of initial temperatures:

$$\overline{T} = \frac{N_1 T_1 + N_2 T_2}{N_1 + N_2} \tag{2.15}$$

And the rate at which this temperature is reached (and $\Delta T \to 0$) is the rate of thermalization

$$\frac{1}{\tau} = \frac{1}{\Delta T}\frac{d(\Delta T)}{dt} = \xi \frac{N_1 + N_2}{3 N_1 N_2}\Gamma_{\text{coll}} \tag{2.16}$$

where the final expression is easily derived from energy conservation[5] and the energy exchange rate Eq. (2.12). In [73], Mosk evaluates the density overlap integral in Eq. (2.12) by making appropriate assumptions about the trapping potential for each species. Therein, the authors assume a harmonic trap $V_i(\mathbf{r}) = (\mathbf{\Omega}_i \cdot \mathbf{r})^2$ for each species where the trap strength of the second species is linearly related to the first so that $\mathbf{\Omega}_2 = \beta \mathbf{\Omega}_1 \equiv \beta \mathbf{\Omega}$; it is useful to note that β^2 is the trap depth ratio of species 2 to species 1. This is a reasonable assumption for two species trapped in a dipole trap, but will not be the case for Rb and Yb in a hybrid trap since the Yb ground state does not have a magnetic moment. Gravitational sag is not included, which is justified if the vertical trap frequency is large enough for each species. These assumptions give

$$\Gamma_{\text{coll}} = \frac{\sigma_{12}\bar{v} N_1 N_2}{(\pi k_B)^{3/2}} \bar{\Omega}^3 \left(T_1 + T_2 \beta^{-2}\right)^{-3/2} \tag{2.17}$$

where the mean trap strength $\bar{\Omega} = (\Omega_x \Omega_y \Omega_z)^{1/3}$. Substituting this and Eq. (2.14) into Eq. (2.16), the thermalization rate is

$$\tau^{-1} = \frac{4(N_1 + N_2)\sigma_{12}\xi \bar{\Omega}^3}{3\pi^2 k_B} \frac{\left(\frac{T_1}{2m_1} + \frac{T_2}{2m_2}\right)^{1/2}}{\left(T_1 + T_2 \beta^{-2}\right)^{3/2}} \tag{2.18}$$

[5]Recall that for a harmonically trapped gas in three dimensions, $U_i = 3 N_i k_B T_i$ since the equipartition theorem states that each particle has energy $k_B T/2$ for each degree of freedom.

In Section 4.5.3 we will specialize this result for the trap geometry in which we have observed interspecies thermalization.

Chapter 3: Design and Construction of the RbYb Apparatus

As the first graduate student on this new project, I started with a completely empty laboratory space. This is the first dissertation on the RbYb apparatus and therefore includes a lot of detail about its design and construction. After describing the vacuum system, the atomic sources are presented, followed by high-current infrastructure, laser systems, the computer control scheme, and finally brief notes on laboratory environment control. Given the level of detail on design and construction, the performance of the atomic sources is included in Chapter 4 along with the discussion of optimized production of ultracold Rb and Yb.

3.1 Main Chamber

Ultracold trapped gasses require ultra-high vacuum (UHV) to prevent collisions with background gas from limiting trap lifetimes. A typical pressure of 3×10^{-11} Torr will give vacuum limited lifetimes on the order of 10 minutes.[1] Achieving pressures this low requires materials with very low out-gassing rates such as most stainless steels, OFHC copper, and certain glasses and ceramics.[2] Connections between vacuum components must be made with metal-to-metal seals, where an annealed copper gasket is compressed between the knife-edges of two Conflat-style (CF) flanges. Careful material preparation and handling is imperative as a stray

[1] Trapped, cold atoms are sensitive pressure sensors; see [79] for a summary of alkali atom loss rates due to hydrogen background pressure.

[2] The LIGO collaboration has required stringent testing of all materials included in their UHV system; their list of allowed and rejected materials is publicly available at https://dcc.ligo.org/LIGO-E960050/public.

fingerprint or hair will severely impact the base pressure achieved. In our experience, most commercial CF parts rated for UHV can be used without additional cleaning.

The central feature of our vacuum apparatus is the trapping region, which commonly consists of either a rectangular glass cell or a stainless steel chamber. A glass cell affords close air-side proximity to the trapped atoms, excellent optical access, and can be nearly non-magnetic. Chambers can be constructed from "non-magnetic" alloys, however machining often leads to a residual magnetization. With our cooling and trapping lasers spanning the visible to near-infrared spectrum, we decided to use a chamber, permitting us to customize the anti-reflection (AR) viewport coatings in each beam direction.

The main chamber (Fig. 3.1) is based on a Kimball Physics Inc. "spherical square" with an 8" spherical inner diameter, 8" CF flanges on top and bottom, and four 4.5" flanges equally spaced around the sides with 2.75" flanges in between. Additionally there are 1.33" CF flanges in a rectangular pattern around each 2.75" flange. Where one 2.75" flange would have been, we had Kimball Physics weld on a 2.5" inner diameter tube with a 4.5" CF flange. This connects to our pumps and increases the conductance over the original 1.9" bore. The pumping setup, shown in Fig. 3.2, consists of a standard 4.5" CF 5-way cross with a titanium sublimation (Ti-sub) pump, 75 L/s sputter ion pump (Gamma Vacuum 75S-CVX-4V-SC-110-N), UHV ionization gauge (Varian UHV-24P), and an all-metal angle valve for connection of the roughing turbo pump (Pfeiffer Vacuum HiCube 80 Eco).

The original ion pump on the main chamber was from Varian (Vacion Plus 55 Starcell), but it had poor magnetic shielding resulting in stray fields at the atoms of more than one Gauss. While this may not seem like a lot, the resulting Zeeman shift for ground state Rb atoms is 1.4 MHz/G or 67 μK/G, which must be considered with final temperatures well below one μK. The shielding on the Gamma Vacuum pumps is well designed, and we swapped pumps while breaking vacuum to install

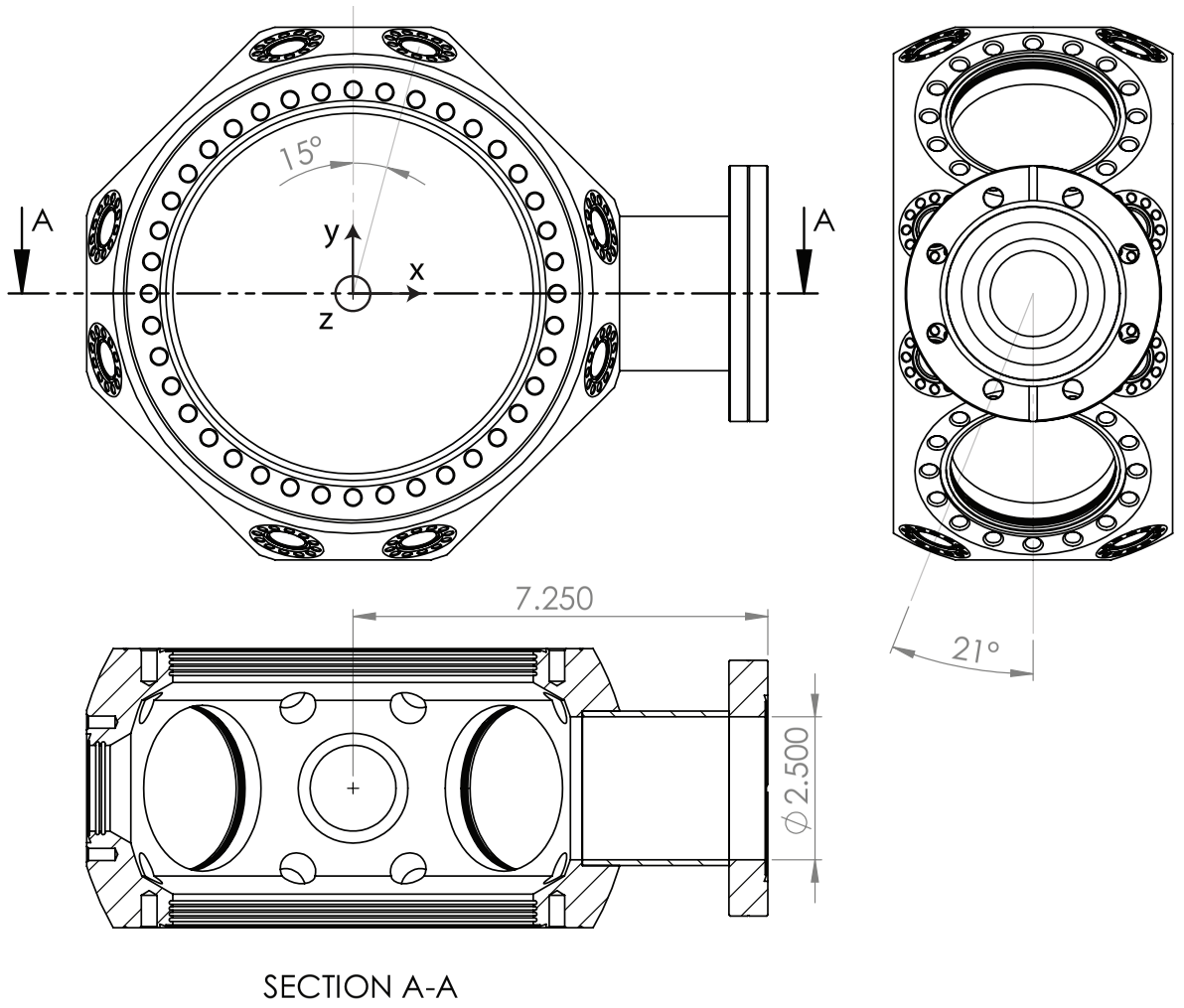

Figure 3.1: Customized main chamber (Kimball Physics MCF800-Cust-G2E5C3A16). Chosen laboratory coordinates are shown as well as polar and azimuthal angles for the mini-viewports.

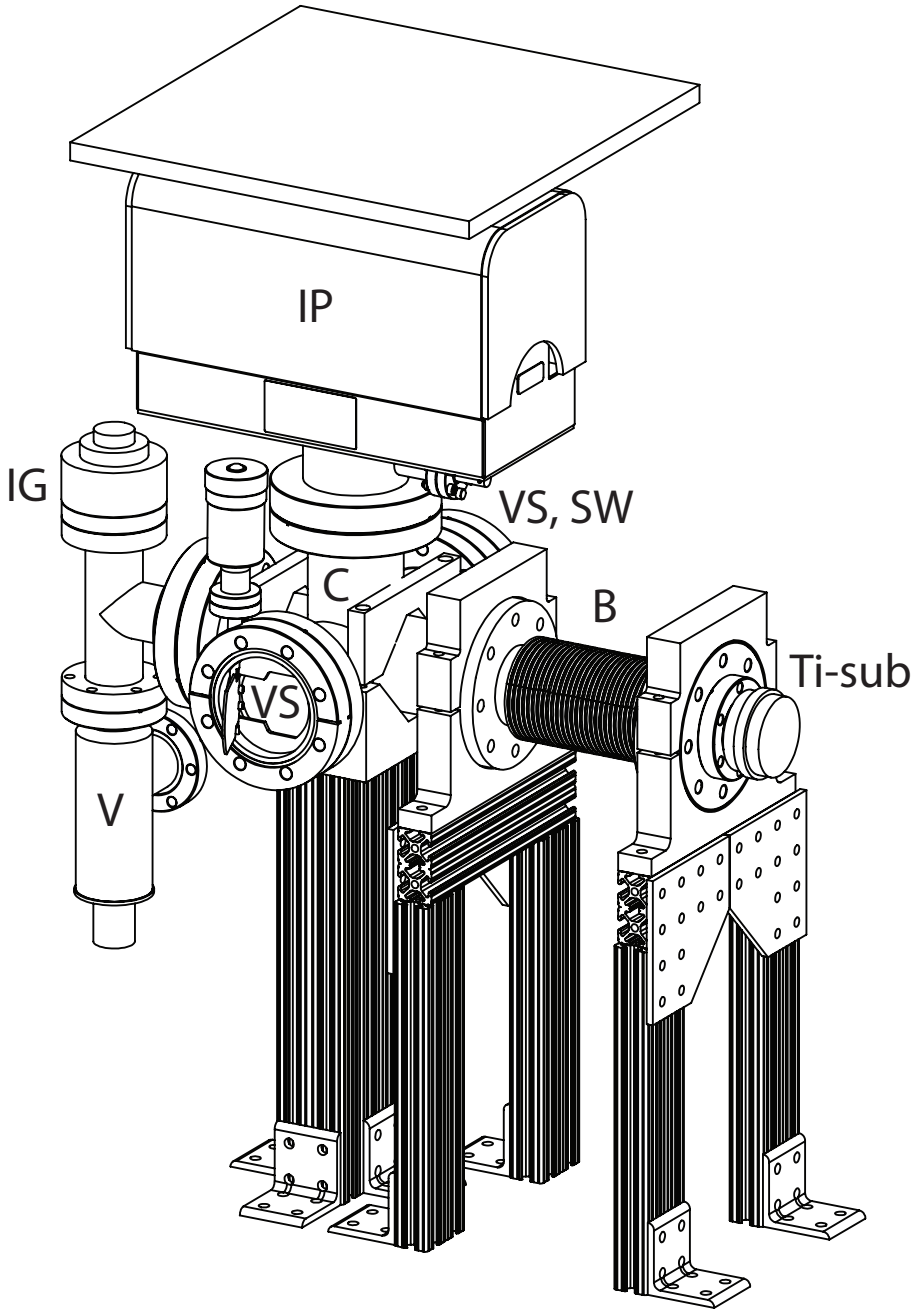

Figure 3.2: Pumping cross assembly. The main chamber attaches, via the 4.5" welded tube, to the front viewport shutter (VS), while the Rb slower beam is input from the back side. The cross (C) is supported by a custom "V-block" attacked to an 80/20 2040 series post, and either side of the bellows (B) is supported with custom flange clamps. Not shown: four threaded rods with nuts on each corner of the clamps allow us to force the bellows into or out of the cross region. *Key*—B: bellows, C: 5-way cross, G: ion gauge, IP: ion pump, SW: Rb slower window, Ti-sub: titanium sublimation pump, V: angle valve, VS: viewport shutter.

the Yb source. We also suspect the extremely poor shielding on the Duniway ion pump attached to the Rb source may be limiting our slower flux, since it produces a 10 G field at the slower entrance. The Ti-sub (Duniway TSP-275-003) is attached to a bellows so that it can be inserted fully into the 5-way cross for more uniform sputtering. Coating the large surface area with a getter material like Ti makes it pump background gas by chemically locking it to the surface upon a collision. Normally, the bellows is stretched, removing the Ti-sub from the Rb slower beam path. The first Ti-sub pump developed a slow leak at one of its metal-ceramic seals on the electrical feedthrough. Suspecting it was caused by mechanical stress from repeatedly connecting and disconnecting the high-current cable, we bought a spare cable and leave it permanently attached to the replacement Ti-sub. Main chamber pressure as low as 3×10^{-11} Torr is maintained for a few months, between Ti-sub firings.

Magnet coils were designed to fit inside custom recessed windows on the 8" flanges (MDC Vacuum/Insulator Seal Inc., Fig. A.1). Minimizing the distance to the atoms means more efficient generation of gradient and bias fields for each Ampere of current. Fig. 3.3 shows a cutaway of the main chamber detailing the recessed windows, quadrupole and bias coils and their mounting structure, as well as the lattice and dipole trapping beam geometry. MOT beams for both Rb and Yb are also sent through the vertical direction and the large 4.5" windows in the horizontal plane, beside the lattice beams. To facilitate optical alignment to the center of the chamber and reduce the total footprint of optomechanical support posts, we placed custom-machined stainless steel "cage washers" (Fig. A.2 and A.3) beneath the vacuum bolts on all of the larger flanges. These washers have #4-40 mounting holes compatible with Thorlabs' 30 and 60 mm cage-rod system, allowing us to directly mount lenses and mirrors to the chamber. Additionally, we designed and machined a set of angled adapters (Fig. A.4), which are attached to the 4.5" washers

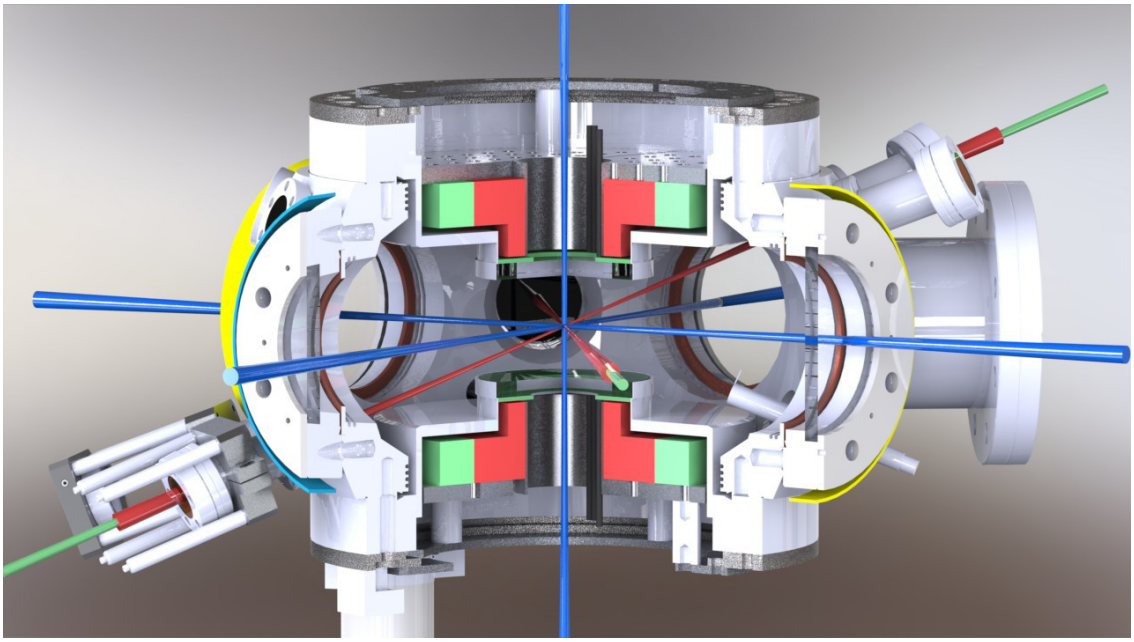

Figure 3.3: Chamber cutaway detailing quadrupole (red) and bias (green) magnet coils within the recessed windows. The rf PCBs are between the magnet coils and the windows. Also shown are optical trapping beams: a mock-up of two-color crossed dipole trap plus 3D 423 nm lattice. MOT beams are not shown, but they are also input through the large windows beside the horizontal lattice beams. The microwave feedthrough is visible inside the chamber on the lower-right side. If shown, the pumping cross (Rb slower) would be on the right (left) side.

and aid in multiplexing MOT and lattice beams in the horizontal direction.

The vacuum viewports were selected to have a minimally magnetic glass-to-metal seal. The majority of the windows on the chamber are MDC Vacuum/Insulator Seal series 97220xx, where the xx denotes the CF flange size. While these appear nearly identical in construction, subsequent windows purchased are expressly labeled as non-magnetic (MDC Vacuum 45002x series).[3] The windows are UV grade fused silica with a 304 stainless steel sleeve and PbAg non-magnetic braze alloy. The recommended maximum bakeout temperature is 200 °C, while the braze alloy melts at 305 °C. Custom dielectric AR coatings were designed and applied by Spectrum Thin Films with mixed results. Despite excellent looking designs, our measurements have shown actual reflectivity varies between 0.2 and 3% depending on the wavelength

[3]These are the only CF windows I have ever found which are specified to be non-magnetic.

and complexity of the requested coating. The coatings and their position on the chamber are diagrammed in Fig. 3.4. Larger than expected reflections necessitated modifying our dipole beam design. Our first 1064 nm dipole trap for Rb was aligned perpendicular to the window, and when observing Kapitza-Dirac diffraction [80] off a 532 nm lattice, there were extra peaks at half the expected momentum, which turned out to be a weak 1064 lattice from a back reflection. Dipole beams are now aligned with about a four degree angle from normal incidence so that reflections miss the atoms. Along the 1.33" (mini-)CF dipole direction, the 0.65" diameter windows are not large enough to allow transmission through the chamber at an angled incidence. Therefore, we designed short adapter nipples with a 5° angle between thier sealing surfaces (Fig. 3.5), which are inserted between the chamber and mini-CF dipole windows, as shown in Fig. 3.4.

Fig. 3.3 also shows the printed circuit boards (PCBs), between the quadrupole coils and the recessed windows, used for radio frequency (rf) control. The board allows full 3D control of the rf polarization through three sets of planar coils (Fig. 3.6), without restricting optical access. A matched pair of PCBs (top and bottom) are driven in series, doubling the rf field for a given current. We found no need to add a capacitive pi-junction, observing that the rf coils installed on our chamber are approximately 50 Ω impedance matched up to about 20 MHz. We also installed a quarter-wavelength microwave antenna roughly fashioned out of a mini-CF coaxial feedthrough. Designed to broadcast microwaves at the Rb ground state hyperfine splitting of 6.834 GHz, the end of the central conductor is bent at ninety degrees and has a length of $\lambda/4 = c/(4 \times 6.834\text{GHz}) \approx 1.1$ cm.

Construction of the magnet coils was challenging. Both the quadrupole and bias coils are wound from Kapton insulated 0.158" square-profile Cu tubing (custom ordered by the group from S&W Wire Company) to allow direct water cooling. Aluminum forms were machined both to support the coils permanently and to assist

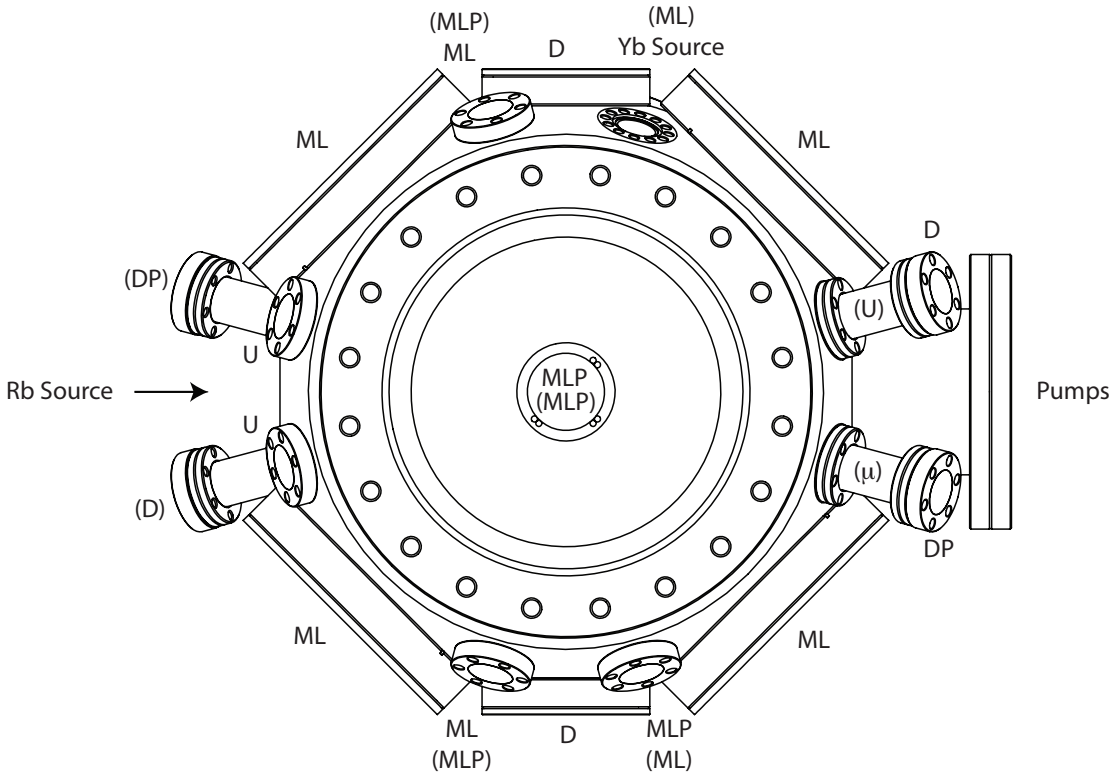

Figure 3.4: Schematic diagram (top view) of AR coatings on the main chamber vacuum windows. Windows are coated on both sides and matched with their opposing partner to reduce back-reflections. *Coating key*—D: dipole trap (532/1064 nm), L: lattice (423 nm), M: MOT (556/780 nm), P: probe (399/780 nm), U: uncoated, μ: microwave feedthrough. Objects on the bottom are labeled in parenthesis. The Rb slower beam window at the end of the pump cross is coated for 780 nm.

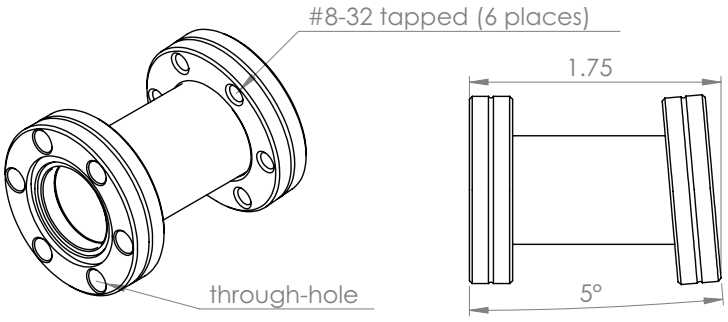

Figure 3.5: Short, angled 1.33" CF adapter nipple to eliminate back-reflection for dipole beams. The part was designed and manufactured by Nor-Cal, to our specifications.

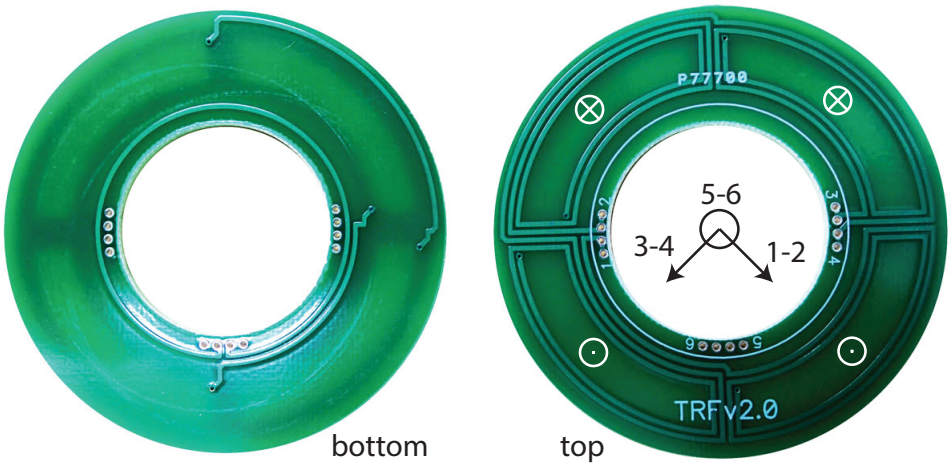

Figure 3.6: PCB for 3D rf drive control. The central loop (left) produces a vertically polarized field, while the vertical component of the paired quadrant-loops cancels to produce a purely horizontal field on axis. The white vector markings indicate the magnetic field in the plane of the PCB, while the black vectors show the field on-axis below the PCB. Note how the linkages between quadrants are paired top-and-bottom to cancel their field effect. Coaxial cable leads are attached at each of the numbered pads.

in the coil winding. The Kapton insulation on the square tubing is thin and easily scratched, so it was imperative to check for shorts while winding. The quadrupole coil consists of two separate coils. The first is two layers of six turns each (2×6) wound on a 1.6" OD form; the second is 4×3, wound around the first. Wound directly around the quadrupole coil, the bias is also 4×3. Each coil was epoxied and allowed to harden under tension before winding the next, and a matched[4] top and bottom set were constructed. To complete the quadrupole and bias coils, the component coils are connected in series (Fig. 3.7) electrically, while cooling water is forced through in parallel.[5] Fine control of constant magnetic fields is accomplished with shim coils, composed of ten turns of 14 gauge kapton-coated wire wound around the 4.5" viewports. Fig. 3.8 shows the geometry of all magnet coils. This figure was

[4]In reality, the top and bottom quadrupole coils are different by roughly one-half turn (out of 24) due to kinks in the square tubing while winding.

[5]Splitting one long coil into two and running cooling water in parallel quadruples the cooling efficiency since twice as much water is in contact with half the heat in each section.

magnet coil	Radia estimate	
quadrupole	0.73	G/cm/A
bias	1.1	G/A
shim 1 & 2	0.29	
z-shim (proposed)	0.70	
quad. as bias	1.61	

Table 3.1: Magnetic field strength produced by each magnet coil for 1 Ampere of current. The quadrupole gradient reported is in the strong direction, along the symmetry axis, and we measured it to be 0.79(2) G/cm/A by balancing gravity for the Rb atoms. While not presently implemented on our apparatus, the ability to reverse the direction of half the quadrupole coil makes a larger bias field, as shown on the last line.

generated with a Mathematica add-on called Radia,[6] with which we estimated the field from each coil. Another useful tool for magnet coil design is a numeric Biot-Savart integration package written by a former NIST postdoc, Michael Johanning, which we used when designing the Rb slower. Table 3.1 compares the estimates to actual values measured with Rb atoms.

The chamber is mounted at a central height of 14.5" above the optical table. Custom breadboard platforms (Vere ALP series) surround the chamber and provide a 2" working optical height (Fig. 3.9). Additionally, there is another breadboard mounted above the chamber which provides space for fiber de-launches for MOT and probe beams. The breadboards are aluminum with a 1" thick honeycombed core for stiffness. The top and bottom plates are both tapped with a 1" grid of 1/4"-20 holes. Unfortunately, the aluminum plates have proved too flexible so that loosening a single neighboring clamping fork will misalign our dipole beam. That said, the honeycomb structure makes the breadboards quite dead to acoustic vibrations, especially compared to the 1/2" solid aluminum breadboards we tried first. Despite the excellent value, I would caution against ordering from Vere. They have been notoriously slow to deliver orders for multiple groups at JQI—two to three

[6]Radia was developed as ESRF, France and is very useful for magnetic design. It is free to download at http://www.esrf.eu/Accelerators/Groups/InsertionDevices/Software/Radia.

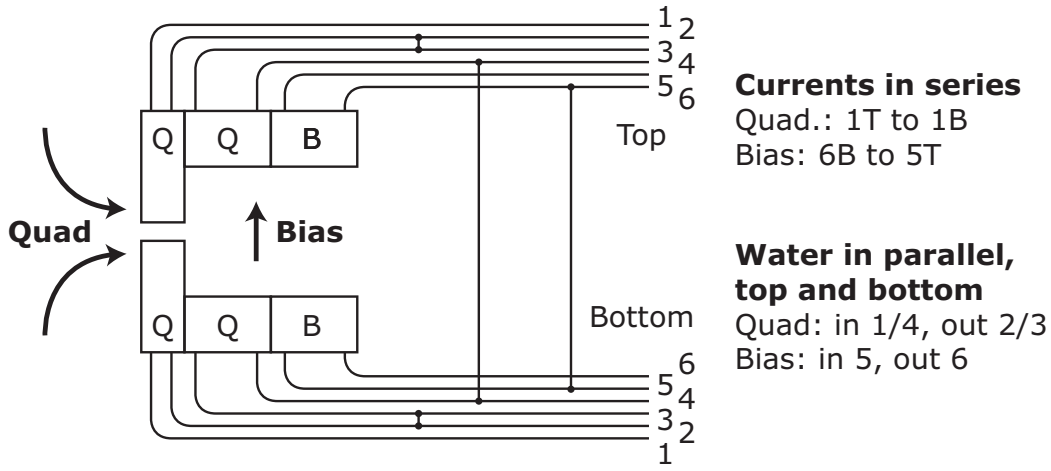

Figure 3.7: Coil leads are labeled from inside out for each set of coils. Pairs of leads were shorted (as diagrammed) by soldering both through a copper block. The resulting magnetic field directions are shown with arrows. A round tube-adapter was soldered to each square wire end, and plumbing connections were made with brass compression fittings.

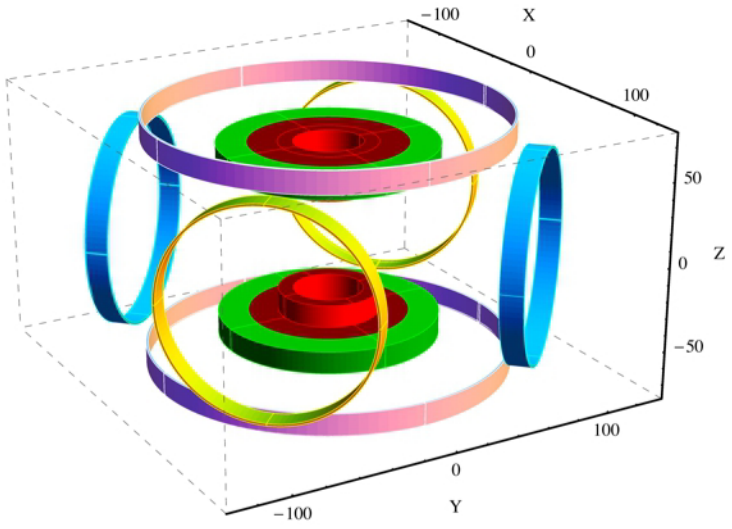

Figure 3.8: Mathematica visualization of magnet coils with the Radia package (axes in mm). In our chosen labratory coordinates, the Rb atomic beam enters from the back (along $\hat{x}$) and gravity is along $-\hat{z}$. *Color code*—red: quadrupole, green: bias, blue: shim 1, yellow: shim 2, purple: z-shim (proposed).

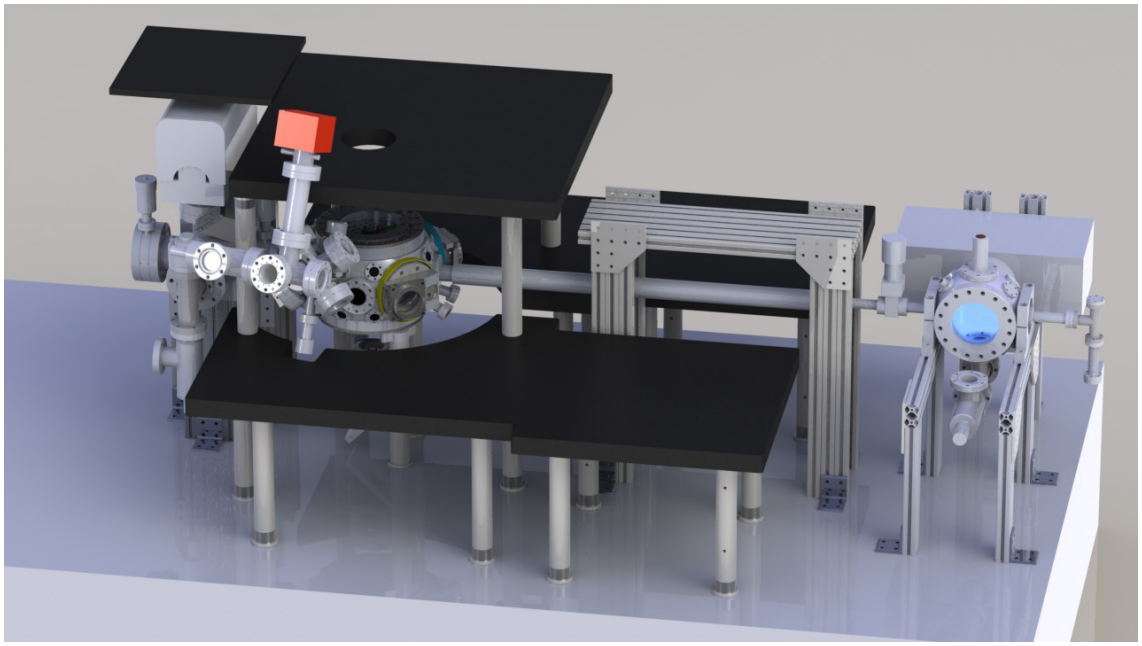

Figure 3.9: Custom breadboards provide working surfaces at chamber height and above.

times the estimated lead time. And in addition to the flexing already mentioned, the flatness of the boards is very poor; most were bowl shaped and freely spin when placed on a truly flat surface.

3.2 Rb source

The Rb source consists of an oven-fed Zeeman slower. The oven chamber (Fig. 3.10) is identical to that described in [20] except for two small differences. First, the ceramic break was replaced with a standard nipple since the actual thermal conduction is comparable. Second, the collimation tube (5 mm ID x 15 cm length) was packed with 15 stainless steel hypodermic needles (Small Parts HTX-19X-06-10, 1.07 mm OD $\times$ 0.89 mm ID $\times$ 15.2 cm length) in an attempt to further reduce the beam divergence. In the kinetic regime, collimation performance is determined by

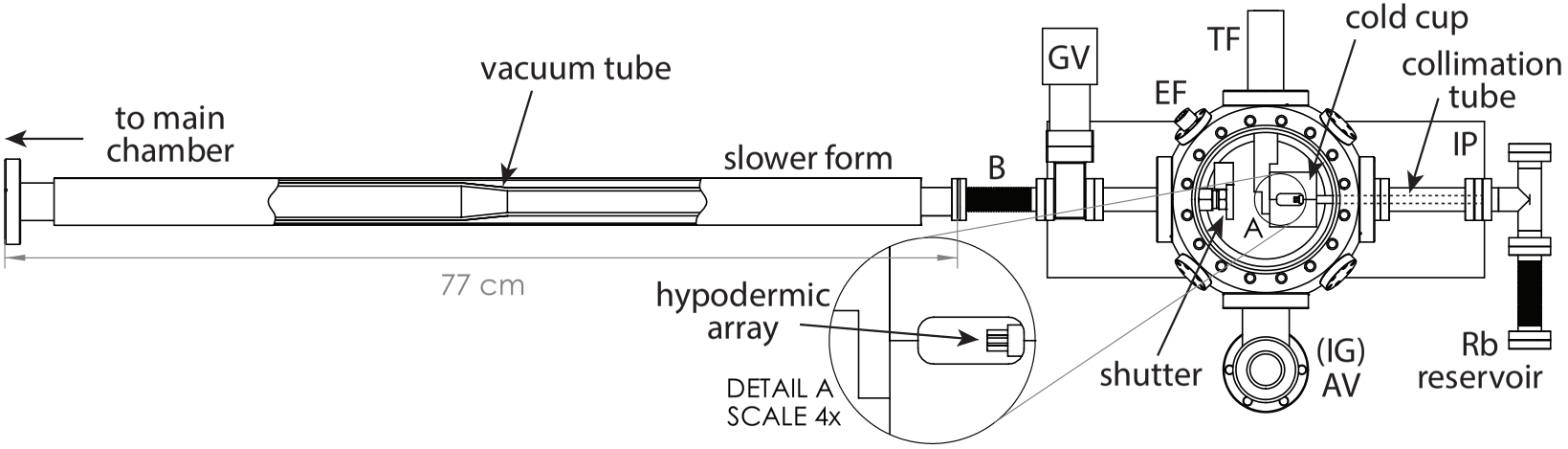

Figure 3.10: Rb source vacuum chamber. On the left, the center of the slower form has been cut away to reveal the diameter reduction in the vacuum tube. The slower tube is attached to the oven with a bellows (B) to relieve mechanical strain. Separate heaters are wrapped around the Rb reservoir and collimation tube and held at 110 and 140 °C, respectively. The length of the collimation tube is shown with a dotted line. *Key*—AV: angle valve, B: bellows, EF: electrical feedthrough for the shutter, GV: gate valve, IG: ion gauge (back), IP: ion pump, TF: thermal feedthrough.

the mean free path between atomic collisions [81]

$$\lambda = \frac{1}{\sqrt{2}n\sigma} = \frac{k_B T}{\sqrt{2}P\sigma}\,, \tag{3.1}$$

where σ is the kinetic collisional cross section, and the density n is determined by temperature T and pressure P of the gas, modeled as ideal. The cross section for Rb was measured by Croucher to be 1397 Å^2 [82]. At a typical Rb oven temperature of 90 °C, the mean free path is about 1.6 cm, placing the collimation tube in the "opaque" regime where $l > \lambda > d$ and collisions along the tube are important. Lucas conveniently presented theory for the effect of a long collimation tube in a universal form applicable for any atom [83], with which we compare our collimation tube for Rb with and without the hypodermics. Approximating the hypodermic array as a set of tubes with negligible transverse extent, the flux and intensity from the array scales linearly with the number of hypodermics without increasing the angular distribution of a single hypodermic significantly. For equal on-axis beam intensity, the hypodermic array will have an angular spread roughly 3 times smaller than the single collimation tube resulting in more efficient use of Rb. Also, the oven pressure at the start of the hypodermics must be higher to achieve the same intensity, requiring a source temperature of 107 °C instead of 90 °C, corresponding to a Rb pressure 3.2 times larger.[7] Such an array will not provide significantly higher on-axis intensity as the tube is already "opaque." The total atomic flux should be roughly 10^{13} atoms per second, or 0.4 g/year for constant operation. Assuming daily operation, the 1 g Rb ampoule (Alfa Aesar 10315) loaded in the oven reservoir should last 5 to 7 years.

The collimation tube is followed by a copper "cold cup." A 3 mm aperture permits the central, well-collimated portion of the Rb beam to enter the slower

[7]While we have not measured the atomic beam profile, the empirically optimized source temperature is 110 °C, consistent with the theory.

tube, while the divergent atoms stick to the cold cup,[8] which is cooled by a two-stage TEC (Custom Thermoelectric 19012-5L31-06CQQ) attached to a thick copper feedthrough (MDC Vacuum 641000) to about -30 °C. Maintaining such a large temperature difference across the TEC dissipates significant heat, which we remove with water cooling. Initially, the TEC was installed in a water block designed to cool PC processors (Swiftech MCW6500-775T), however the weakly-barbed plumbing fittings proved unreliable and resulted in a major flood overnight during a planned power outage. The power was restored before the cooling water pump was restarted. Without water cooling, the TEC quickly heated up, and it melted the plastic tubing, spraying water everywhere once the water pump was on. The cooling water loop provided by the university has an automatic refill valve, and flooding continued until it was discovered. To prevent further risk of flooding, the barbed fittings and plastic tubing were replaced with modified compression fittings and copper tubing.[9] Additionally, the current driver for the TEC was interlocked so that a solid-state relay interrupts the current if the cold plate temperature rises above a chosen value. As with all interlocks, one must carefully examine failure modes. Here they include: temperature sensor malfunction, loss of power to the monitor circuit, disconnection of the relay switch signal, etc. The relay is only closed if the temperature monitor circuit is powered.

To prevent the Rb beam from reducing the trap lifetime after the MOT stage, a beam shutter (Uniblitz LS6T1ECE) was installed in the source. The shutter was mounted on the end of a Cu pinch-off tube held between the gate valve and adapter nipple (left-hand side of Fig. 3.10). Half of a stainless steel 3/8" compression fitting, affixed around the shutter aperture with high-vacuum compatible epoxy (Varian

[8]Before the addition of a cold cup to the group source design, this excess Rb load would cause an increasing leakage current across the source ion pump electrodes, requiring the pump to be replaced every year or two.

[9]I also designed a new "water block" to cool the TEC. It accepts standard NPT fittings, and its 2.75" diameter matches the CF flange for tighter fitting insulation.

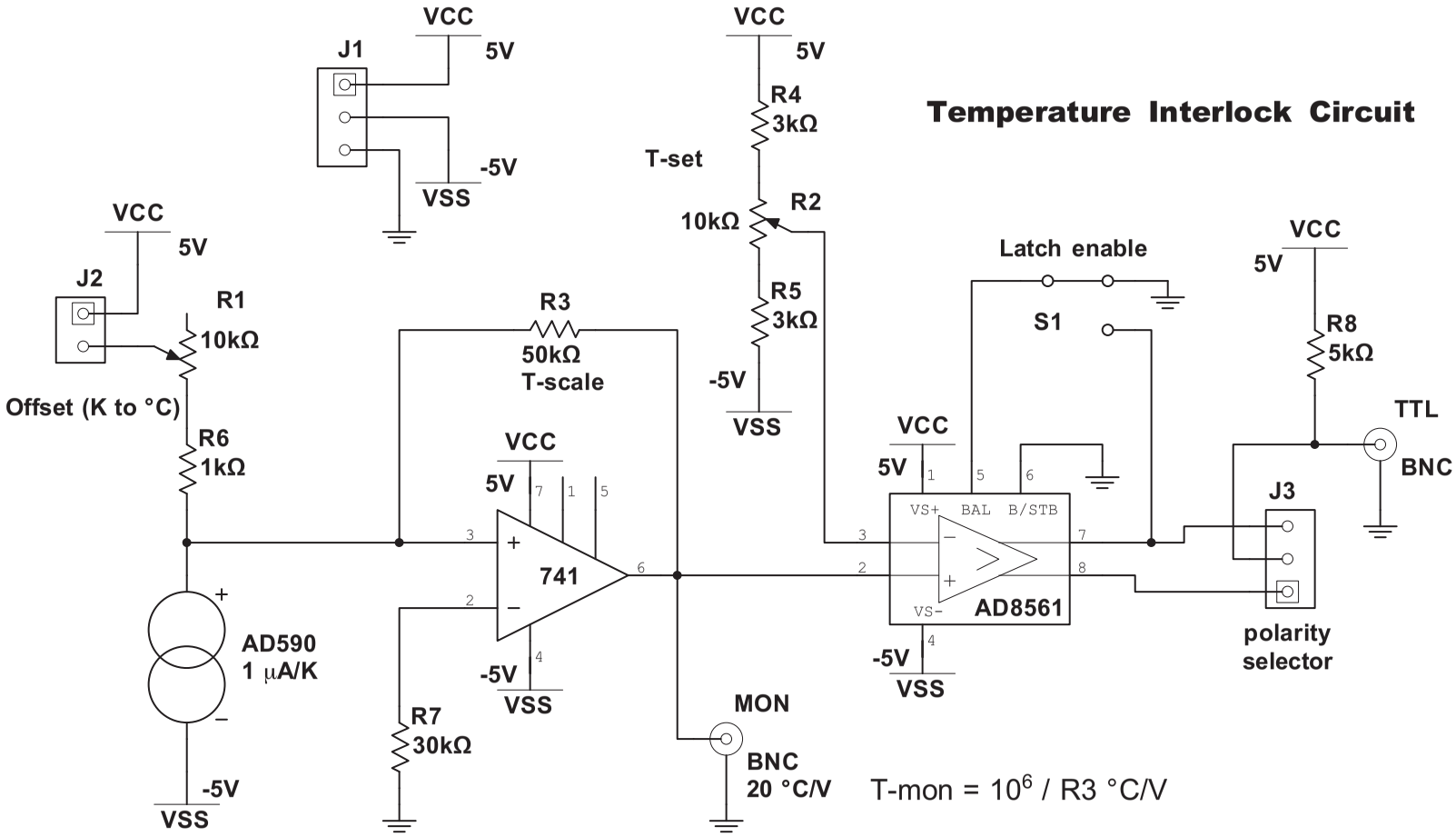

Figure 3.11: Schematic of the temperature interlock for the Rb oven cold cup. The (remote) temperature sensor is an AD590, which acts as a current source. The optional offset (J2) makes the current 1 μA/°C with the appropriate adjustment of R1. With R3 = 50 kΩ, the transimpedance amplifier (741) produces a 20 °C/V signal. Finally, this is compared to the setpoint (adjusted with R2) with an AD8561 comparator, which provides a TTL level output to control an SSR.

TorrSeal or Loctite Hysol 1C), attaches the shutter to the pinch-off. Initially, we achieved poor vacuum pressure after baking the oven, only 10^{-8} Torr. Suspecting outgassing from the shutter, we tried a few different shutters, eventually purchasing one rated for high vacuum ("ECE" specification in Uniblitz part number, rated for $< 10^{-9}$ Torr). Ultimately, it was not the shutter which limited the base pressure. The electrical connections were made with a small amount of rosin-core solder, and the outgassing of the solder flux was the problem. While UHV compatible solder is available, no solder flux should be used; instead, we switched to a crimped female contact (AccuGlass 110908) and spot-welded the leads in place. Even a standard shutter, perhaps with their actuator coil potted in TorrSeal as done for other Rb sources in the group, would have been fine. The shutter is operated with a TTL-switched driver (Uniblitz 122-BP). We modified the driver board to provide the minimum required hold voltage, V_{hold}, reducing the resistive heat load. An adjustable voltage regulator (Texas Instruments LM2575) provides

$$V_{\text{hold}} = 1.23\ \text{V}\left(\frac{R_{15}}{R_{14}} + 1\right) - 1.6\ \text{V}\,, \tag{3.2}$$

where the resistor labels refer to the 122-BP Uniblitz schematic. For the LS6T1ECE model, we used R_{14} and R_{15} = of 3 kΩ and 7 kΩ, respectively, with 1% tolerance for a measured V_{hold} of 2.54 V. We observed the shutter coil temperature by monitoring the actuator coil resistance compared to its room temperature value of 12 Ω. The temperature rise is acceptable, and the shutter can be held open indefinitely without damage.

3.2.1 Rb Zeeman Slower

The Rb atoms exiting the oven are collimated, but at 110 °C, their velocities have a Boltzmann distribution peaked at 585 m/s. A MOT's ability to catch and

trap an atom depends on the size of the MOT beams, its detuning, and field gradient. This is characterized by a "capture velocity," above which atoms will pass through the MOT; for our Rb MOT this is roughly 20 to 30 m/s, and the atomic beam must be slowed down. A Zeeman slower consists of a near-resonant laser beam opposing the atomic beam and a tapered magnet coil. The slower beam can only be resonant for a particular range of velocities, and after these atoms scatter roughly one thousand photons the Doppler shift cuts the scattering rate in half. Applying a varying magnetic field over the length of the slower can cancel the Doppler shift with a Zeeman shift of the cycling transition and maintain near-resonant scattering over the entire length of the slower [84]. An efficient slower will have a constant scattering rate, and thus constant force, for the resonant velocity class throughout the length of the slower. This leads to a square-root shaped velocity profile along the slower. Equating the Zeeman and Doppler shifts,

$$B(x) = \frac{\hbar k}{\mu_B}\sqrt{v_0^2 - 2ax} \tag{3.3}$$

where k is the slower laser wavevector, μ_B is the Bohr magneton, and v_0 is the highest slowed velocity. The acceleration $a = (\hbar k/m)\Gamma$ for atomic mass m and scattering rate

$$\Gamma = \frac{s_0\gamma/2}{1 + s_0 + (2\delta/\gamma)^2} \tag{3.4}$$

with natural linewidth γ, normalized intensity $s_0 = I/I_s$, and detuning from atomic resonance δ. The saturation intensity [33],

$$I_s = \frac{\hbar\gamma\omega^3}{12\pi c^2} \tag{3.5}$$

depends on the atomic transition linewidth and frequency ω, where c is the speed of light. The maximum scattering rate, for zero detuning and intensity $s_0 \gg 1$, satu-

rates at $\gamma/2$, corresponding to a maximum achievable acceleration $a_{\max} = \hbar k\gamma/2m$.

I designed the Zeeman slower with a program originally written by Ian Spielman. Rather than build the square-root slower profile from a layered set of packed windings as in [84], one can wind a slower from a single wire whose coils have a spatially varying pitch. The code finds the optimum spacings for a fixed number of turns. I modified it to allow for multiple, independent layers of windings and used it to produce two separate slower coil designs, one each for Rb and Yb.[10] While the target profile is given by Eq. (3.3), ultimately it is most important that the acceleration required to follow the magnetic field profile

$$a(x) = \frac{dv(x)}{dt} = \frac{\partial x}{\partial t}\frac{dv(x)}{dx} = v(x)v'(x) = \left(\frac{\mu_B}{\hbar k}\right)^2 B(x)B'(x) \tag{3.6}$$

not exceed $a_{\max}$. Therefore, kinks in the field profile that are too steep must be avoided, or the atoms will not scatter photons fast enough and will be out-paced by the Zeeman shift causing them to decouple from the slower. Fig. 3.12 shows the designed slower field as well as the measured field for the constructed slower.

Winding the slower coil was more straightforward than the bias and quadrupole coils. Computed tick marks were plotted on paper and taped to the top and bottom of the stainless steel form with wide Kapton tape. Annealed copper "refrigerator" tubing, 1/8" OD, was shrink-wrapped with insulation and wound around the form to match the tick marks. Temporarily securing the coils with zip ties every five turns allowed us to wind the entire profile and make fine adjustments to the coil spacing before permanently securing the turns with epoxy. A duplicate layer was wound with the opposite helicity for each section, roughly doubling the magnetic field when connected in series. As with the chamber coils, water is run in parallel through each layer for more efficient heat removal. With no more than 30 A per section, the second layer proved unnecessary; the slower coils rise only a couple

[10] As described in Section 3.3, we build a 2D-MOT instead of a Zeeman slower for the Yb source.

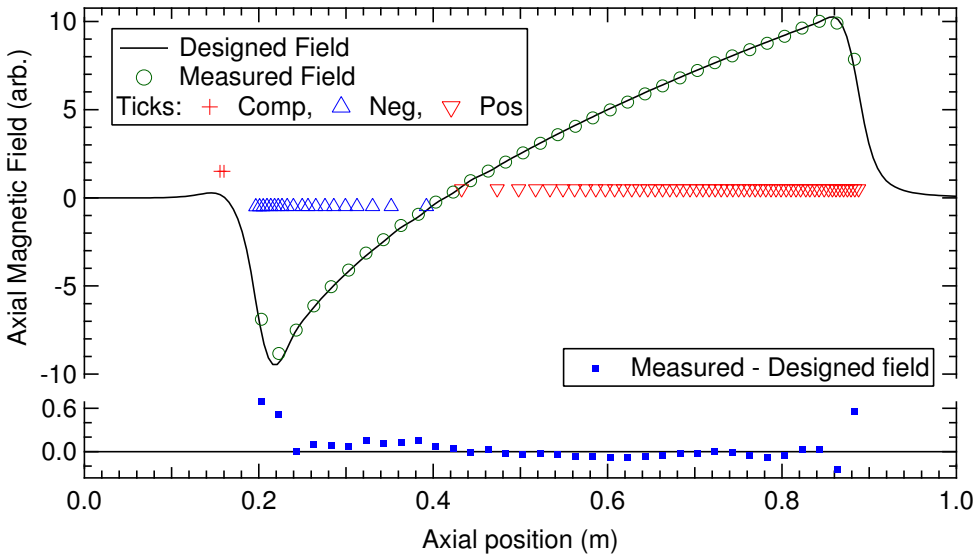

Figure 3.12: Designed field profile and coil spacing (one coil between each pair of "ticks") for Rb Zeeman slower. The measured profile of the constructed slower is also shown. The zero-crossing reduces the total power dissipated in the slower coil and puts the slower beam many linewidths off resonance at the position of the MOT. The compensation, negative, and positive sections consist of 4, 2×19, and 2×55 turns, respectively.

degrees with the currents constantly on. Additionally, a 4-turn "compensation" coil was wound around the 2.75" CF flange connecting the slower to the main chamber. In series with the end section of the slower but with opposite helicity, this coil effectively nulls the slower field at the center of the main chamber. It also causes atoms to decouple more cleanly by making a steeper turn-off of the magnetic field.

The slower-coil form slides over a long welded vacuum tube (visible in Fig. 3.10), which was wrapped in heater tape and loose layers of aluminum foil for baking. The tube tapers to a larger OD in the middle so that a diverging atomic beam is not clipped. A step-diameter profile has much smaller surface area than a single large-diameter tube, reducing outgassing. Thermocouples were installed in the middle of each section for monitoring the temperature while baking, and the coil form is held concentric to the tube with aluminum spacers at either end.

The Zeeman slower provides a significant increase in the Rb beam phase space

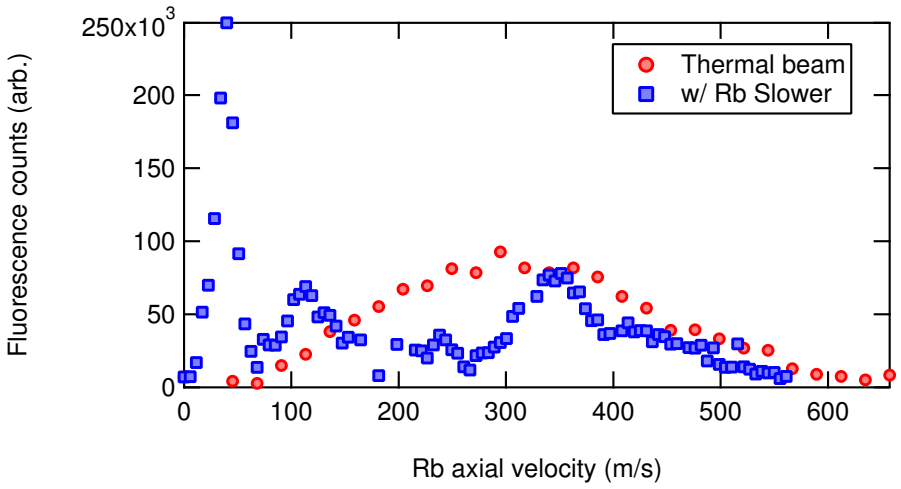

Figure 3.13: Fluorescence spectroscopy of the Rb atomic beam velocity distribution with and without operating the Zeeman slower. Due to the designed magnetic field amplitude, only atoms up to about 300 m/s are slowed, and the peak near 100 m/s is likely due to some atoms decoupling before reaching the end of the slower.

density. The fastest atoms which are slowed begin scattering photons in the maximum magnetic field at the beginning of the slower and continue to scatter photons along the entire length. Atoms with a smaller initial velocity become resonant at a lower magnetic field and only scatter photons for the latter portion of the slower. All slowed atoms exit the slower with a similar velocity, set by the slowing laser detuning with respect to the final magnetic field. Therefore, we expect significant compression of the velocity distribution for the slowed component, as shown in Fig. 3.13.

3.3 Yb source: 2D-MOT

When loading the $^3P_1$ 3D-MOT directly, the velocity of the Yb source essentially has to be as low as possible. The characteristic laser cooling velocity $v_c = \gamma/k \approx 0.1$ m/s for the 555.8 nm transition is nearly fifty times smaller than the Rb 780 nm transition. While we can increase the capture velocity by broadening the laser linewidth, it is at best about 5 m/s. After designing an Yb slower, we were concerned the exit velocity would be too large. As the velocity width exiting a

slower is typically tens of m/s, changing the slower laser detuning so that the peak was at 5 m/s would cause many of the atoms to turn around.[11] Furthermore, the slower would have been fairly large, despite being one-third the length of the Rb slower.

A 2D-MOT source solves many of these challenges. It can be very short, and the exit velocity can be finely tuned with a "push" beam. We based the Yb 2D-MOT on an existing lithium (Li) source [85]. Rough scaling of the Li numbers to Yb showed we ought to get around 10^9 atoms/s at oven temperatures lower than comparable Zeeman slowers. Our implementation of the source is shown in Fig. 3.14. Nor-Cal constructed a custom cross for the 2D-MOT region. It is a 5-way 2.75" CF cross with two additional 1.33" CF flanges. Yb is loaded in a closed half-nipple and heated to 390 °C yielding a broad, thermal atomic beam roughly perpendicular to the symmetry axis of the 2D-MOT. Care was taken to ensure the Yb has no line-of-sight to the 2D-MOT windows because unlike Rb, the very low vapor pressure of Yb causes it to stick to any room temperature surface. Two 398.9 nm beams are retroreflected along the cross directions, and the quadrupole line-zero is provided by a pair of permanent bar magnets (each composed of six magnets, K&J Magnetics BX062). As mounted, we calculate[12] the magnets provide a gradient of 48.4 G/cm with stray fields (gradients) below 20 mG (12 mG/cm) over the 3D-MOT volume in the main chamber. A standard 5-way cross supports a roughing valve and compact ion pump combined with a non-evaporable getter or NEG (SAES NEXTorr D 100-5), which provides 100 L/s hydrogen pumping speed and easily keeps the oven pressure at 10^{-10} mbar when the Yb is hot. The 2D-MOT source is connected to the chamber through a copper differential-pumping "gasket," shown in the inset of Fig. 3.14, which replaces the sealing gasket between the custom cross and gate

[11] Takahashi, Gupta and Leanhardt have all successfully use Zeeman slowers to load Yb MOTs.

[12] The calculation, performed with the Radia package described in Section 3.1, did not include the slight magnetization of the stainless steel that we have observed.

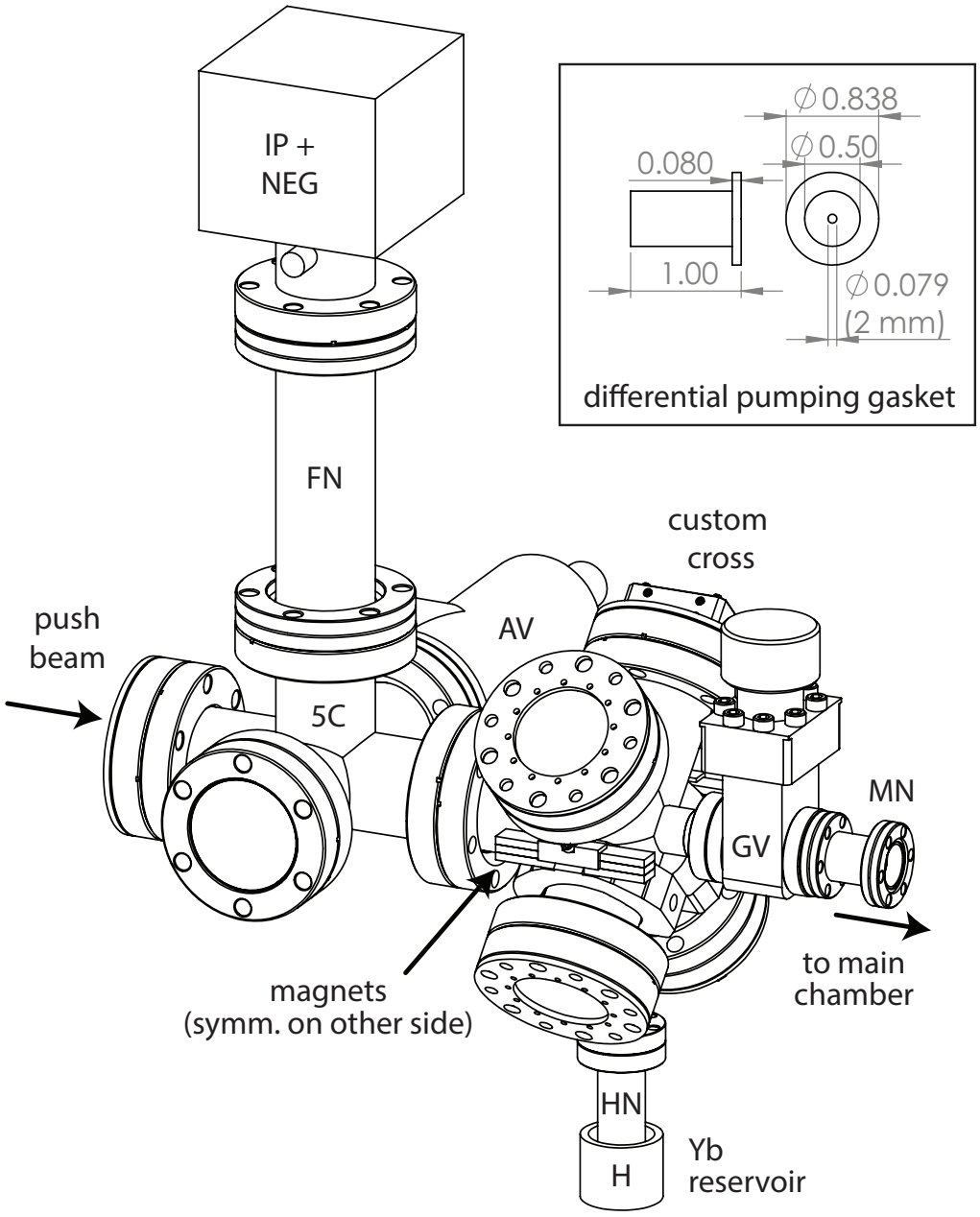

Figure 3.14: Yb 2D-MOT source vacuum chamber. All parts are standard, unless noted. The 2D-MOT beams enter through the viewports attached to the custom cross (front) and are retroreflected outside the back viewports. As on the main chamber, the viewports have custom "cage washers" (Fig. A.2) under the vacuum bolts to facilitate mounting Thorlabs' 30 mm cage directly to the vacuum system. To prevent the NEG from blocking the push beam, it was installed on a full nipple. Both the gate valve (GV) and main chamber have tapped bolt holes, requiring the use of a minimum-length nipple to connect them. *Key*—AV: angle valve, FN: full nipple, GV: gate valve, H: band heater, HN: custom capped half-nipple, MN: minimum-length nipple (custom), 5C: 5-way cross.

valve. To keep the source as bright as possible, the distance between the 2D- and 3D-MOTs must be minimized. The transverse temperature in the 2D-MOT should be roughly the Doppler temperature $T_D = \hbar\gamma/2k_B$, which corresponds to a velocity of 0.18 m/s. With an axial exit velocity of 5 m/s and a 22 cm distance to the center of the main chamber, the transverse width of the Yb atomic beam is nearly 1.6 cm at the 3D-MOT.

Alignment of the 2D-MOT is less robust than the Rb slower, and it needs to be optimized daily. The output direction critically depends on balancing the intensity of each pair of transverse beams, especially at the exit. As the atoms exit the 2D-MOT beams, an intensity imbalance provides a transverse force, kicking the atoms off line. For initial alignment, the line of fluorescence from the 2D-MOT is monitored with a small security camera, and beam alignment is adjusted to create a straight line oriented coaxially with the pushing beam. The total number in the 3D-MOT is the best measure for final 2D-MOT beam alignment. Its loading rate is also determined by the exit velocity, which must be lower than the capture velocity while still being large enough to mitigate transverse bloom. For a 2D-MOT loaded perfectly orthogonally, atoms will exit both ends with a velocity distribution given by T_D. However, the axial velocity projection of atoms due to thermal source divergence is larger than this. The addition of a spectrally broad push beam can redirect atoms exiting the wrong way back towards the 3D-MOT and increases the exit velocity. A narrow push beam will accelerate some range of axial velocities to a common exit velocity, increasing the brightness of the source. Fine control over this exit velocity is required since the capture velocity of the broadened 556 nm 3D-MOT is so low. While Sengstock's group found a 399 nm pushing beam worked best (see Section 5.4 of [86]), we empirically determined that the 556 nm transition worked better. Optimizing the pushing beam performance involves a delicate balance between increasing the 2D-MOT output at velocities which can be

captured and disturbing the 3D-MOT with radiation pressure from the push beam. What is gained by a broad-linewidth pushing beam at 399 nm in terms of atom flux is lost in our setup because we cannot prevent the pushing beam from shortening the 3D-MOT lifetime.

Optimized on 3D-MOT loading and saturated number, we find optimum performance of the 2D-MOT Yb source with the following parameters. Each 399 nm 2D-MOT beam is 70 mW with a diameter of about 15 mm and is detuned -35 MHz below resonance. The 556 nm push beam is detuned 8.9 MHz above resonance and is 2.5 mW focused to a spot inside the differential pumping tube. These parameters work well for all the bosonic isotopes, but we have observed reduced performance for both fermionic isotopes. The hyperfine splitting of ^{173}Yb limits the 2D-MOT detuning, as others have documented [86].

3.4 Current sources and water cooling

Repeatable, optimal control of atoms requires magnetic field stabilization with a large dynamic range. The quadrupole coils provide fields between 2 and 13 G/cm for the Yb and Rb MOTs, respectively, and nearly 200 G/cm for the compressed Rb magnetic trap. Our current stabilization scheme is based on feedback to the gate voltage of a MOSFET, as depicted in Fig. 3.15. A Hall-effect sensor sources a monitor-current proportional to the actual current driven through a magnet coil, and this monitor is stabilized to a request voltage with a PI control circuit (Fig. 3.16), developed within the group. Due to the non-linear current response of the MOSFETs to applied gate voltage, they require a 3 V drain-source voltage drop to source maximum current. For fast switching of the quadrupole coil, a feed-forward signal generated from the request voltage accounts for the inductive load by changing the supply voltage, ensuring the MOSFETs are active.

For the bias and quadrupole coils, the currents are supplied by Agilent 6690A

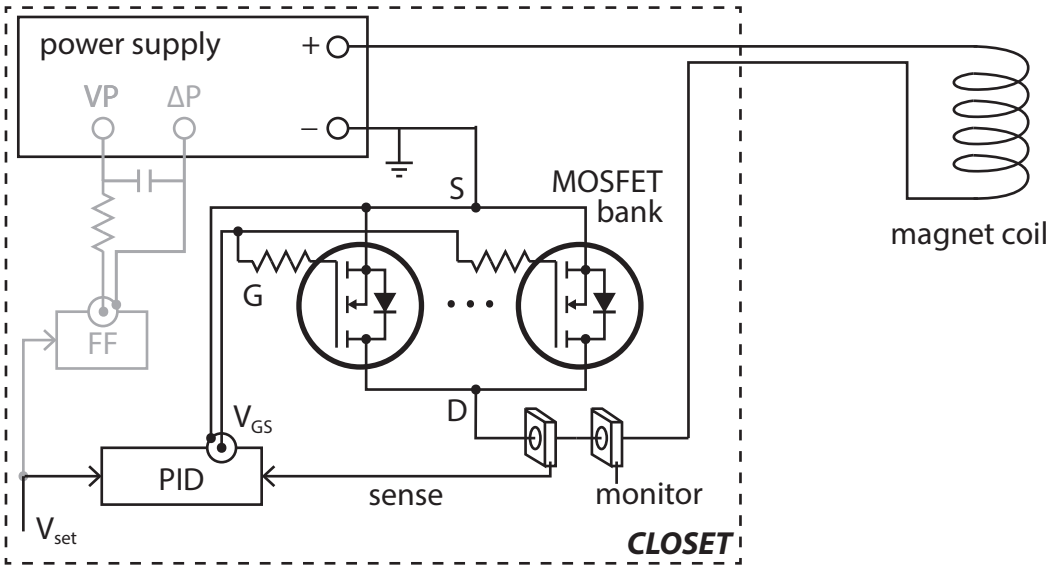

Figure 3.15: MOSFET stabilization of bias, quadrupole, and slower magnet coil currents. The "sense" signal from a Hall effect current sensor is stabilized to V_{set} with a PID circuit (Fig. 3.16) which controls the gate-source voltage V_{GS} on the bank of MOSFETs. The feed-forward (FF) is only used on the quadrupole coil and modifies the power supply voltage. As an extra precaution, three varistors (37 V transient clamping, 14 V dc max) are connected between S and D.

(15 V, 440 A) DC power supplies, while a Sorensen DHP10-660M51 (10 V, 660 A) generates the Rb slower currents. A bank of six N-type MOSFETs (STMicroelectronics STE250NS10), configured in parallel and attached to a water-cooled aluminum plate (Lytron CP10G14), control each current. To mitigate noise and laboratory heat load, the power supplies are located in a closet a few meters away from the experiment enclosure with a dedicated air return. Currents are delivered to the experiment over 4/0 AWG flexible welding cable (McMaster-Carr 7818A17) to minimize the electrical impedance of the long runs. Each cable is connectorized with a copper solder lug (McMaster 7913A4) and bolted to the MOSFETs in the closet and to a breakout panel at the experiment. This breakout panel affords easy connection of both current and water cooling through the use of compression fittings and copper tubing.

Made either from 1/8" OD "refrigerator" tubing or the square-profile tubing,

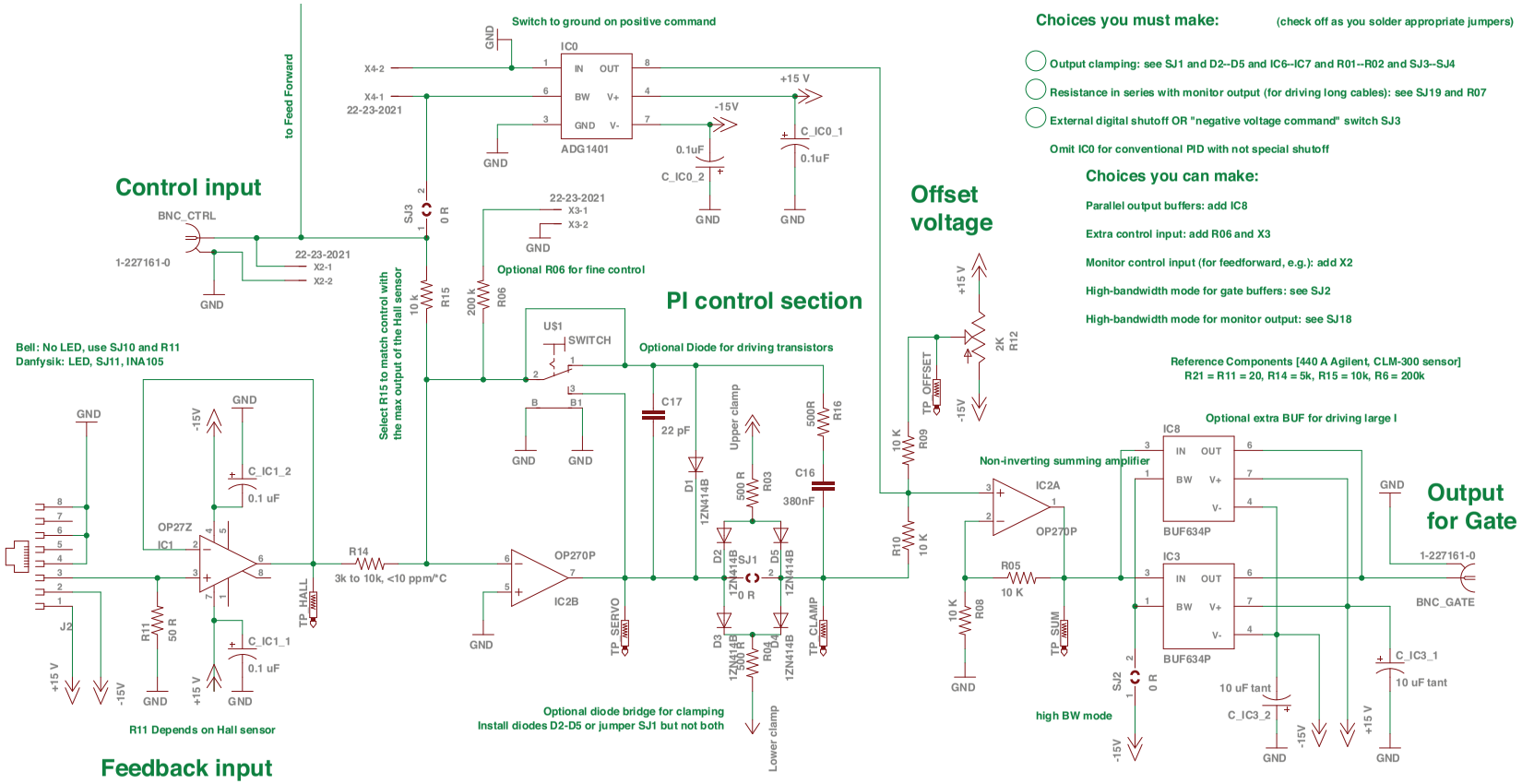

Figure 3.16: PI circuit for magnet coil current control. The corresponding monitor, power, and feed-forward circuits are in Fig. 3.17.

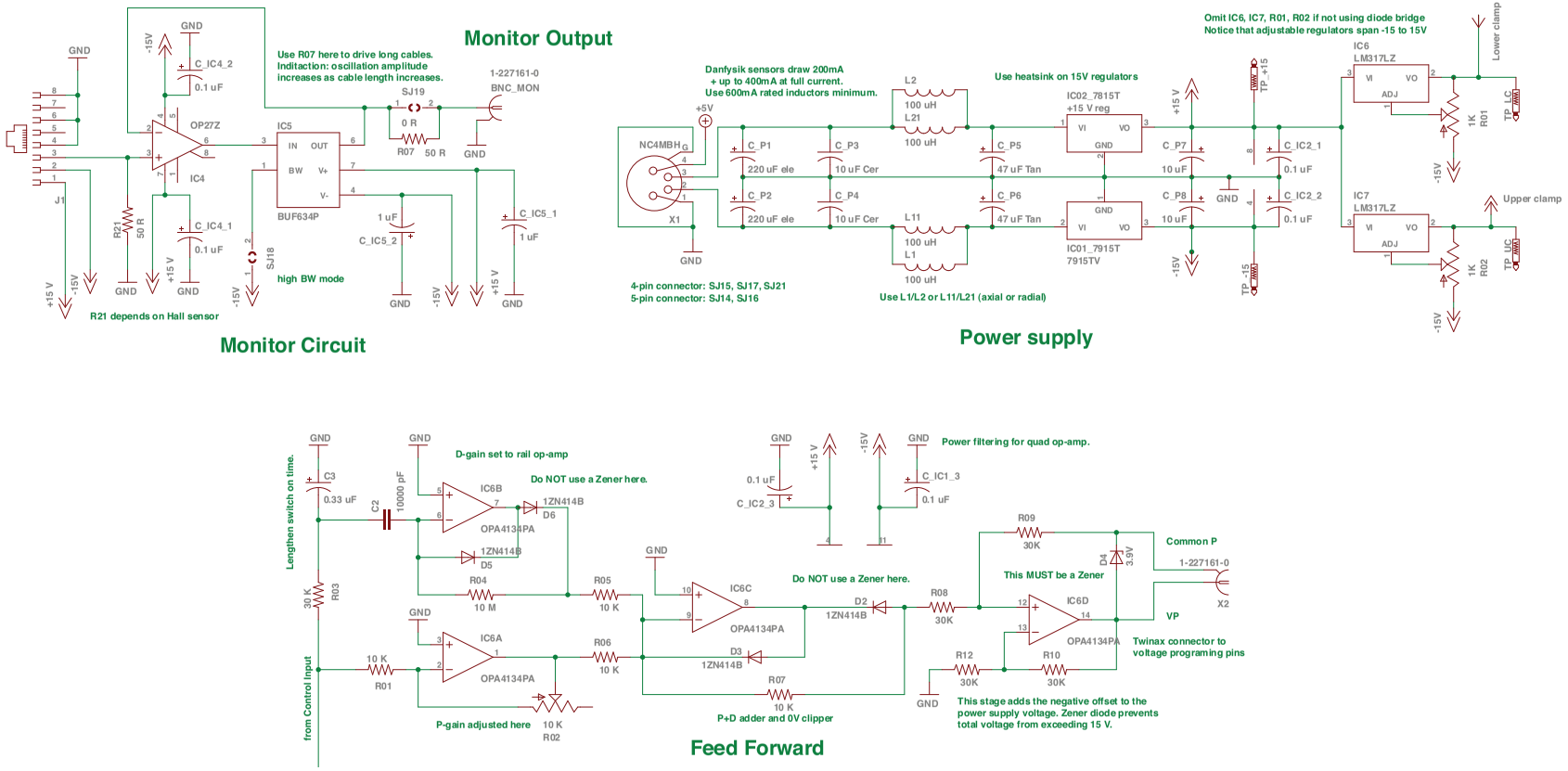

Figure 3.17: Top: monitor and power filtering portions of the current control PI circuit. Bottom: Feed-forward circuit utilized in quadrupole current control to adjust the power supply voltage.

the magnet coils have a relatively high impedance to the flow of cooling water. Therefore, we installed a high pressure chilled water loop with a 20 kW heat exchanger (Coherent LaserPure20 0301-120-00), which is cooled by the low-pressure building chilled water loop. There is a second, separate experiment (RbLi) with whom we share our laboratory space, and the heat exchanger was chosen to accommodate the heat load of both experiments. The output is split, and each experiment has a booster pump (McMaster 8449K24, Berkeley MGPS7D) with a variable shunt to provide pressure overhead between 30 and 220 psi. The noisy heat exchanger and booster pumps are also located in the closet. We have found that vibrations at the main chamber are minimized while still providing sufficient heat-sinking for the magnet coils by running with a pressure around 70 psi. However, the plumbing system was designed to handle pressures up to 250 psi. The high pressure loop is filled with a 10% solution of OptiShield Plus in distilled water to prevent corrosion of the disparate metals (copper, steel, bronze, brass) that make up the circuits. The booster pump delivers water to a plumbing manifold (Fig. 3.18) over very large diameter hose (McMaster 5630K37[13]). The manifold breaks out ten cooling lines, each with a quarter-turn valve and 440 μm particulate filter (Swagelok B-6F-440) on the supply side and a flow-switch (Proteus 100C110) on the return. The valves are opened to varying degrees to roughly impedance match coils of different lengths. Due to the small ID of the magnet coils, the filters have proved invaluable in preventing detritus, such as pieces of PTFE tape, from clogging the coils. To safeguard against overheating the magnet coils, we interlock the power supply operation to the water flow with the flow-switch, which has a user-adjusted trip-point. As implemented, all currents are disabled if any flow is too low.

Sharing the heat exchanger between two experiments has caused some issues. The initial string-wound filter on the return had too high an impedance and became

[13]Admittedly, the 1000 psi rated "mining" hose is overkill.

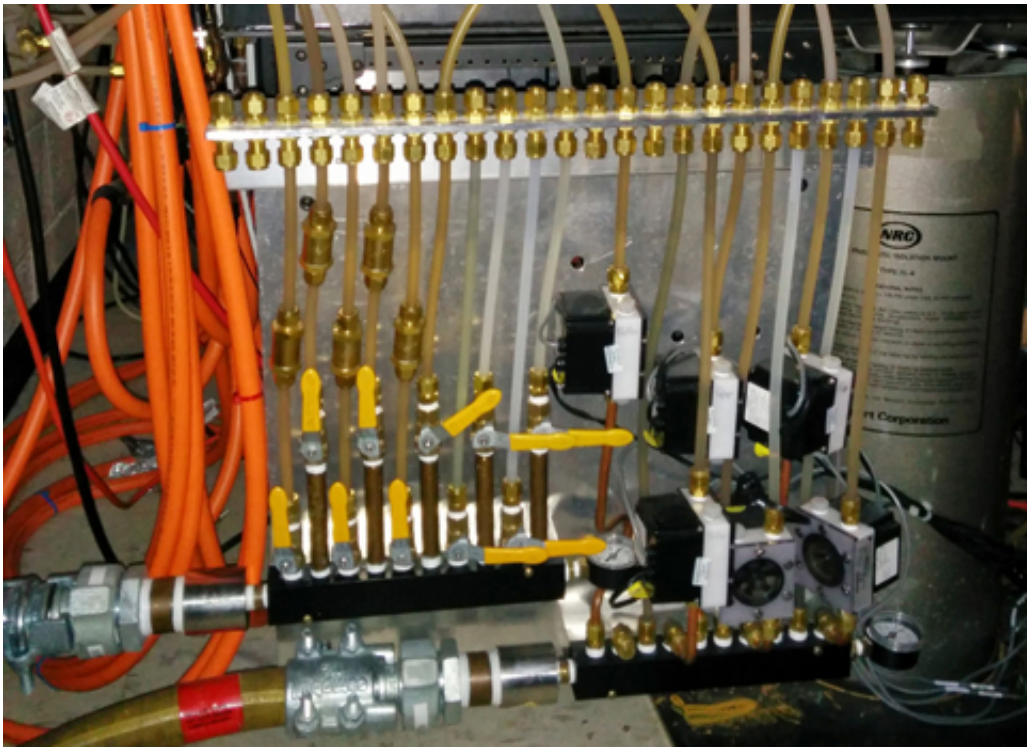

Figure 3.18: A breakout manifold provides ten magnet coil cooling lines for pressures up to 250 psi.

clogged quickly. This extra pressure drop taxed the pumping capacity of the heat exchanger and prevented both experiments from running at once. We now use a lower impedance pleated cellulose filter cartridge (McMaster 7191K11), which ought to be changed annually. It is also imperative to check the water reservoir level weekly. Each and every time it has been low, there was a plumbing leak on either the RbYb or RbLi apparatus. Usually, one of the many compression fittings which connect to the magnet coils has cracked due to over-tightening; to date, only one soldered connection has failed on the RbYb experiment. The leak has often been so slow that the only evidence was residue on the optical table where water droplets have evaporated.

3.5 Lasers

Given the complexity of laser cooling and trapping disparate atomic species, commercial systems were purchased whenever possible in the hopes that this would improve reliability. For the cooling lasers, that has meant lasers which we can easily keep locked to an atomic reference throughout an entire day. While most lasers have been reliable, I will also highlight major problems we have encountered with some systems.

The optical schematics in this section and Chapter 4 are largely constructed from Alexander Franzen's "ComponentLibrary,"[14] which is licensed under the Creative Commons Attribution-NonCommercial 3.0 Unported License.[15] Some items have been modified.

3.5.1 Rb cooling lasers

We use three separate lasers for Rb: a *master* locked to Rb absorption, to which we beatnote lock *cooling* and *repump* lasers that supply MOT, slower, and probe light. The Rb master laser (Newport Vortex II) is referenced to a Rb vapor cell through a saturated absorption lock on the ^{85}Rb $F = 3$ to $F' = 3 - 4$ crossover. The optical schematic, shown in Fig. 3.19, is quite compact. Unlocked, the Vortex exhibits strange frequency noise. Although we observe frequency swings of about 30 MHz every few seconds, the lock is able to stabilize the frequency well.

Repump light has been generated from both an inexpensive, free-running diode (Sharp GH0781JA2C, obsolete) and a Toptica DL100pro grating stabilized laser. The latter was purchased because the free-running diodes can be difficult to keep on mode. However, after experiencing numerous diode failures in the Toptica, we re-installed the Sharp laser head to minimize downtime and have not wasted much

[14] http://www.gwoptics.org/ComponentLibrary/
[15] http://creativecommons.org/licenses/by-nc/3.0/us/

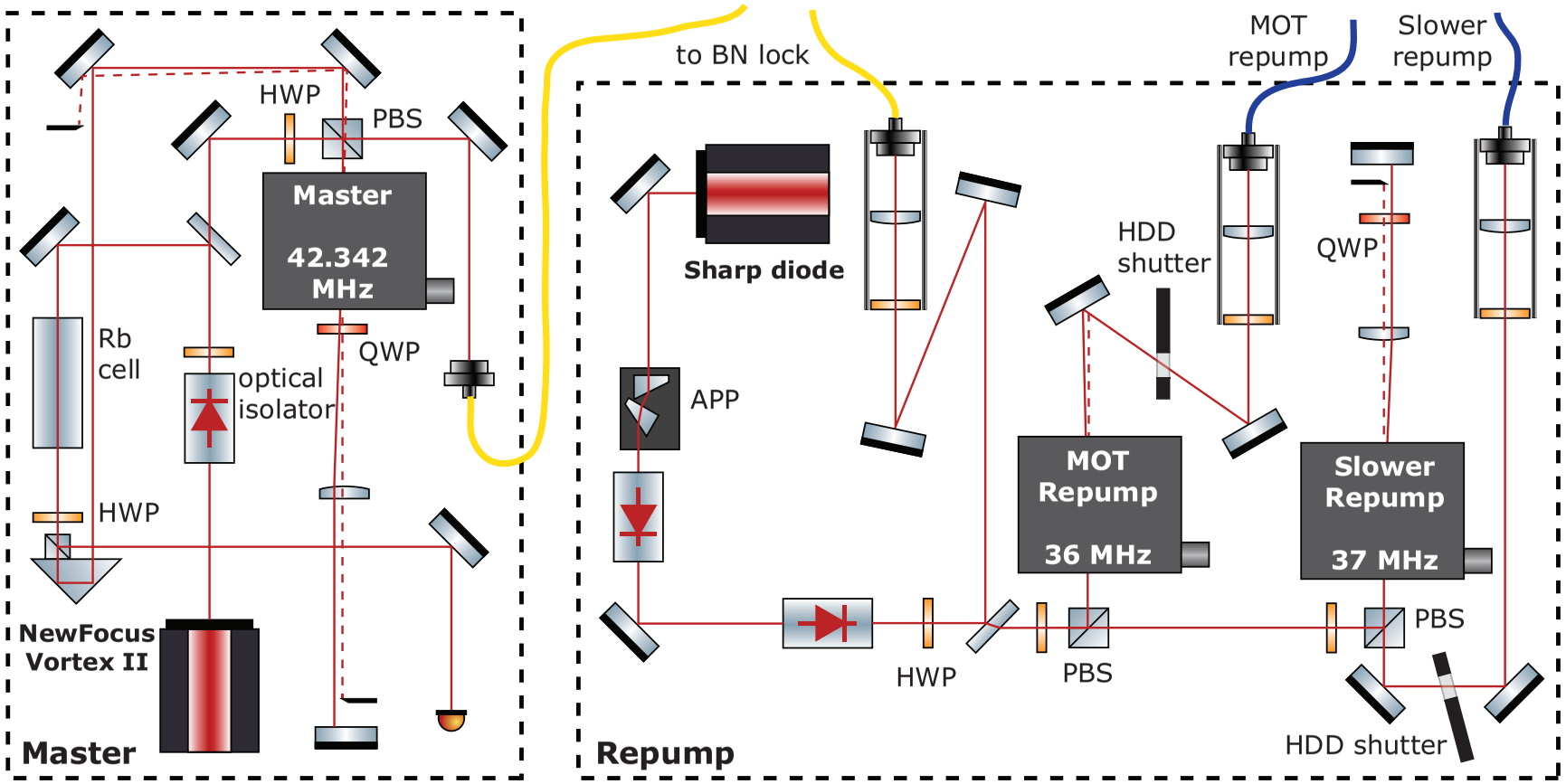

Figure 3.19: Rb Master and Repump laser schematics.

time on its idiosyncrasies. The present diode is operated around 7 °C.[16] However, each time it is turned on, the diode must be brought back near room temperature in order to find the right mode (while watching its frequency on the wavemeter) and then slowly cooled over the course of a few minutes. The schematic for division of repump light between beatnote (BN) lock, slower and MOT is also in Fig. 3.19. The power after the isolators is about 40 mW. The slower repump launch delivers 6 mW, and the MOT repump power is about 0.4 mW per beam.

The cooling laser is a tapered amplifier (TA) chip (Toptica BoosTA) seeded with 50 mW from a Toptica DLpro. Typically, we get about 450 mW from the TA. As shown in Fig. 3.20, the seed laser also provides light to three probe fibers: a pair for absorption imaging and one for the BN lock. The MOT fiber launch provides 14 mW per beam, while the slower beam is 22 mW. The seed laser diode also failed once, and after five years of operation the TA output power is reduced and will be replaced soon. While frustrating, all of these repairs are easily performed in-house.

On our laser breakout boards and throughout much of the experimental apparatus, we utilize beam shutters home-built from 2.5" laptop hard disk drives (HDD). The idea originates with Scholten [87], who maintains a webpage[17] with a recent circuit design that we have duplicated.While economical, the HDD shutters tend to bounce and occasionally fail to open. We tried changing the bumper material which limits the HDD arm movement, but sorbothane caused the shutters to stick over time. Ultimately, changing RC values on the filter in series with the HDD voice-coil (8 Ω resistance) proved the best fix, and we have settled on a 10W, 100 Ω resistor and 100 μF capacitor. These values may need to be tuned depending on HDD brand. The bounce has not been eliminated, but judicious alignment of the beam on the blocking "flag" can prevent transmission during the bounce, at the expense

[16]Despite being below the typical laboratory dew point, the TEC has survived for five years, presumably because it is oriented vertically and condensation can drip off.

[17]http://optics.ph.unimelb.edu.au/atomopt/shutter/shutter.html

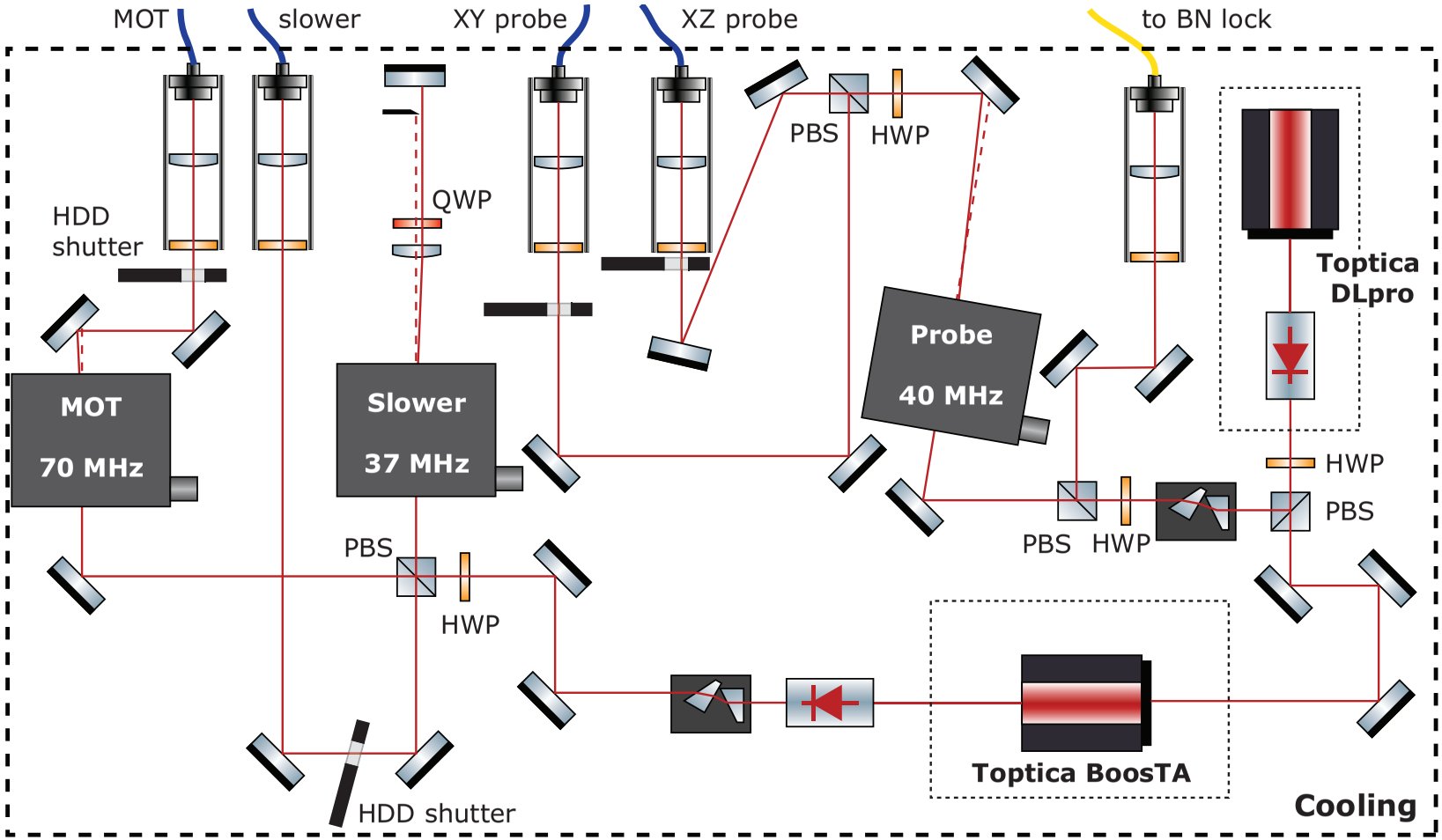

Figure 3.20: Rb Cooling light schematic.

of opening delay. The typical rise time for the shutters is sub-ms for mm-size beams and opening or closing delays are tens of ms. In most experimental procedures, we use an AOM as a fast switch with a negligible delay, and we simultaneously close the HDD shutter to block any leakage light that transmits the AOM due to imperfect turn-off of the rf drive. If near-resonant, leakage light would quickly heat the trapped atoms and cause trap loss; we also constructed boxes around each of the Rb lasers to contain the resonant light.

We accomplish flexible locking of the Rb cooling and repump lasers with a beatnote lock, which has been duplicated a few times at JQI. Both lasers are mixed with the Rb master laser on a single-mode, non-PM fiber optic "star coupler" (Fiber Optic Network Technology Co.[18]), which combines and divides four inputs equally onto four outputs. One output is coupled into a Fabry-Perot cavity whose transmission is constantly displayed on an oscilloscope, enabling us to monitor the Rb laser locks and mode quality. Another is attached to a Bristol 521 wavemeter. The third output in use is sent to the BN lock electronics, depicted in Fig. 3.21, while the fourth is not in use. The three laser frequencies (each roughly 384 THz) are converted to three beatnotes at the difference frequencies through detection with a fast metal-semiconductor-metal photodetector (Hamamatsu G4176-03) with a 30 ps rise and fall time. The largest beatnote is between the cooling and repump lasers at 6.6 GHz, roughly the ground state hyperfine splitting, and it is attenuated in the electrical schematic as the amplifiers are rated to 6 GHz. Fig. 3.22 shows each of the lock points as well as AOM shifts. The two lower beatnotes are about 1.1 GHz and 5.5 GHz and are between cooling–master and repump–master, respectively. The signals are amplified, and split with high- and low-pass filters with 3dB points around 2.5 GHz. Then each beatnote is divided down and compared to a reference by a phase-locked loop (PLL) chip (Analog Devices ADF4007, evaluation board UG-158).[19]

[18] http://www.fontcanada.com

[19] We are not using the full capabilities of the evaluation board; instead we bypass the final

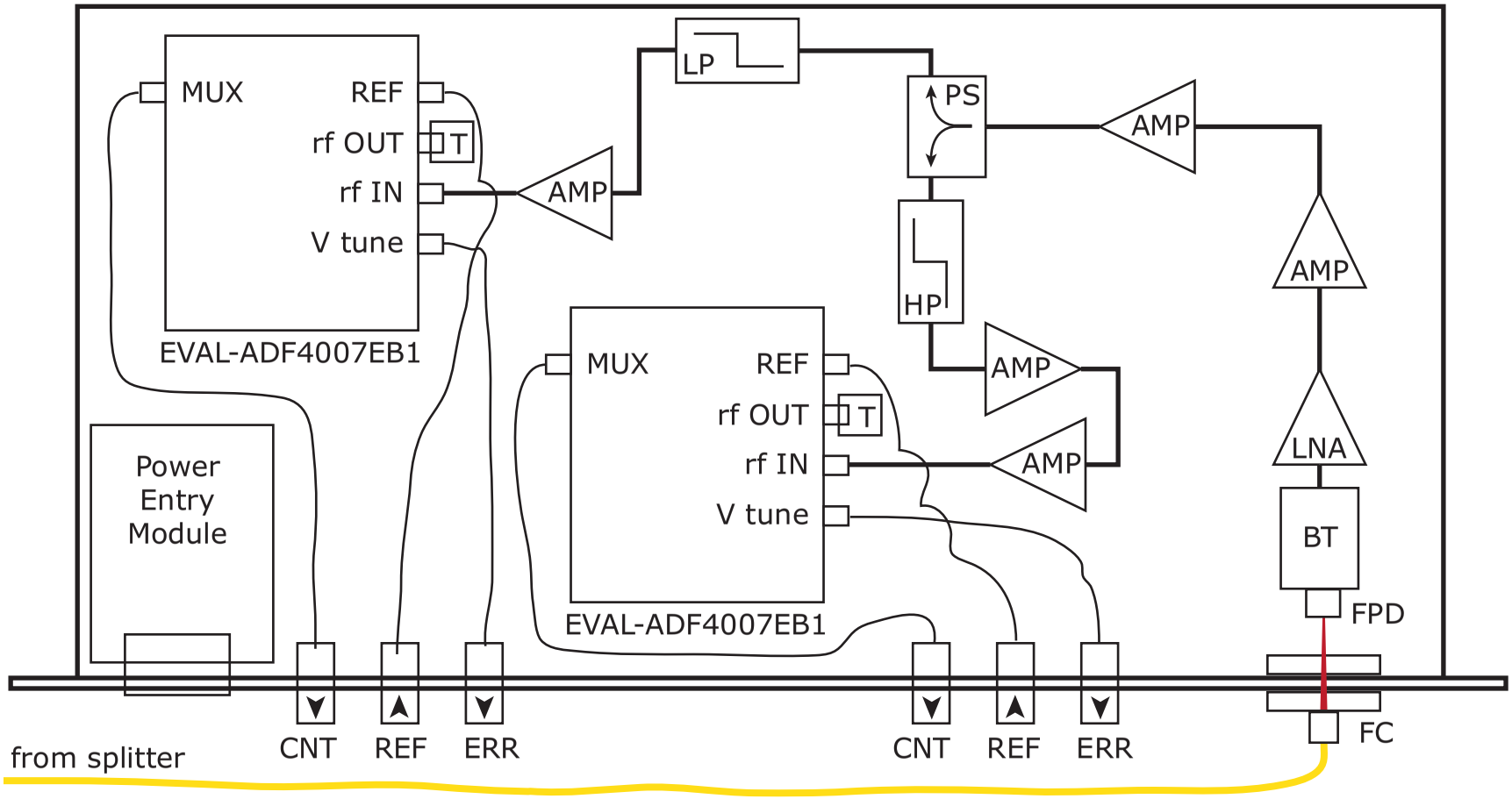

Figure 3.21: Rb beatnote lock schematic. Following schematic from bottom right— FC: FC-APC fiber port and asphere (Thorlabs A375TM-B), FPD: fast photo-detector (Hamamatsu G4176-03), BT: bias tee (Mini-Circuits ZX85-12G-S+), LNA: low-noise amp. $0.1 - 6$ GHz (B&Z Technologies BZP106UB1X3), AMP: 12-16 dB amp. (Mini-Circuits ZX60-6013E+), PS: power splitter (Mini-Circuits ZFRSC-123-S+), LP: low-pass filter < 2.4 GHz (Mini-Circuits SLP-2400+), HP: high-pass filter > 2.5 GHz (Mini-Circuits VHF-2700+), T: 50Ω terminator.

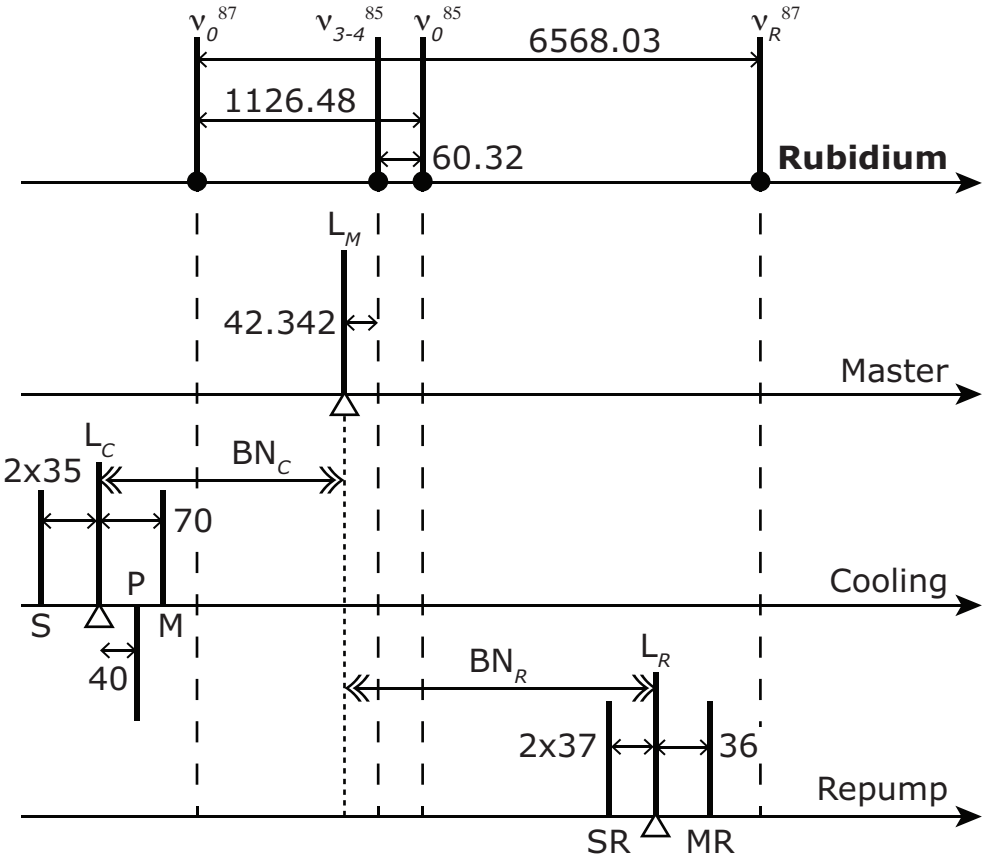

Figure 3.22: Rb laser locking scheme, (with energy *increasing* to the right). All numbers shown are frequency difference in MHz. Except for the top row, frequency differences are AOM shifts, with "2×" signifying a double-pass. Rubidium lines are at the top, where ν_0 denotes a cycling transition, ν_R^{87} is $F = 1$ to $F' = 2$, and ν_{3-4}^{85} is the strongest saturated absorption line, the crossover $F = 3$ to $F' = 3 - 4$. Lock points for each laser are at the open triangles. Frequency differences between lock points (double headed arrows) are the locked beatnotes. S: slower, P: probe, M: MOT, SR: slower repump, MR: MOT repump.

We provide external frequency references from a dynamically adjustable commercial DDS (Novatech 409B). The PLL chip optionally outputs the divided input on the MUX pin, with appropriate jumper settings, which we monitor on rf frequency counters (MFJ Enterprises MFJ-888). The cooling (repump) counter displays the beatnote frequency divided by 16 (64). When locked, the counter frequencies are stable to 100 Hz. The PLL "V tune" output has an extremely sharp transition between ± 1.3 V rails.

We characterized the switching performance of the beatnote lock when the DDS frequency is changed by monitoring the transmission through a Rb vapor cell with the cooling laser locked on the side of the ^{87}Rb $F = 2$ Doppler peak. This gave us a roughly linear frequency to intensity transfer, enabling us to observe the frequency response to a step change in the request. The frequency tends to overshoot the request by about 15 MHz per 100 MHz jump. The initial frequency change is fast, about 1.4 ms rise per 100 MHz, with a longer decay to the requested frequency of about 10 ms per 100 MHz. All these values depend on the exact PID settings and have been observed to change on the cooling laser based on the fraction of piezo voltage "fed forward" to the current controller. When the MOT lasers are moved far off resonance for the molasses,[20] we jump 136 MHz in 2 ms and the slow decay is unimportant. To move the probe light on resonance, we need to change the cooling lock point by 178 MHz. Due to the overshoot, we're within two linewidths after 16 ms, but the lock takes about 30 ms to settle on resonance within 1 MHz.

The MOT and MOT repump light are combined on another fiber splitter/combiner (2 inputs to 8 outputs, Canadian Instrumentation & Research Ltd., now Evanescent Optics, Inc.). The two inputs are combined approximately equally on six of the outputs to give a single fiber for each MOT beam which contains both frequencies. Additionally, each input has a 1% tap output which we use to monitor the

filtering op amp (OP27) and directly connect R17 to the "V tune" output.

[20] The Rb cooling procedure is described fully in Section 4.5.1.

Label	input A	input B	6-beam MOT	retro MOT
X1	15.3 %	16.4 %	H1	H1
X2	17.1	17.9	H2	–
Y1	17.0	18.1	H2	H2
Y2	16.7	15.7	H1	V↓
Z1	16.8	15.3	V	–
Z2	16.2	15.2	V	V↑
tap W1	0.9	–		
tap W2	–	1.4		

Table 3.2: Measured splittings for the Rb MOT 2-to-8 fiber splitter/combiner. The taps contain only light from their respective inputs A (repumper) and B (cooling), while the other six outputs are mixed. We re-paired output fibers for the best power balance from opposing beams in a 6-beam MOT (H: horizontal, V: vertical). Only four of the outputs are used in the retroreflected MOT; the vertical direction is still two separate beams.

fiber coupled power. Having measured the relative output on each of the six ports (Table 3.2), we found we achieved a better power balance between opposing beams in a six beam MOT with different pairings than labeled. However, once we setup the RbYb mixture, it was more convenient to use a retroreflected MOT for each species, as described further in Section 4.3.

3.5.2 Yb cooling lasers

Before purchasing the Toptica TA-SHG system at 398.9 nm, we first investigated constructing our own extended-cavity diode lasers (ECDLs). With the development of violet gallium nitride diodes for HD DVD/Blu-ray, 405 nm laser diodes have been readily available since about 2007. Unfortunately, the temperature tuning of these diodes is less than their near-infrared counterparts, necessitating purchasing wavelength-selected diodes (Nichia NDV4313) as close to 399 nm as possible. We first tried a Littman-Metcalf (Fig. 3.23) geometry, using optomechanics designed and machined at JILA. In this configuration, the first-order diffraction off a grating is retro-reflected back to the grating and fed back to the laser diode. Unfortunately, these diodes tend to be less receptive to feedback. From private communications as

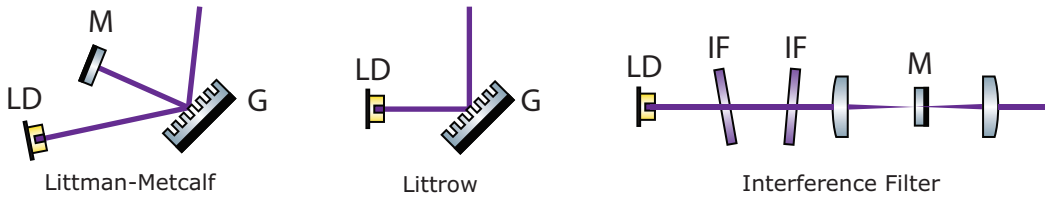

Figure 3.23: Extended cavity diode laser designs we tried for 398.9 nm. *Key*—G: grating, IF: interference filter, LD: laser diode, M: mirror.

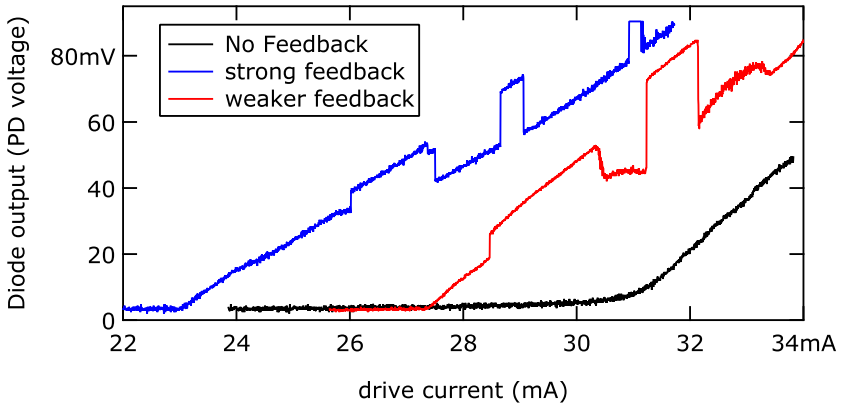

Figure 3.24: Lasing threshold depression with grating feedback in Littrow configuration. The power jumps are indicative of "mode-hops." All three ECDL configurations we tried exhibited this step-like behavior near threshold. With the Littman-Metcalf and IF cavities, the edges of the steps were much fuzzier than seen here in the more stable Littrow configuration.

well as the stable powers specified by commercial ECDL manufacturers like Toptica, the consensus seems to be that blue and violet diodes can only be stabilized up to 10-20% of their maximum output power. We have not even managed to see stable modes more than a few mA above threshold, as the frequent intensity jumps show in Fig. 3.24. We worked with a summer student to test an interference filter (IF) based external cavity laser [88, 89] for an NIR diode. Violet diodes in the IF design performed similarly to the Littman-Metcalf, presumably because the cavity lengths were similar. As the cavity length L gets shorter, the free-spectral range FSR $= c/(2L)$, or the frequency difference between constructive modes, increases which may help the desired mode compete with near-by modes of the internal diode

cavity. In an effort to minimize the external cavity length, we also tried a Littrow grating configuration, which did increase the range of current above threshold where we could see feedback. We never got rid of the mode-hops completely, and they prevented stable operation over hours.

It seemed pragmatic to purchase a commercial solution. The Toptica TA-SHG system consists of a cavity, containing a non-linear crystal suitable for second-harmonic generation (SHG), which is pumped by a fundamental laser at twice the desired wavelength, 797.8 nm. Within the last year, Toptica began offering TAs with 2 to 4 times the output power as the models we originally purchased, enabling us to get $>$ 300 mW at 398.9 nm from the system. The TA-SHG laser has not been without its problems. Maintaining efficient doubling requires optimizing the alignment of the fundamental to the cavity every few days. The TA required replacement twice within the first two years. Provided a new TA is in stock, this sort of repair has a relatively short turnaround as we can perform the work ourselves. The first repair was trickier than expected as the optimal TA seed polarization mysteriously changed to a strange orientation between chips, and we had to install a half-wave plate as well.

As violet light experiences stronger attenuation (of order 10 dB/m) within optical fiber, we "free-space" the light to the 2D-MOT and spectroscopy, although recently we have considered the potential stability benefits of fiber-coupled 2D-MOT beams. Fig. 3.25 shows the optical schematic for 398.9 nm, including two probe beams for Yb which are coupled over fiber, and the AOM shifts for the Yb lasers are diagrammed in Fig. 3.26. As the vapor pressure of Yb is orders of magnitude smaller than Rb, a room temperature vapor cell does not provide enough signal to see absorption. There are two solutions to this in our laboratory. The 398.9 nm laser is referenced to atomic absorption in a spectroscopic hollow-cathode lamp (HCL, Hamamatsu L2783-70NE-YB). The cathode of the HCL contains Yb, and

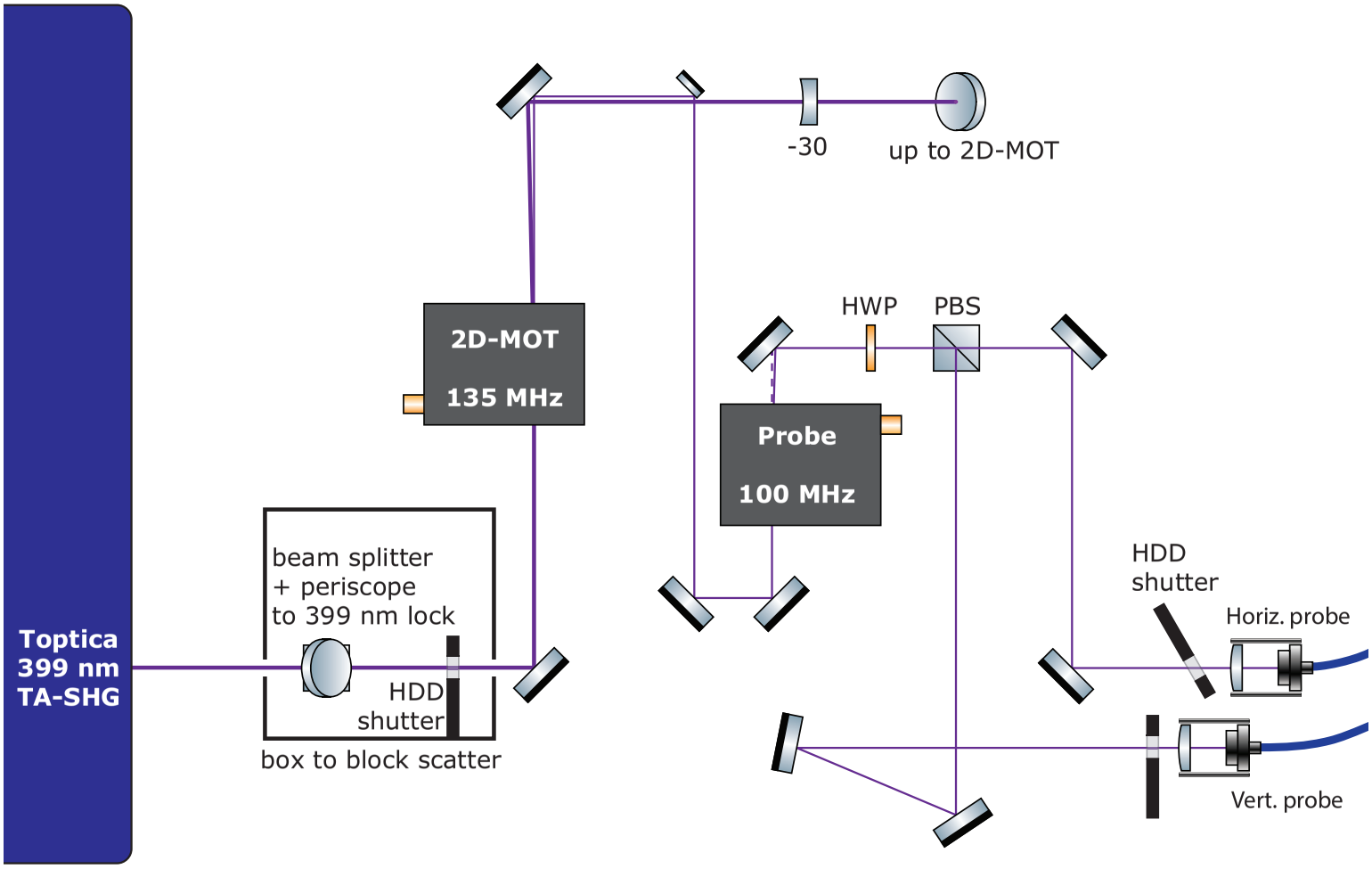

Figure 3.25: Division of the 398.9 nm light.

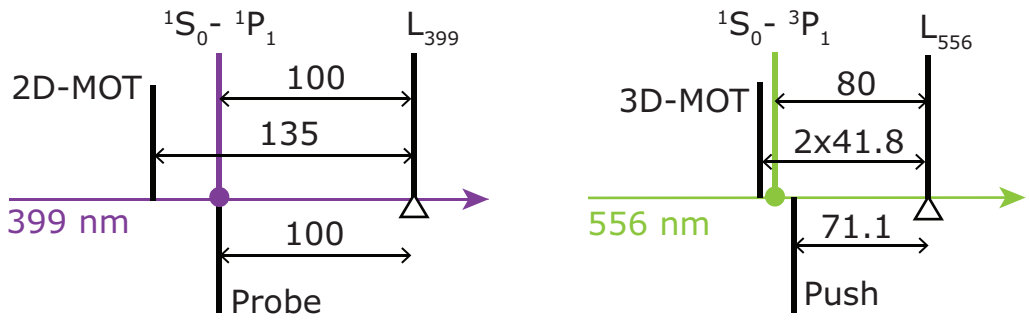

Figure 3.26: AOM shifts and lock-points for the Yb laser systems. All frequencies are given in MHz and 2× represents a double-passed AOM.

when a high voltage (Stanford Research Systems PS310) is applied, a plasma forms in the neon buffer gas which ejects neutral and ionized Yb into the vapor. Therefore, HCLs can be used to directly lock ground and excited state transitions for atoms and ions. So far, we have done saturated absorption with two 398.9 beams (Fig. 3.27) as we have not needed any repump light.

The narrow $^1S_0 \rightarrow {}^3P_1$ transition at 555.8 nm on which we operate the 3D-MOT, is locked to a home-built heat pipe (Fig. 3.28). Yb metal is placed near the center of a 1.33" CF custom nipple (N). The standard viewports (V) are angled at 5° with a custom angled-nipple adapter (A, drawing in Fig. 3.5) on each end to prevent etaloning. A 3/8" copper pinch-off tube (P) is attached to the tee (T) to allow evacuation and back-filling with helium. After back-filling to 10 mTorr and observing a satisfactory absorption signal, the pinch-off is sealed. The central region is well-insulated with fiberglass and heated to > 450 °C. For the first observation of absorption, we find it is necessary to flash-heat the Yb metal higher than 650 °C[21] after which lower temperatures give sufficient vapor pressure. Presumably, there is some sort of thin layer coating the Yb which must first be driven off. The helium buffer gas serves to shorten the mean free path below the line-of-sight distance to the windows, and we can leave them at room temperature without coating them with Yb. The buffer gas causes some pressure broadening, although not enough to

[21]This was accomplished by heating the stainless steel with a butane torch until glowing red.

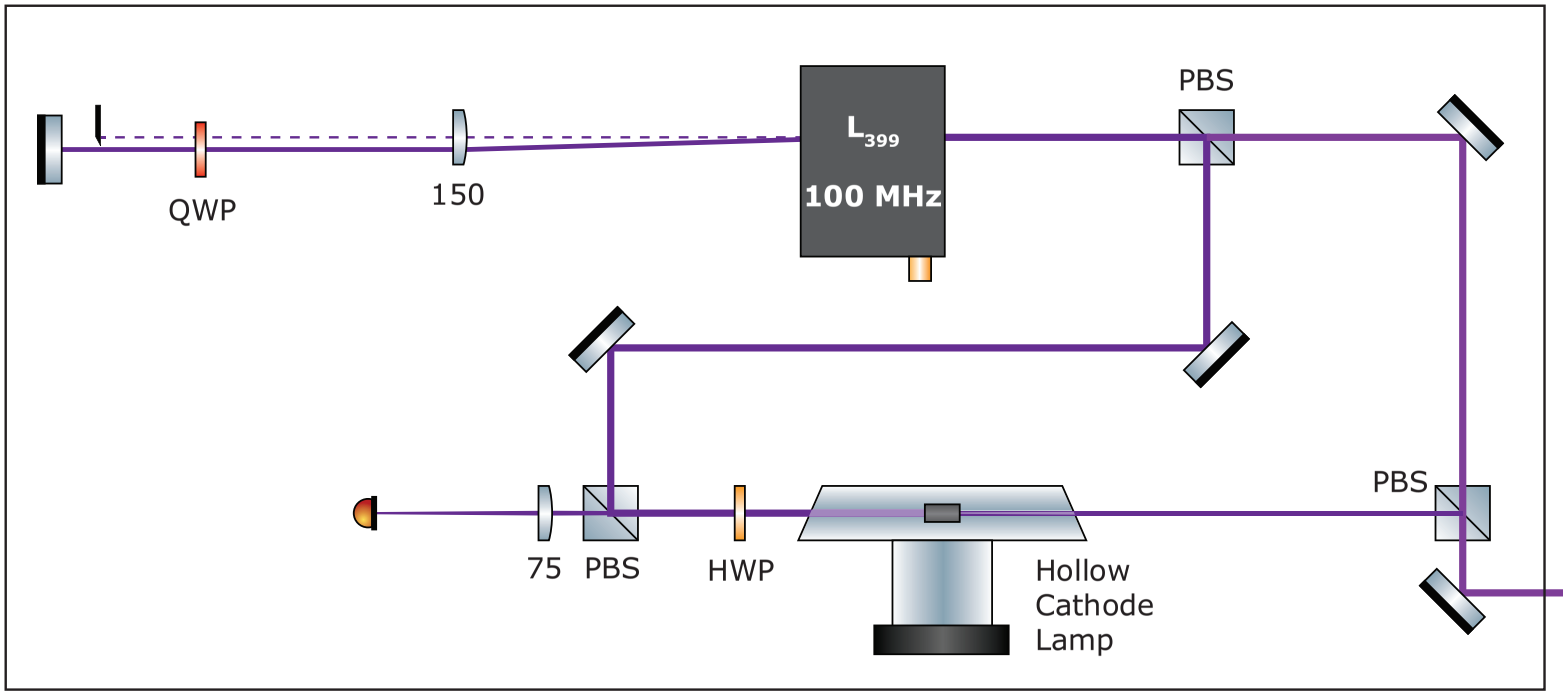

Figure 3.27: Saturated absorption lock for 398.9 nm light utilizes hollow-cathode lamp.

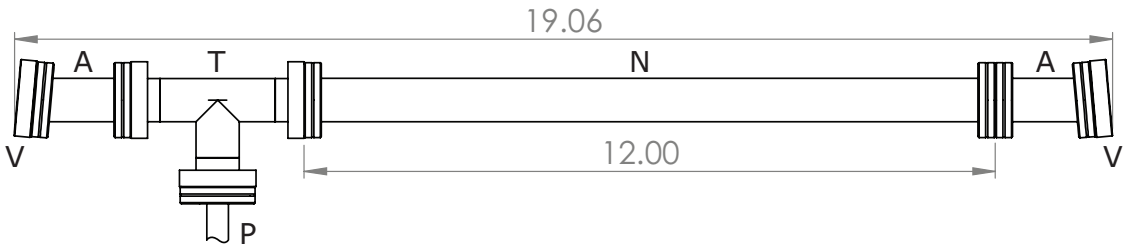

Figure 3.28: Yb heat pipe cell for 555.8 nm spectroscopy, with dimensions in inches. See the main text for a description of the labels.

explain the observed absorption linewidth of about 1 MHz.[22] With our first heat pipe, the observed absorption signal decreased slowly over time, and we had to turn up the temperature by 50 °C every few months. We constructed a second cell to swap with the first once we could no longer increase the temperature. While we used millimeter-sized pieces of Yb for the first heat pipe, the second has been loaded with a few grams of Yb foil which is easier to conform to the inner diameter of the nipple. Upon opening the first cell, we discovered that a thin, semi-transparent layer of Yb had formed at either end of the heated region. Presumably, this was attenuating the laser power. Increasing the heat may have thinned or even moved this layer, temporarily restoring a sufficient locking signal. The timescale for this migration is tolerable, and we expect to need to change the cell again in 12 to 18 months.

The 555.8 nm laser was purchased from Menlo Systems. It consists of an OrangeOne model laser operating at 1111.6 nm which pumps a periodically-poled lithium niobate (PPLN) wave-guided doubling crystal. The fundamental laser and doubling head are connected with direct fiber splices, and contain no user serviceable parts. Unlike the TA-SHG system, this means there is no need for alignment. The only knob for optimizing the SHG efficiency is the setpoint of a temperature controller which heats the PPLN, and we find this setpoint only needs to be changed for large changes in pump power or ambient temperature. As shown in Fig. 3.29,

[22]This is the width of the $m_J = 0$ peak when split with a strong magnet placed beside the heatpipe. Power-broadening from the pump intensity contributes to the linewidth as well.

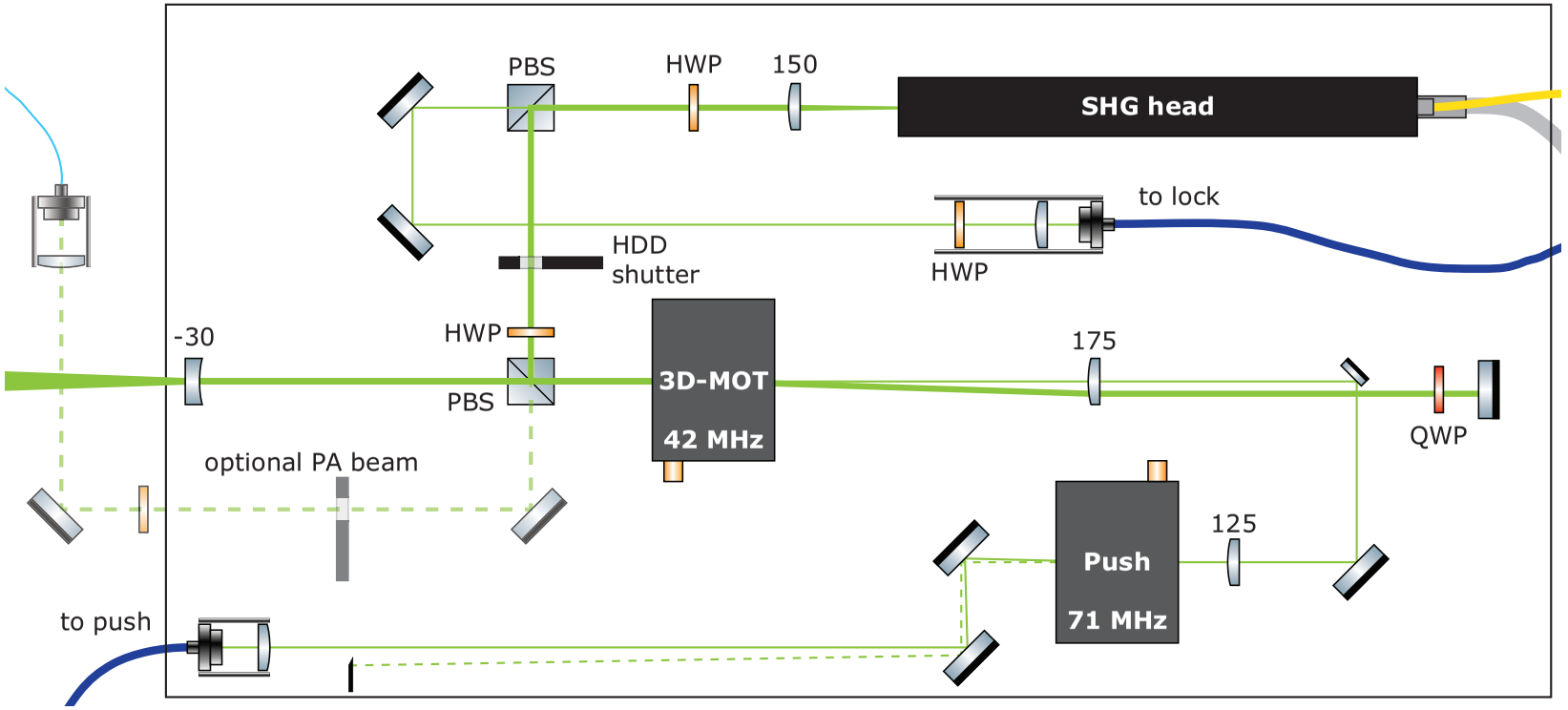

Figure 3.29: Optical schematic for distribution of 555.8 nm cooling light. Lens focal lengths are given in mm. On the left-hand side is an optional fiber launch for a photoassociation (PA) beam.

the laser out is directly split between the lock (Fig. 3.30), 2D-MOT push beam, 3D-MOT beams, and a photoassociation beam. Precise AOM shifts are given in Fig. 3.26.

For the first two years we operated the laser around 65% of its maximum output, obtaining roughly 150 mW at 556 nm from 0.7 W of pump power. Within a few months of routinely running at full power (1.2 W pump producing >250 mW SHG) the seed fiber laser within the OrangeOne portion (sourced from NKT Photonics) started mode-hopping. We were able to keep it locked for roughly one hour at a time, but eventually a mode-hop would break the lock, and sometimes this even caused the output power to drop enough that an internal safety would shut off the amplification stages. The mode-hopping degraded over the course of six months, and Menlo Systems determined the laser system would need to be shipped back to the factory in Munich; ultimately it took two months to repair and return the laser at a cost of almost 40% of the purchase price. While the seed laser death was probably a fluke, within three months of operating the repaired laser, the doubling stage failed catastrophically resulting in another three months without the ability to make an Yb MOT. Throughout the negotiations regarding the repairs, Menlo Systems has proved responsive and eager to explain the physics behind each of the failures. As a result, it has been extremely useful to log all monitor values provided by the laser controller interface *when the laser is in good working order* under our laboratory conditions, enabling at-a-distance diagnostics for the issues we have encountered.

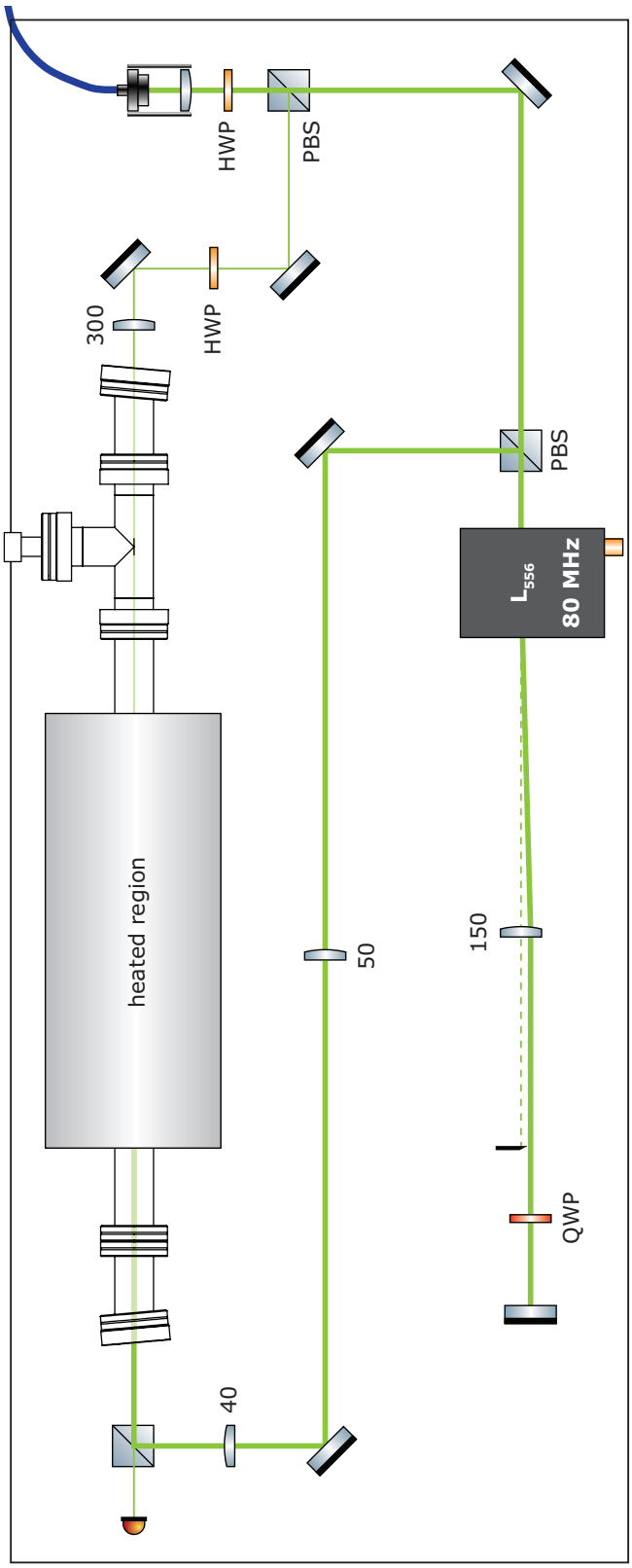

Figure 3.30: Optical schematic for the 555.6 nm lock.

	532 nm	1064 nm	$\alpha_{532}/\alpha_{1064}$
Rb	−249.3(7)	687.5(1.2)	−0.363(2)
Yb	267(12)	162(7)	1.64(14)
$\alpha_{\mathrm{Rb}}/\alpha_{\mathrm{Yb}}$	−0.93(4)	4.23(20)	

Table 3.3: Calculated polarizabilities (in a.u. of a_0^3) for Rb and Yb at the two dipole trap wavelengths. Relative polarizabilities are also shown. Details on these calculations are given in Appendix B.

3.5.3 Dipole trapping lasers

As described in Section 2.1, independent control over the dipole traps for Rb and Yb is possible through the use of two laser colors. The polarizabilities of each atom at 532 and 1064 nm are summarized in Table 3.3. Certainly other combinations could have been chosen, but multi-watt commercial lasers are readily available at 1064 and 532 nm.

The 1064 nm dipole trapping light is generated by a 30 W fiber amplifier (IPG YAR-30K-1064-LP-SF) seeded by a 30 mW fiber-pigtailed laser (QPhotonics QFBGLD-1060-30PM), with fiber-Bragg grating (FBG) stabilization for single mode operation. We found that seed operation was unstable below about 70 mA of drive current or 16 mW output power, consistent with the specified threshold current. Observing the interference spectrum with a fiber splitter and 2 km delay fiber in one arm, we confirmed that the linewidth is < 3 MHz when operating at full output power. The amplifier requires between 1 and 5 mW seed light, and the seed power (operating at 130 mA) is set with a fiber attenuator (OZ Optics BB-500-11-1064-6/125-P-50-3A3A-3-1), which provides a stable attenuation factor without requiring constant realignment. Originally, we purchased a laser which included an internal seed (IPG YLR-30-1064-LP-SF). However, within a few months of consistently operating at the full 30 W output, it sustained "optical schematic damage" and was completely rebuilt over three months. With a handful of labs all using high-power 1064 dipole traps, the larger group maintains a spare laser which fortu-

nately limited down time. The 1064 nm light is delivered to the experiment over two fibers (NKT Photonics LMA-PM-10 and LMA-PM-15), whose core contains a hexagonal lattice of air-holes that run the length of the fiber. This photonic crystal structure, rather than a step-index, provides single-transverse mode guiding over a very large wavelength range with a larger mode diameter than solid-core fiber. Fig. 3.31 shows the optical schematic for the fiber launch board. To protect the fibers from potential steering during AOM warm-up, mirrored shutters constructed from a half-inch mirror epoxied to the arm of an HDD shutter, are placed to dump the launched order when not in use. This allows both optical and rf power to be applied, keeping the AOM warm, without sending light to the fiber.

While the 1064 nm laser power can be varied continuously up to 30 W, we have found it difficult to maintain good fiber coupling efficiency over a wide range of powers. The culprit appears to be thermal lensing due to some combination of the optical isolator and our telescope optics, despite using fused silica lenses. We have also seen thermal lensing in the fiber launch lenses. To deliver maximum power to the dipole beams, we run the laser at full output power and split it equally between the two fiber launches. After aligning each launch at low total laser power, the power is increased a few watts at a time and the fiber launch carefully re-optimized. In this way, we achieve the best coupling efficiency at highest power. Even though the efficiency degrades as the diffracted power is lowered with the AOM, we are dumping less power into the fiber cladding and mount than we would have at high power, preventing damage from optical heating.

An 18 W VERDI (Coherent V18) laser at 532 nm was used for the second dipole color. This laser has also required servicing multiple times. Most recently, the doubling head had to be replaced. The division of the 532 nm laser into two dipole beams is diagrammed in Fig. 3.32. Due to the lower polarizability, we have tried to avoid fiber-coupling loss for the 532 nm dipole beams to maximize the delivered

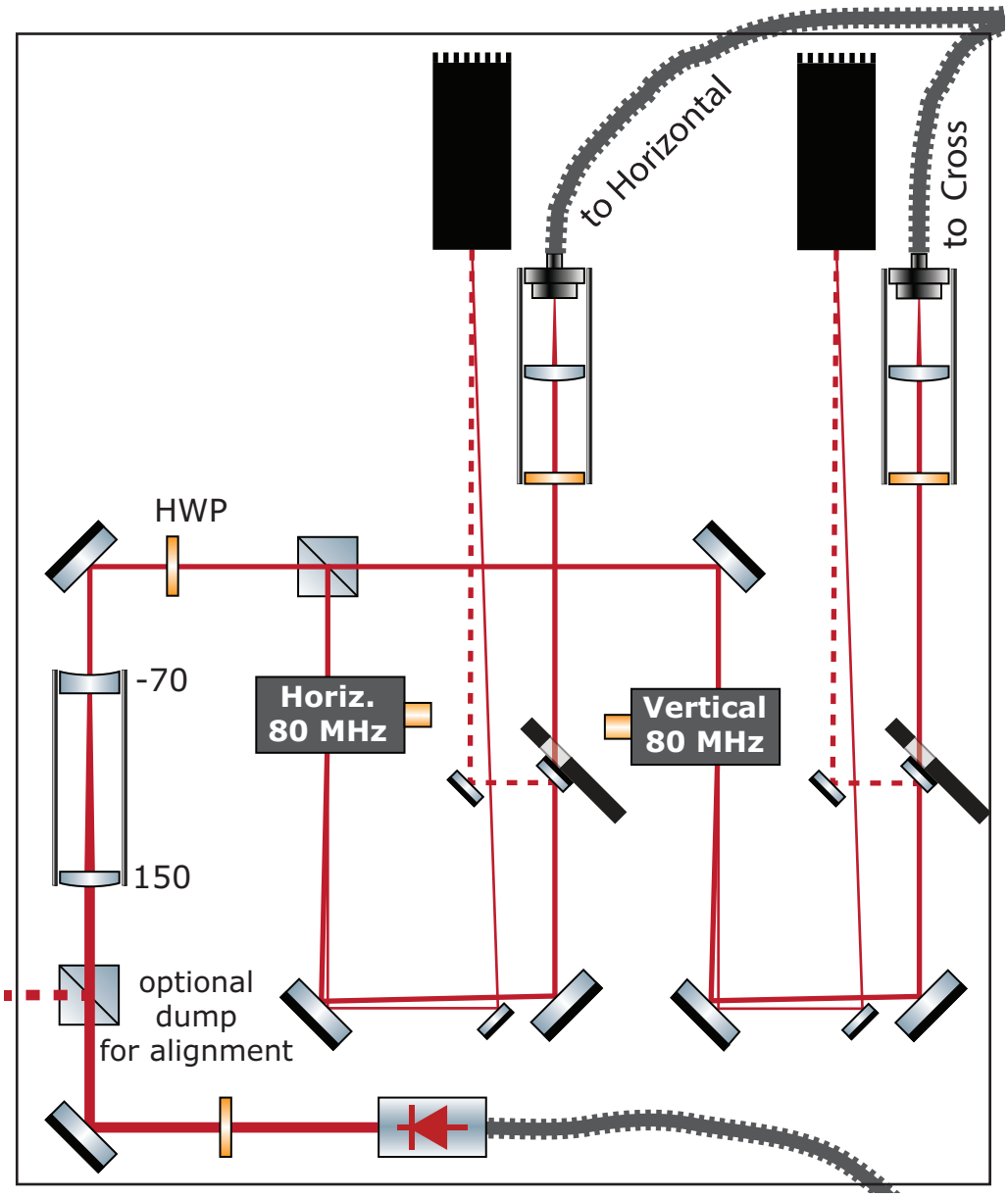

Figure 3.31: Optical schematic for 1064 nm dipole beam fiber launches. Focal lengths are in mm.

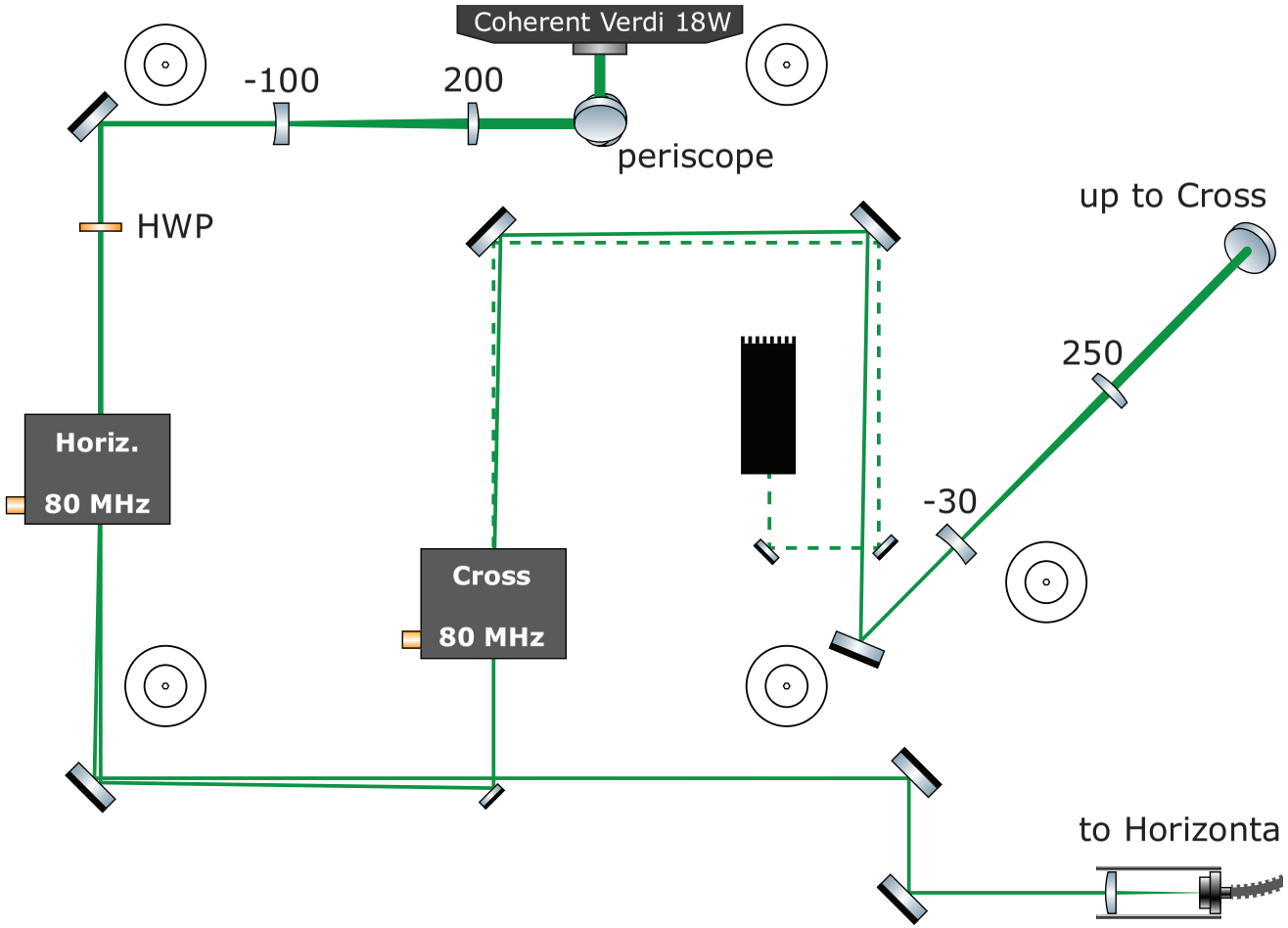

Figure 3.32: Division of the 532 nm laser into two dipole trapping beams. Lens focal length are given in mm.

intensity. However, particular beam configurations require stable alignment only a fiber can deliver. Section 4.3 contains a careful discussion of engineering traps for RbYb mixtures, including the difficulty of maintaining overlap for two-color crossed-dipole traps.

3.5.4 Yb-only lattice

For Rb-blind trapping at the light-shift zero wavelength, $\lambda_{\text{zero}} = 423.018(7)$ nm (see the inset of Fig. 2.1), we used another Toptica TA-SHG system. The TA's gain is peaked around 860 nm with a range of nearly 30 nm 6 dB below peak. The seed diode laser has a free-running wavelength of 835.4 nm and with Littrow stabilization can be tuned between 840 and 849 nm. Therefore, the SHG output can be tuned between 420 and 424.5 nm, a range wide enough to cover both λ_{zero} wavelengths near the Rb $6p$ doublet. This wide tuning range enabled us to make a precision measurement of the $\langle 5s_{1/2} \| D \| 6p_j \rangle$ reduced electric-dipole matrix elements, detailed in Chapter 5. The SHG output power is 250 mW around 423 nm and drops to 180 mW at 420 nm. We have had no problems with this laser, although it has only been used heavily for the precision measurement to this point. Internal alignment also needs to be optimized every few days as with the 398.9 nm laser. This alignment does not change the SHG output direction, which is determined by the doubling cavity mirrors, however changing the laser wavelength typically will. The crystal must be rotated horizontally within the cavity for optimal phase matching of the SHG nonlinear process, necessitating walking the cavity output mirror as well.

3.6 Computer control

Experiments with degenerate quantum gasses require precise timing, often down to fractions of a microsecond, while the duty cycle of experimental shots varies

between seconds and minutes. Briefly, I will describe our approach, standardized across the entire group of laser cooling and trapping experiments at JQI, to this challenge. A "master" digital device provides a variable timebase for each "slave" device. The slaves must be able to store a program as a table of output states and step through lines of this table when triggered by the master. Both the master and slaves are programmed by a control computer in entirety before starting a given experimental cycle. In this way, the computer is removed from experimental timing.

The standard master is 24 output commercial FPGA-based card (SpinCore PulseBlasterUSB) capable of providing TTL pulses with programmable spacing between 50 ns and one week. Programs can be up to 4000 lines long and it supports loops nested up to 16 levels deep. We use a few types of slave devices. For programmable frequencies, predominately to drive AOMs, we use a commercial DDS (Novatech 409B) with 0-171 MHz, 0.1 Hz resolution, and internal memory capable of storing an output table of 32768 points. Its table-mode output cannot be triggered faster than every 150 μs, which by current standards is quite slow. While we have never used it, the Novatech is capable of frequency sweeps through direct programming of the internal DDS chip (Analog Devices AD9959), although not in tabled mode. Other labs have built an FPGA- or Arduino-controlled DDS replacement with 0-200 MHz output and better than 0.1 Hz resolution. The DDS chip (Analog Devices AD9954) can also output linear frequency sweeps between two specified frequencies with 10 ns time steps. On-board memory limits the DDS output table to 1024 lines (512 if utilizing sweeps).[23] Programmable analog voltages are provided by National instruments cards (NI USB-6229 and NI PCI-6733), the former of which also has a plethora of digital outputs and analog inputs. The majority of our data acquisition is in the form of images, however the analog inputs have

[23]Complete documentation for "in-house" hardware is available on the group wiki, presently at https://wiki.umd.edu/JQIamo, but migrating in the near future to https://jqi-wiki.physics.umd.edu.

proved very useful for diagnosing experimental timing issues like the sticky HDD shutters discussed in Section 3.5.1 or logging laser power with a photodiode over the course of an extended experiment. There are also some devices which do not fit the master-slave model, such as a microwave source (Standford Research Systems SG384) whose output often needs to change each cycle.

Historically, the computer control software, written in National Instruments LabVIEW, was very inflexible to the addition of a new kind of slave device. Recently, we rewrote the control software entirely making the underpinnings object-oriented. Essentially, all slave devices are treated equally; adding a new device now consists of providing a prescribed set of device methods, but there is no longer any need to modify the central code which takes a procedure, divides it up into devices and commands them to program their respective hardware.

3.7 Environmental control

An overhead structure was constructed for dust mitigation before moving optical tables into the laboratory. The tables are at one end of the laboratory space, and the extruded aluminum frame (80/20) provides a front wall and ceiling for the enclosure. This ceiling is sealed from above with sheets of PVC for the first four feet and 0.08" thickness vinyl (McMaster-Carr 1894A12) for the remainder.[24] Initially, we tried securing the vinyl with adhesive hook-and-loop strips, however there was an adverse reaction which caused the adhesive to slowly drip onto the optical table below. Instead we used screws through holes punched in the vinyl, secured to the 80/20 T-slot; duct tape has also held the vinyl securely without issue. HEPA filters (Camfil Farr Slimline series 41-DCM, 23.6" square), installed in close-fitting cutouts in the ceiling, provide filtered air from a dedicated university-controlled variable air volume (VAV) environmental control (HVAC) system. Shelving constructed from

[24] Another lab used a thicker vinyl which proved too heavy to easily support across 24" spans.

80/20 and PVC sheet is suspended from the rafters over each optical table providing sturdy support[25] for countless pieces of electronics and lasers.

Unfortunately, the HVAC cooling capacity barely matches our heat load making a stable laboratory temperature difficult to maintain. We have worked through seemingly endless issues with the university HVAC technicians but have finally achieved 0.5 °C temperature stability normally. However seasonal changes and unusually cold outdoor temperatures warrant extra scrutiny of the laboratory temperature control. HEPA replacement will be relatively easy as one can access the top of the enclosure. The lifespan of a HEPA filter depends on the pre-filtering and fraction of re-circulated air, however the manufacturer recommends replacement once the pressure drop doubles across the filter; under typical conditions, this may take ten years. Given our demonstrated need for high air flow to combat the heat load within the enclosure, HEPA replacement should be kept in mind in the coming years.

[25]The stiffness of the structure was confirmed during the magnitude 5.8—nearly magnitude 3.0 in College park—earthquake in August, 2011!

Chapter 4: Engineering Mixtures of Rb and Yb

As outlined in Section 2.1, creating a lattice of Yb atoms immersed in a Rb BEC requires large, near-degenerate mixtures. To efficiently load the Rb-blind lattice, we will need a crossed-dipole trap for Yb to match the tight confinement of the optical lattice. Rb atoms can be confined in either a hybrid quadrupole plus single dipole trap or a crossed-dipole trap. In addition to the single-species cooling and trapping (described in Sections 4.5.1 and 4.5.2), sympathetic cooling can be leveraged for ultracold mixture preparation 4.5.3.

4.1 Rb and Yb MOTs

While the fastest route to an ultracold mixture of Rb and Yb might have begun with overlapping MOTs, the Görlitz group has observed strong interspecies losses for a dual RbYb MOT [29]. In his thesis [90], Nemitz describes their observations fully. The presumed mechanism involves light-assisted RbYb* collisions, where the ytterbium is in the $^3P_1$ excited state, which impart enough kinetic energy to both atoms for them to escape the MOT. They conclude that Rb*Yb losses are negligible upon seeing no change in the loss rate between bright and dark-spot Rb MOTs. In the latter, the repumper is masked in the center of the MOT causing atoms to accumulate in $F = 1$ making the MOT light far off resonant. With the addition of a depumper, Nemitz reports more than 90% of the Rb atoms were in their ground state.

Unless one cools the minority species sympathetically, large MOTs of each

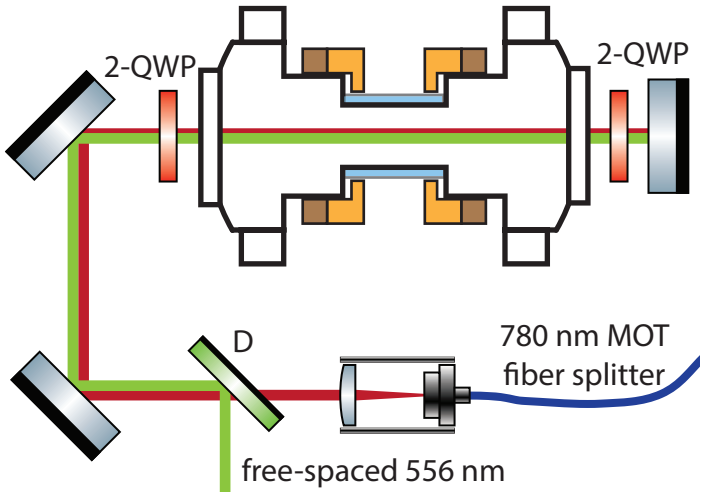

Figure 4.1: After combination on a dichroic mirror (D), the Rb and Yb MOT beams co-propagate, sharing polarization and retroflection optics. The mirrors pictured have broadband dielectric coatings (Thorlabs EO2) which cover both wavelengths. Only linearly polarized light at either S- or P-polarized incidence is used to preserve polarization. Quadrupole and bias coil cross-sections are shown in orange and brown, respectively. *Key*—D: dichroic mirror, 2-QWP: two-color quarter waveplate.

species are a necessary starting point for degenerate mixtures. Therefore, the Rb and Yb MOTs must either have no spatial overlap or be loaded sequentially. At the cost of lengthening the duty cycle, sequentially loaded MOTs can operate at separately optimized field gradients, leading to larger, colder clouds. Both MOTs are generated with three retroreflected beams.[1] Linearly polarized, large diameter beams of 556 nm and 780 nm are combined on dichroic mirrors (custom coating by Thin Film Labs, dichroic coating reflects 556 nm at 45°, while the opposite side is AR coated for both wavelengths; we provided the substrates, 2" square windows from JML Optical) and subsequently circularly polarized with dichroic waveplates (Red Optronics custom order, 2" diameter; unlike most waveplates we order, these cannot be zero-order and actually have the opposite quarter-wave retardance, modulo integer wavelengths). As shown in Fig. 4.1, each beam is retroreflected with another dichroic waveplate to flip the circular polarization. Due to the imaging optics in the vertical direction (see

[1]For the Rb-only work described in Chapter 5, we used a 6-beam Rb MOT; now we are only using four ports of the 6-output fiber splitter/combiner (Section 3.5.1) to generate the Rb MOT beams.

Fig. 4.4), it was simpler to input vertical Rb MOT beams from both directions, but the vertical Yb MOT beam is retroreflected to conserve power. The additional optics also cause a strong power imbalance between the down-going Yb MOT beam and its retroreflection, resulting in a vertical position shift with increasing quadrupole field, which we utilize as a method to displace the Yb and Rb MOTs. MOT performance and typical beam parameters are summarized in Section 4.5.

4.2 Optical dipole traps

Optical dipole trapping relies on the ac polarizability of an atom in the intense electric field of a focused laser beam. The potential is due to the ac Stark shift (or "light shift"), which is calculated with second-order perturbation theory in the dipole approximation. While Grimm, provides an excellent review of dipole trapping [91], specific results are restricted to D1 and D2 lines of alkalis. As many excited states must be considered for the precision measurement of Chapter 5, the more complete approach of Mitroy, Safronova, and Clark in [92] is summarized here. Conveniently expressed in terms of an ac polarizability, the light shift is

$$\Delta E = -\frac{1}{4}\alpha_0(\omega)\mathcal{E}^2\,, \tag{4.1}$$

where $\mathcal{E}$ is the electric field strength. The dominant contribution due to the valence polarizability of an atom in state v can be expressed as a sum over states (in atomic units):

$$\alpha_0^v(\omega) = \frac{2}{3(2J_v+1)}\sum_k \frac{\langle k \parallel D \parallel v\rangle^2 (E_k - E_v)}{(E_k - E_v)^2 - \omega^2} \tag{4.2}$$

where we need only be concerned with the angular momentum J_v of fine structure for laser detunings large with respect to hyperfine structure. An additional contribution that is essentially frequency independent comes from the core electron polarizability. Each term in the sum over electronic states k is proportional to the square of a

reduced electric-dipole matrix element, $\langle k \,\|\, D \,\|\, v\rangle$, since this is the contribution of second-order perturbation theory. Depending on total angular momentum and detuning compared to fine and hyperfine structure, vector and tensor light shifts may be comparable to the scalar light shift.[2]

The intensity of a Gaussian laser beam propagating along $\hat{\mathbf{z}}$ is

$$I(x,y,z) = I_0 \frac{w_{0x} w_{0y}}{w_x(z) w_y(z)} \exp\left\{ -\frac{2x^2}{w_x^2(z)} - \frac{2y^2}{w_y^2(z)} \right\}, \tag{4.3}$$

where the peak intensity

$$I_0 = \frac{1}{2}\varepsilon_0 c \left|\mathcal{E}_0\right|^2 = \frac{2P_0}{\pi w_{0x} w_{0y}} \tag{4.4}$$

is conveniently calculated from the total beam power P_0. The $1/e^2$ radius of the beam is (for each transverse direction)

$$w(z) = w_0 \sqrt{1 + z^2/z_R^2} \tag{4.5}$$

with Rayleigh range,

$$z_R = \frac{\pi w_0^2}{\lambda}, \tag{4.6}$$

the distance from the minimum waist where the beam size has increased by $\sqrt{2}$. The intensity given in Eq. (4.3) is for an elliptical beam; when the minimum waists are equal in each transverse direction, the beam has cylindrical symmetry. Furthermore, in an astigmatic beam the minimum waists need not coincide, effectively reducing the peak intensity. Measuring and minimizing astigmatism is discussed in Section 4.3.

A single Gaussian beam provides strong transverse confinement, but the axial confinement, due to the curvature of the Rayleigh range, is much weaker. Thus, if

[2]There is no vector light shift for linearly polarized light, since it is proportional to $\boldsymbol{\mathcal{E}}^* \times \boldsymbol{\mathcal{E}}$. If far-detuned compared to fine structure, tensor light shifts require $J \geq 1$; if the detuning is not that large, there may be a tensor shift provided $F \geq 1$.

small or isotropic traps are desired, crossing beams must be used. Trap alignment becomes significantly harder since the relative alignment between beams should be stable at the micron level. With multiple beams, the intensity must be calculated from the *total* electric field. Interferences can be used to create optical lattice potentials. If two interfering beams are detuned, then the resulting lattice will travel at a velocity proportional to the detuning. For detunings large compared to the trap frequencies, the field changes faster than the atoms can respond, and one can simply consider the time averaged potential. For a crossed dipole trap generated from the same laser, detuning the beams by an AOM shift is typically sufficient for the resulting potential to be simply the sum of the intensities; independence can also be achieved with orthogonal polarizations.

Assuming all trapping beams are independent, the total light shift for a given atom is

$$U_{LS}^{\text{atom}}(\mathbf{r}) = -\frac{1}{2\varepsilon_0 c} \sum_{\text{beams } b} \alpha_0^{\text{atom}}(\omega_b) I_b(\mathbf{r}) \tag{4.7}$$

The total potential U also includes gravity for both atoms and magnetic fields for Rb. For atomic temperatures much less than the trap depth, the dipole potential is roughly harmonic with trap frequencies given by

$$U(\mathbf{r}) \approx \sum_i \frac{1}{2} m \omega_i^2 r_i^2 \,. \tag{4.8}$$

While simple analytic expressions are obtained for a single beam, the addition of a non-orthogonal crossing beam makes the algebra more complicated. Furthermore, the principal axes of the trap *rotate* as a function of relative power between the cross-trap beams. In practice, it is simplest to find the frequencies and axes of a multi-beam trap by diagonalizing the Hessian matrix of U, which is the Jacobian of the trapping force $(-\nabla U)$; such a procedure is implemented in the Mathematica code included in Appendix C.

4.3 Implementing two-color dipole traps for mixtures

Following the Görlitz group, we have also chosen to implement a two-color optical dipole trap which affords the flexibility to independently adjust trap depths for Rb and Yb. As described in Section 3.5.3 and Table 3.3, the 1064 nm dipole trap will be attractive for both Rb and Yb, although the Rb polarizability is more than four times larger; the 532 nm polarizability has approximately the same magnitude but is attractive (repulsive) for Yb (Rb).

The combination of optical and magnetic traps must initially be able to trap Yb atoms and exclude the Rb cloud while it is cooled. This can be achieved with a very large bias field to offset the quadrupole trap, but we have found that a single, small 532 nm dipole trap is sufficient to repel the hot Rb atoms. With a 20 μm waist, 8 W of 532 nm light will trap Yb with a depth of about 750 μK. The Rb atoms, whose temperature is less than 130 μK (see Fig. 4.5), see a barrier of more than 700 μK—many times their thermal energy. Once the Rb has been cooled by rf evaporation the trap must be modified so that the species can mix. A 1064 nm dipole trap can be turned on to counteract the repulsive 532 nm trap for Rb, but its waist must be equal to or smaller than the 532 nm waist to prevent a persistent barrier.

With many more Rb atoms in the quadrupole trap than dipole trapped Yb atoms, Rb is the natural choice as a sympathetic coolant. However, for sympathetic cooling to be efficient, the cooled species must have a much deeper potential than the coolant. The opposite is the case for Rb and Yb in a 1064 nm dipole trap, so two-color dipole traps are necessary for effective sympathetic cooling of the low abundance Yb isotopes. Additionally, the lattice experiments with superfluid immersion discussed in Section 1.2 will require tight confinement in 3D for efficient lattice loading. With Yb, this can only be achieved by adding a crossing dipole

trap. Finally, at the lowest temperatures and trap depths, we need to consider the differential gravitational sag between Rb and Yb. Given the polarizabilities, the Yb must be trapped more deeply to combat this with dipole power alone. We may also be able to use a moderate repulsive quadrupole field to lower the Rb cloud either by reversing the quadrupole current or the hyperfine spin projection.

The simplest initial geometry is coaxial 532 and 1064 nm beams with equal, coincident minimum waists. Then, the trap depth and radial potential at the center of the trap are equal for Rb and Yb with the appropriate power ratio:

$$\frac{P_{532}}{P_{1064}} = \frac{\alpha_0^{\mathrm{Rb}}(1064\text{ nm}) - \alpha_0^{\mathrm{Yb}}(1064\text{ nm})}{\alpha_0^{\mathrm{Yb}}(532\text{ nm}) - \alpha_0^{\mathrm{Rb}}(532\text{ nm})} \approx 1.02(5)\,. \tag{4.9}$$

However, because z_R for the 1064 nm trap is half that at 532 nm, the axial trapping of Yb and Rb will not match. Rb will have tighter axial confinement since it has the largest polarizability at 1064 nm. Choosing the right waist for the trapping beams proved an iterative process. It is necessary to balance the competing demands of efficient trap loading, which points to a large trap volume, and a high thermalization rate achieved with the higher density of a small trap. For our initial mixture experiments we found a 20 μm waist is a good compromise. While it is convenient to have steering mirrors after the final lens, the strong divergence of the 1064 nm beam makes it larger than a 1" optic if the focussing lens is too far from the chamber, which places a lower bound on the waist for a given lens. The final lens has a focal length $f = 250$ (500) mm in the horizontal (cross) direction, and the beam waist is selected by modifying the telescope so the incident beam radius is $w \approx f\Theta = f\lambda/(\pi w_0)$ at the focussing lens. As shown in Fig. 4.2, the 532 nm and 1064 nm beams must share the 250 mm focussing lens in the horizontal direction. To correct for the chromatic focal shift of the plano-convex lens used, the fiber collimation is tweaked to overlap each horizontal beam's minimum waist.

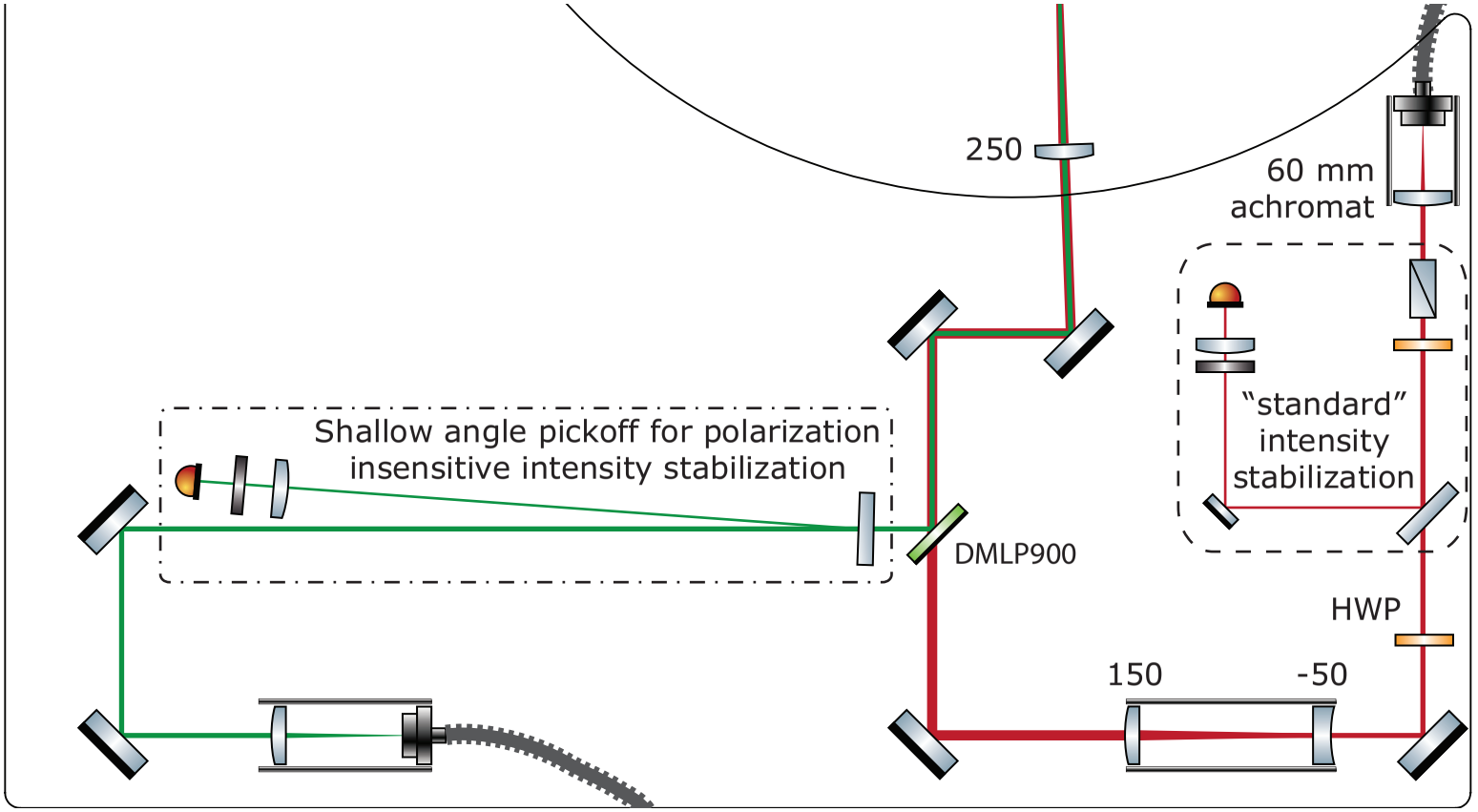

Figure 4.2: Fiber delaunch, combination and focussing optics for the 532 nm and 1064 nm coaxial dipole trap along the horizontal direction. The boxed regions show two implementations of intensity pick-offs for intensity stabilization. The reflectivity of the beam samplers is polarization dependent, so a Glan-laser polarizer defines a fixed pick-off fraction of the 1064 nm intensity (dashed box). As discussed later, the 532 nm polarization varies widely requiring the less precise shallow-angle pickoff shown in the dot-dashed box.

Dipole trap alignment begins with loading Rb into the horizontal 1064 nm beam input through the 2.75" viewports. With absorption imaging from the side and beneath, this is aligned to intersect the quadrupole trap center whose position is imaged without time-of-flight with a small number of Rb atoms. If a cross trap is used, the 1064 nm crossing beam is also aligned to intersect the quadrupole trap center. Once aligned to cross, a ball of atoms is present where the dipole beams intersect. For slight misalignment, this ball is observed to shift off center laterally to each beam; therefore tweaking the alignment to achieve the best centering from both imaging directions produces optimal crossing. To ensure that two beams cross, they can be imaged from two orthogonal directions. We have also set up absorption imaging along the edge of their crossing plane, attaching a camera and fiber port to either side of the other mini-cross direction (see Fig. 3.3). After roughly aligning the 532 nm dipole beams to copropagate with the 1064 nm beams, we use the Yb atoms to fine tune the overlap. Since both colors are attractive for Yb, we simply alternate between 532 and 1064 nm traps, ensuring that they are perfectly overlapped in 0.1 ms TOF absorption imaging from two directions.[3]

The alignment must be fine tuned daily, provided the lab temperature is stable to about 0.5 °C. However, tightening a clamping fork or adding or removing an optic mount anywhere on the platforms requires realigning the dipole traps. After alignment, the mixture loading and thermalization (Section 4.5.3) is quite repeatable day-to-day. To load the clouds with minimum heating, the waists of each horizontal beam need to be aligned and the atoms aligned to the waist. We have used a number of methods to determine the waist position of the horizontal beams. With a variable hold time after loading a cloud of atoms off-center, one can observe axial oscillations of the atoms at the axial trap period of order 0.1 s. For a hold many trap periods long, this motion has damped and the atoms sit at the trap minimum. With either

[3]This imaging is essentially *in situ*, however need a short time to turn off the dipole trap beams whose scatter otherwise degrades image signal-to-noise.

method, the focussing lens can be adjusted so that the focus is centered in the vacuum chamber. An alternate method to check that the waists of the 532 and 1064 nm coaxial beams coincide is to vary the power ratio with Rb in the dipole trap. As the repulsive and attractive balance changes, the axial minimum will translate if the waists do not overlap.

Directing the crossing dipole beams through the chamber proved challenging. The port axis is declined 21° from the mid-plane of the chamber. Currently, we are only relying on the cross for additional axial confinement when producing Yb BECs or Rb BECs without the quadrupole field. Therefore, the waist need not be as small as the horizontal beam. Allowing space for at least one mirror between the focussing lens and the chamber meant using a focal length of at least 500 mm. Were one to mount the final lens on the chamber (see Fig. A.5 for a 30 mm cage adapter), a 200 mm lens could also be used. In order to keep space on the optical table free for 556 nm MOT beam optics, the cross-beam optics were designed to be mounted on the underside of the breadboard (Fig. 4.3), which also has threaded holes. The schematic was first designed with CAD software (SolidWorks). This was especially useful in designing mounts for the pair of walking mirrors that take the beam from the plane of the breadboard and change its inclination to match the mini-viewport direction. While this sort of task is often accomplished iteratively by adjusting and remounting an optic until it is correctly oriented, making virtual adjustments in SolidWorks was much faster than adjusting optics hung beneath the breadboard. First, the beam path was defined as a 3D sketch; next, mirrors were assembled so that their normal bisected the beam angles. This left a rotational degree of freedom for the mirror mount orientation, which was used to keep the knobs as orthogonal as possible between the two mounts, facilitating straightforward beam walking. Finally, the appropriate wedged bases (Thorlabs AM16T and AM45C) were selected and oriented to provide a mounting surface coincident with the breadboard

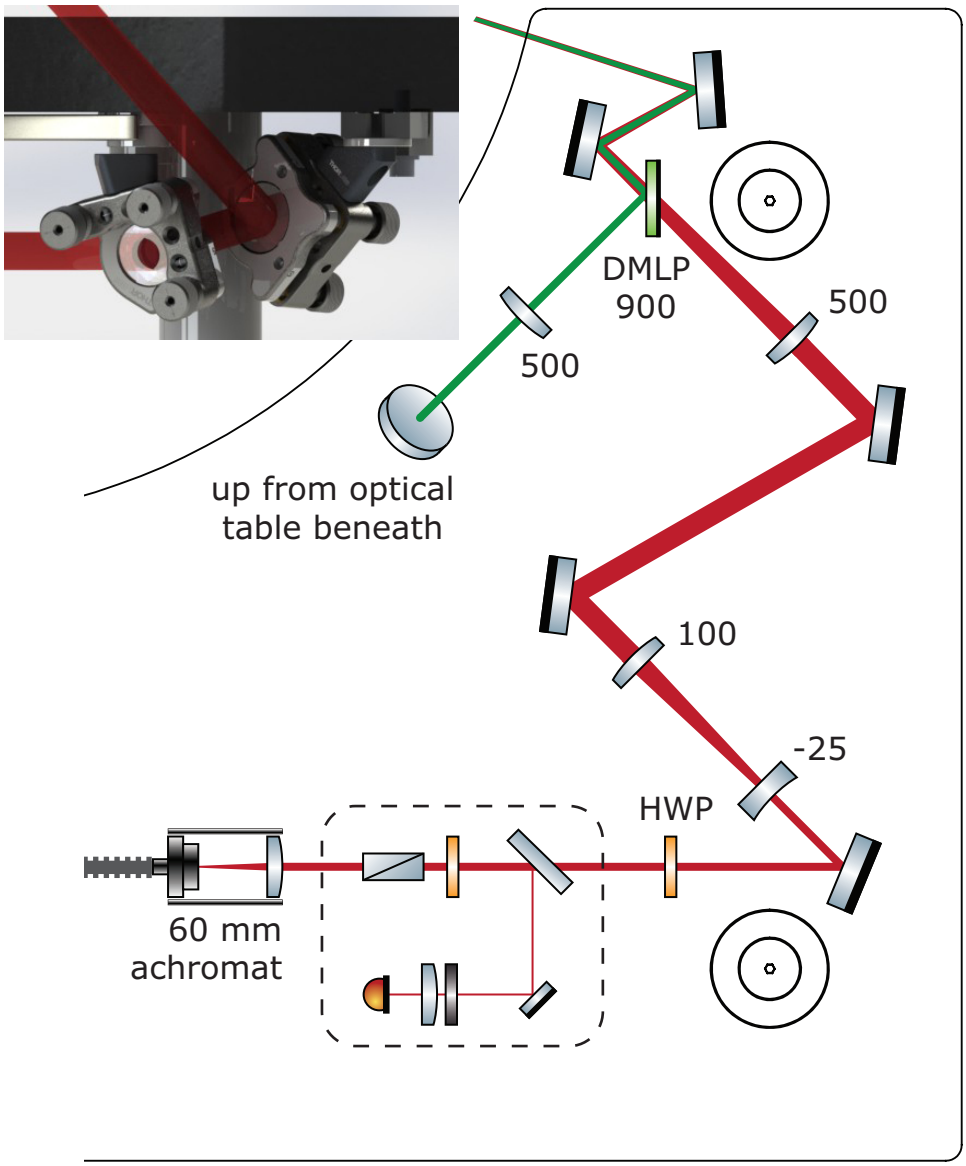

Figure 4.3: Optical schematic for the crossing dipole beams, viewed from beneath. At the top of the figure, the 532 nm and 1064 nm beams are combined on a dichroic mirror (Thorlabs DMLP900), and subsequently are sent up through the chamber at an inclination of 21°. 1064 nm intensity lock optics are inside the dashed rectangle, immediately after the fiber collimation. Inset: Side-view of the final two mirror mounts.

for each mirror mount.

When constructing the dipole trap optics and testing the setup with the atoms, we encountered a few unexpected issues. First, thermal lensing is more prevalent at visible wavelengths than in the NIR. Early on, we constructed a 2x telescope for a 532 nm beam from a pair of N-BK7 lenses. Observing the beam profile on a camera one meter downstream from the telescope, one could watch a hole grow in the center of the beam over seconds after suddenly switching on a few watts of 532 nm. For all our high power beams, we are now careful to use fused silica optics which have a thermal expansion coefficient nearly ten times smaller than other common optical glasses.

In an attempt to promote long-term stability we used ultra-stable stainless steel mirror mounts (Thorlabs Polaris-K1). These mounts were designed to exhibit repeatable positioning below two μrad after thermal cycling; additionally, they have 100 thread-per-inch actuators with a smooth action enabling precise manual control at the few μrad level. However, early versions of the product specification sheet recommended using significant torque to secure the optic to prevent it from shifting due to differential thermal expansion. We discovered, after much headache, that the optic set screw was the source of persistent astigmatism of the dipole beam. The astigmatism of the beam was quantified by measuring the waist profile over a few z_R on either side of the minimum spot. This was accomplished with a short focal length lens and a beam profiling camera on a translation stage. We found that the minimum waists were offset by nearly a full Rayleigh range in the two transverse directions. After trying to remove the astigmatism with careful lens alignment, we eventually noticed that the orientation of the astigmatic profile was at $\pm 45°$, which matched the set screw orientation. Loosening the set screw and applying just enough torque to contact the mirror has fixed the astigmatism. Subsequently, Thorlabs quietly changed the recommended set screw torque to 1/10 their original

specification.

Our first two-color dipole trap used 532 nm trapping light free-spaced over about 1.5 m to the chamber, while the 1064 nm light was fiber-coupled. Due to the short distance between the 1064 nm fiber and the chamber, we found that we needed to adjust the 1064 nm beam very little each day when aligning the coaxial trap. However, we soon discovered relative alignment was a problem at faster timescales, too. Working with a Rb BEC, we examined the lifetime in a set of two-color traps with roughly fixed trap depth but increasing total power. The more 532 nm power we used, the shorter the Rb lifetime became, presumably due to large potential fluctuations from pointing instability. After adding a fiber (NKT Photonics LMA-PM-10, 5 m length, high-power SMA905 connectors) for the 532 beam also, both long and short term stability are greatly improved.

However, as alluded to in Section 3.5.3, fiber coupling watts of 532 nm light has some limitations. The most power we have been able to couple through the fiber is about 10 W. Despite working hard to match the numerical aperture (NA) of the fiber and achieving very high coupling efficiency at low power, high power transmission always suffered. We are convinced thermal lensing in the coupling optics was not the main cause, having tried longer focal length fused silica lenses in addition to short focal length aspheres. Above about 4 W of transmitted power, the coupling throughput dives sharply, and we are only able to get up to 10 W by rotating the input polarization away from what was PM matched at low power. This is further evidence that there is some polarization-dependent material interaction within the fiber that seems to be limiting its capacity despite the large mode area provided by the photonic crystal structure. Without PM matching, we have had to modify our usual intensity lock measurement to make it as insensitive to polarization as possible. At 45° incidence, the reflection off the beam sampler (Thorlabs BSF10-A) varies between about one and ten percent for S- and P-polarization. A Glan-laser

polarizer is typically used to set a fixed pick-off fraction. We have observed the 532 nm beam polarization rotate strongly out of the fiber so that at times we would lose most of the power at the polarizer, limiting the locked power to about 2 W. In order to preserve higher power operation, we have used a very shallow angle pick-off (as shown in Fig. 4.2) which minimizes the reflectivity difference between S and P. While the intensity lock stability is worse than usual, it is good to a few percent, and we have observed it to improve significantly the Rb number stability in the two-color dipole trap.

4.4 Imaging

We monitor the initial cooling and trapping stages of any experiment in multiple ways. A small security camera provides a live image of the 3D-MOTs as viewed through one of the mini-viewports along the main dipole beam. Another video monitor is used to diagnose the Yb 2D-MOT alignment. Low-magnification absorption of both Rb and Yb along the horizontal direction provides MOT and quadrupole trap diagnostics as well as dipole alignment and loading performance. Probe beams for each atom are fiber coupled, and we swap fibers to switch between Rb and Yb horizontal imaging. The wide field in the horizontal direction allows us to measure temperatures $1-500\ \mu$K by varying TOF up to 25 ms without needing to reposition the camera (Point Grey Flea2 FL2G-13S2M[4]).

High-magnification imaging is implemented in the vertical direction with probe beams directed down through the 1.5" bore in the center of the quadrupole coils. This direction is convenient since TOF can easily be used to fine-tune the focussing despite the short depth of field. As shown in Fig. 4.4, the vertical direction is quite crowded. Above the chamber, the 780 nm probe and MOT beams are combined on

[4]This sensor has much higher quantum efficiencies than others sold by Point Grey: 50 (25)% for 399 (780) nm.

a polarizing beam splitter (PBS), while the Yb MOT and 399 nm probe beams are added with dichroic mirrors (D and D2, respectively). They are all sent through a dichroic quarter waveplate for 556 and 780 nm. Below the chamber, a single collection lens (L1: 75 mm achromat, Edmund Optics 49-358) for both Rb and Yb absorption imaging is inserted within the magnet coil, and a second dichroic waveplate returns the MOT beams to linear polarization. Another dichroic mirror (D2) splits off the 399 nm probe beam to the Yb imaging camera. Two meniscus lenses (L2: 125 mm Thorlabs LE1156-A, L3: -100 mm Thorlabs LF1822-A) correct aberrations at 399 nm and give an effective collection focal length of 61.8 mm. The final focusing lens is a 200 mm achromat (L4: Thorlabs AC254-200-B) and sets the magnification.

The dichroic mirror (D2) will also reflect 423 nm light, meaning vertical lattice beams could easily be combined via polarization onto the 399 nm beam path; alternately, it is also possible to bring in vertical lattice beams on either side of the collection lens, which cross in the center of the chamber at a shallow angle and must subsequently be folded above the chamber and returned. When imaging Rb, a flipper mirror directs the 780 nm probe light to the Rb camera through two 150 mm achromats (L6: Thorlabs AC254-150-B). Otherwise, the Yb MOT light is separated with a dichroic mirror and retro-reflected, while a separate up-going Rb MOT beam is also combined onto the path. Despite going through the collection lens, both MOT beams are collimated in the center of the chamber due to the relay lens (L5: 150 mm achromat, Edmund Optics 49-391) at the bottom.

It is useful to image Yb and Rb atoms in the same experimental shot. While this could be done on separate portions of the same camera, the paths must be split to account for chromatic focal shift and aberrations between 399 and 780 nm imaging light. Sequential imaging with different TOFs for Rb and Yb could correct for the focal shift without splitting the paths, but this would leave chromatic aberrations

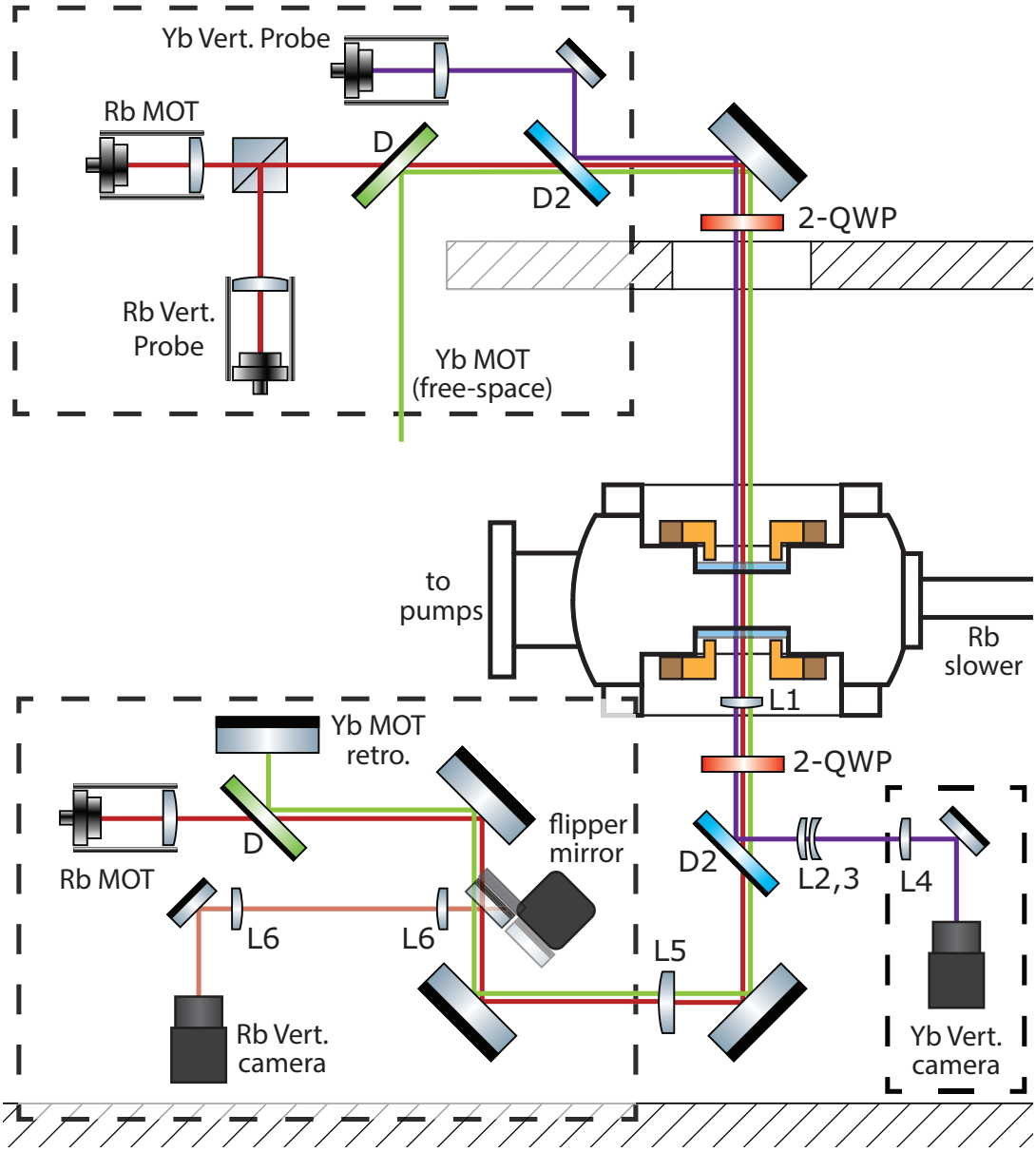

Figure 4.4: Schematic of the vertical imaging system, viewed from the side. Many dichroic mirrors are used to combine Yb and Rb MOT beams with vertical absorption imaging beams for both species. The portions of the schematic in dashed boxes are actually in the horizontal plane. The cross-section of the quadrupole and vertical bias coils are shown in orange and brown, respectively. *Key*—D: dichroic mirror (MOT), D2: dichroic 399nm probe, 2-QWP: two-color quarter wave plate (556/780 nm), L1-6: imaging lenses, see text.

uncorrected. We have chosen to use separate cameras from Point Grey (Flea3 FL3-FW-03S1M). Despite having a smaller sensor area and larger pixel size, this Flea3 model has slightly higher quantum efficiency than the Flea2G used in the horizontal direction. These cameras have FireWire (IEEE-1394b) connectors, and we have found that simultaneous triggered operation of the cameras requires each to be on a separate bus otherwise they automatically synchronize to each other's triggers. And with each camera on its own FireWire card, they can each operate at maximum transfer speed, minimizing the time required between images. To simplify controlling multiple cameras, new image acquisition software was written in LabVIEW.

4.4.1 Extracting physical parameters from images

Absorption imaging and processing has been reviewed in detail in [65]. Throughout the larger group at JQI, basic image processing is performed after every experimental shot using the scripting language within Igor Pro. Each experiment tends to specialize the Igor scripts to reflect their particular apparatus's trapping geometry, therefore they are not included here.

4.5 Apparatus performance

In this section, typical benchmarks for the RbYb apparatus performance are presented. First, we will give typical trajectories to BEC for Rb or Yb alone. These benchmarks are with the same MOT loading and dipole trapping dictated by mixture requirements. In the case of Rb, the hybrid trap volume is about ten times smaller than typically used in our group, resulting in smaller condensates. For Yb, our first BECs were obtained with 30-40 μm waists in a 532 nm only cross-trap. The results presented in Section 4.5.2 utilized a 24 μm horizontal 532nm dipole beam, and are similar to the performance of the two-color horizontal trap detailed in Section 4.5.3.

All reported values are representative of typical, daily apparatus performance.

4.5.1 Rb BEC

We load around 3×10^9 atoms in the Rb MOT in 6 s. The MOT gradient along the vertical direction is 13.6 G/cm, while the MOT beams are detuned -24 MHz below the cycling transition and each contain 14 mW over a diameter of about 2.5 cm. There is also 0.22 mW of repumper on each beam, with an optimal detuning determined empirically to be 5 MHz blue of the $F = 1 \rightarrow F' = 2$ "repump" transition. The Rb slower currents are 36 (30) A in the positive (negative) sections. The slower beam is circularly polarized and detuned -144 MHz from resonance with 22 mW focussed just beyond the oven nozzle. With orthogonal polarization, the slower repump contains 8.6 mW and is detuned -68 MHz from the repump transition.

At the end of the MOT stage, the slower light is turned off, and the MOT repumper power is reduced by a factor of nearly 100. While the atoms at the edge of the cloud are still repumped, central atoms fall into $F = 1$ and stop scattering photons, reducing the internal radiation pressure and increasing the MOT density. This "temporal dark spot" stage lasts 20 ms, after which the MOT detuning is switched to -160 MHz without lowering the power for a 7 ms molasses, during which the sub-Doppler polarization gradient cooling reduces the cloud temperature to 40 μK. Then, the repumper is turned off completely for 1.5 ms to pump all atoms into $F = 1$.

We initially capture atoms in the quadrupole trap at 44 G/cm for 110 ms to match the large size of the Rb cloud after the molasses stage. The quadrupole zero is biased for best overlap, empirically optimizing for highest captured number. During the capture stage, the 1064 nm horizontal dipole trap is switched on at 300 mW. This provides a trap depth of around 75 μK, and we have observed deeper traps to cause significant heating during the loading stage. The quadrupole trap is

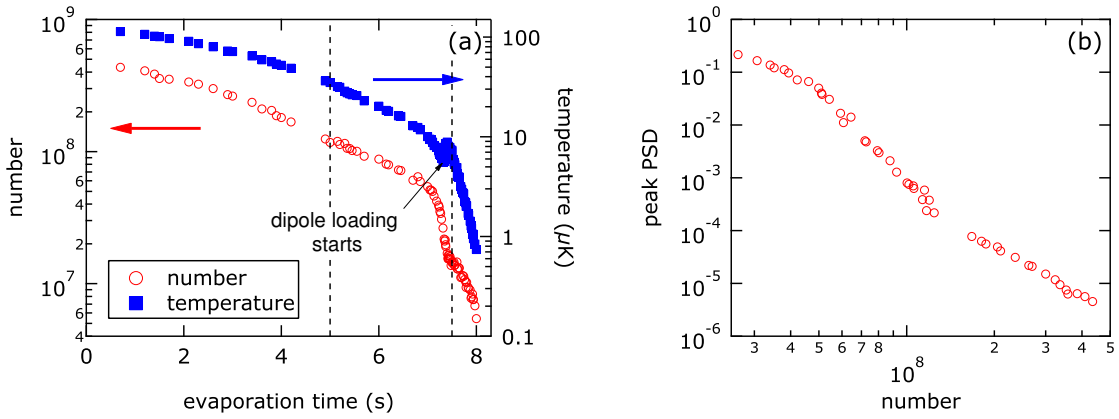

Figure 4.5: (a) Evaporation of Rb in the quadrupole and hybrid traps. Three experimental stages of evaporation are separated by dashed vertical lines: rf evaporation in the quadrupole trap, decompression and rf evaporation to load the hybrid trap, and evaporation in the hybrid trap. (b) Peak phase-space density ($D = n_0\Lambda^3$) gained during evaporation. D was only calculated before the atoms were loaded into the quadrupole plus dipole trap.

ramped adiabatically to 187 G/cm over 1 s. While this compression increases the atom temperature to 130 μK, the increased density lowers the thermalization time and allows us to evaporate faster. In the compressed quadrupole trap ($t = 0$) in Fig. 4.5, rf evaporation is performed linearly, ramping from 18 to 5 MHz over 5 s. Then, the quadrupole trap is lowered to 20.6 G/cm, with a linear ramp over 2.5 s while the rf knife is further lowered to 1 MHz. This adiabatic decompression quickly lowers the temperature, while continued rf evaporation further increases the phase space density. As seen in Fig. 4.5, the atom number drops sharply around 7 s and the temperature increases slightly. At this point, the atoms are loading into the dipole trap and gain some kinetic energy as the trap depth is higher than the atom temperature.

The final evaporation to a BEC is forced with an exponential ramp of the dipole power from 300 to 12 mW over 0.8 ms ($1/e$ time of 0.25 ms). A vertical magnetic gradient of 30.5 G/cm would exactly cancel gravity for Rb, and with a smaller gradient, atoms evaporate out of the bottom of the hybrid trap. Final radial (axial) trap frequencies are about 200 (30) Hz, with approximately 10^6 atoms in the

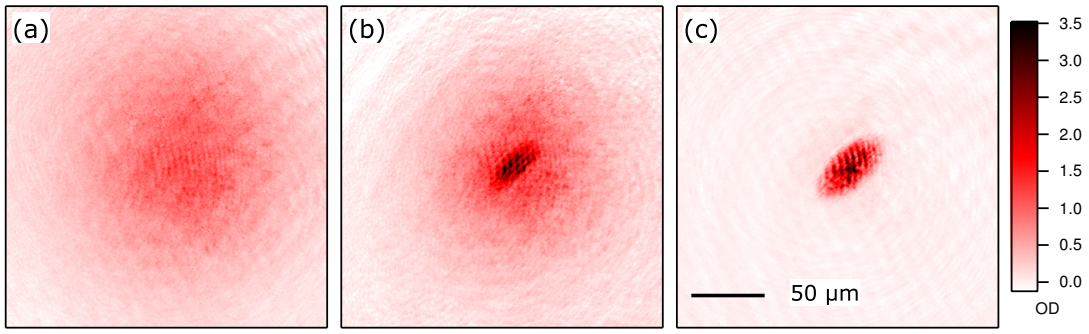

Figure 4.6: Crossing the BEC transition with ^{87}Rb. All images are after 35 ms TOF. (a) Thermal cloud just above T_c. (b) Bi-modal distribution showing thermal cloud and small condensate. (c) Nearly pure BEC. With the dipole trap roughly along the main diagonal, we see the aspect inversion characteristic of anisotropic confinement of a BEC.

condensate. With such a tight trap, the BEC first appears at T_c of about 1 μK.

4.5.2 Yb BECs

Without the large quadrupole trap for initial trapping, loading Yb into a dipole trap is much less efficient than for Rb. Additionally, the Yb MOT loading rate is less than Rb, and we load the Yb MOT for 20 s. As shown in Fig. 4.7, the Yb MOT has a very long loading time constant. 2D-MOT parameters are as described at the end of Section 3.3. Initially, the quadrupole gradient is 1.9 G/cm, and the 556 nm MOT beams are broadened with frequency modulation (FM) of the MOT AOM to increase the capture velocity. The FM drive sweeps the MOT frequency at 400 kHz and is centered 6.3 MHz below resonance, resulting in a spectrum with about 12 teeth (Fig. 4.8) spread over 4 MHz (8 MHz after double-pass), measuring the width 20 dB below the peak. The broadened MOT has 35 mW per 1.5 cm diameter beam. The low gradient and broadened MOT light results in a low atom density and enables us to load 5×10^8 atoms in 20 s.

For more efficient transfer to the dipole trap we need to compress the MOT for better overlap. This is done in two stages. First, the FM is turned off over 200 ms leaving only a single MOT tone -3.6 MHz detuned from resonance with

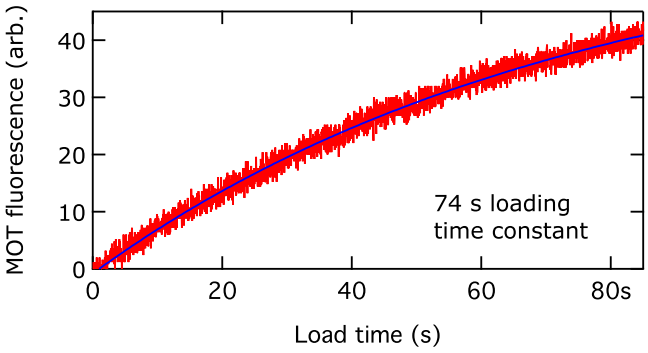

Figure 4.7: Fluorescence from Yb MOT load. The $1/e$ loading time of the Yb MOT is very long due to the low density.

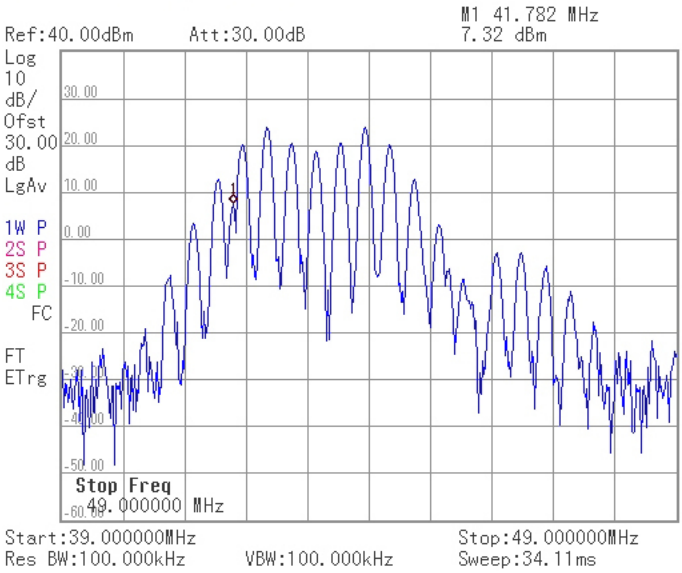

Figure 4.8: Spectrum of broadened 556 nm MOT AOM drive rf (log scale). Resonance is at exactly 40 MHz, with red detuning at higher frequencies (see Fig. 3.26).

0.7 mW per beam. During this step, the gradient is also increased linearly to 11.3 G/cm. Then the horizontal dipole trap is switched on, and the MOT beam power is further reduced by a factor of 4 in 100 ms while the shimming fields are ramped to final values which overlap the MOT with the dipole trap. The increased gradient and reduced scattering rate both compress and cool the atoms as low as 12 μK. In the compressed MOT, the restoring force barely balances gravity causing bosonic clouds to sag to the bottom of the trap. This also significantly reduces both the MOT lifetime and number stability, limiting the duration of this stage. At this point atoms have loaded the dipole trap and the MOT beams are switched off.

Our first experiments with dipole trapping Yb were with ^{174}Yb using a crossed 532 nm dipole trap with 24 (28) μm waists for the horizontal (crossing) beams. We were able to trap more atoms with a 30 to 40 μm horizontal waist, but the axial trap frequency was so low that thermalization was slower than the trap lifetime making it impossible to evaporate the atoms into the shallower crossed-trap. Further trap refinements are described in Section 4.5.3. Beginning with 10 W and 1.5 W in the horizontal and cross beams, respectively, atoms initially are only visible in the horizontal beam. Over a few hundred ms, the atoms are observed to spread along the dipole trap axially. After the MOT is switched off, evaporation proceeds in two steps. First, the horizontal beam was reduced exponentially for 2 s with a $1/e$ time of 1.5 s, after which the atoms are nearly all in the "dimple" of the crossed-trap. Second, with a 2.8 s time constant, both beams are evaporated together for 6 s, resulting in a pure BEC of few 10^5 atoms, as shown in Fig. 4.9.

We have also condensed ^{170}Yb in a similar procedure. Due to the ten times lower natural abundance and less efficient evaporation, we required an 80 s MOT load for about 2×10^4 condensate atoms. As discussed in Table 2.2, ^{172}Yb and ^{176}Yb cannot be condensed due to collapse, and ^{168}Yb would take another 20 times longer to load the MOT, making it impractical.

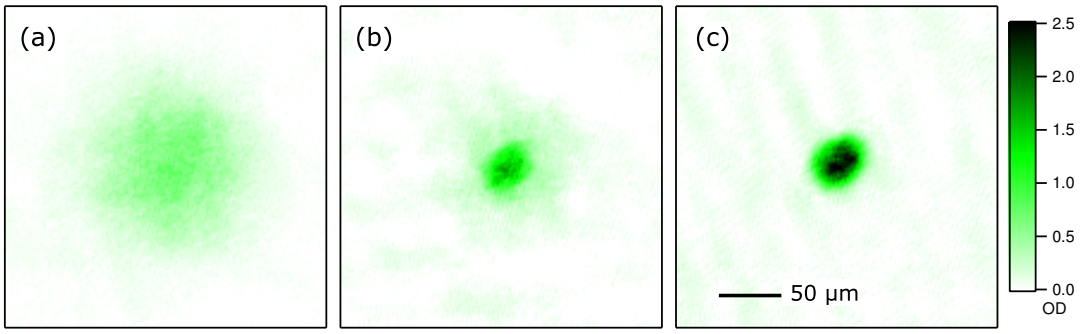

Figure 4.9: ^{174}Yb BEC in a 532 nm crossed-dipole trap (10 ms TOF). (a) Thermal cloud, (b) Bi-modal distribution, (c) pure BEC. The BEC appears round because the trap frequencies in the cross trap are similar when viewed from below.

4.5.3 RbYb mixtures

The first indication of density overlap in a mixture of Rb and Yb atoms is that their temperatures equilibrate. Fig. 4.10 shows cloud width fits during a variable TOF to extract the temperature. The procedure was repeated with both species and with each separately. Yb MOT loading parameters were identical to those in Section 4.5.2. The dipole trap consisted of 532 nm plus 1064 nm coaxial horizontal beams with 21(2) μm waists. Upon compressing the Yb MOT, the atoms were loaded into the dipole trap with 10 and 1.7 W of 532 nm and 1064 nm light, respectively. Subsequently, the Rb MOT was loaded for 6 s with a vertical displacement of 5 mm from the dipole trapped Yb atoms provided by a 5.5 G bias field. Otherwise, the cooling and evaporation were identical to Section 4.5.1. During the quadrupole compression, the 532 nm beam power was reduced with a linear ramp to 4 W. The Rb atoms were initially repelled by the total dipole potential, but they were brought into thermal contact with the Yb atoms by the end of the rf evaporation by ramping off the bias field.[5] Finally, the Rb atoms were cooled further and loaded into the dipole trap with a 2 s decompression ramp. After a 1 s hold in the two-color dipole trap, the atoms were released and one species was imaged after a varying TOF.

[5]Recall that this magnetic displacement of the Rb does not affect the dipole trapped Yb atoms since they are in the $^1S_0$ state.

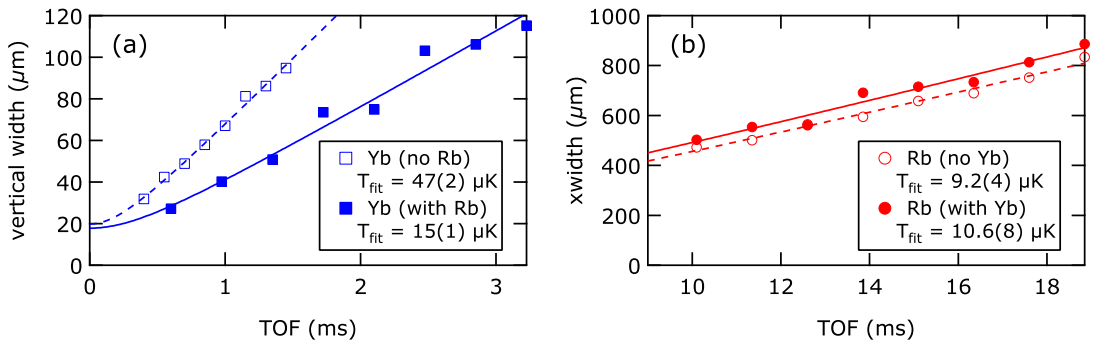

Figure 4.10: Sympathetic cooling in a mixture of (a) ^{172}Yb and (b) ^{87}Rb. An approximate temperature is extracted from cloud growth during short to moderate TOF. Both species were imaged from the horizontal direction with (closed symbols) and without (open symbols) the other atom. Reduced chi-squared for the fits has not been reported due to known imaging systematics (described in the text). We calculate the peak Rb (Yb) density is 7×10^{13} (2×10^{14}) cm^{-3} in the mixture.

As shown in Fig. 4.10(a), the presence of the Rb reduces the final Yb temperature by about a factor of 3. Without Rb, the mean Yb number over the temperature measurement sequence is $2.4(1) \times 10^6$ while it is drops to $1.9(1) \times 10^6$ when Rb is present. The Rb temperature with and without Yb is essentially consistent. We calculate that the Rb (Yb) trap depth at the end of the mixture procedure is 60 (480) μK. Since it sees a significantly shallower trap, the Rb acts as the coolant, and its temperature is fixed by the trap depth whether Yb is present or not. The Rb number is reduced from $2.7(1) \times 10^6$ to $2.2(1) \times 10^6$ when Yb is present. Despite the large reduction of Yb temperature, the Rb number remains high because the quadrupole trapped atoms, many of which are not loaded into the dipole trap, also act as a preliminary coolant.

The fitted Rb and Yb temperatures in the mixture are not identical, which is at least partially attributable to imaging resolution. The radial trap frequency is higher for Yb while it has a much lower axial frequency. This means the Yb atoms have too low an OD to image effectively beyond a few ms TOF. At such early times of flight, the vertical cloud width is less than 10 pixels across, and size measurements are limited by our imaging resolution. Additionally, with its large axial extent, the entire

Yb cloud is not in focus. It is unlikely that the clouds have not thermalized since we expect a 4 μK temperature difference to give an instantaneous thermalization rate of 900 s^{-1} from Eq. (4.10), which is the generalization of Eq. (2.18) to a trap which a different scaling (β_i) between species in each direction:

$$\tau^{-1} = \frac{4(N_1+N_2)\sigma_{12}\xi\bar{\Omega}^3}{3\pi^2 k_B} \frac{\left(\frac{T_1}{2m_1}+\frac{T_2}{2m_2}\right)^{1/2}}{\prod_{i=x,y,z}\left(T_1+T_2\beta_i^{-2}\right)^{1/2}}\,. \tag{4.10}$$

where ξ is given in Eq. (2.13) and $\bar{\Omega} = (\Omega_x\Omega_y\Omega_z)^{1/3}$. The potentials for each species are given by

$$U_1 = \textstyle\sum_{i=x,y,z} \Omega_i^2 r_i^2 \tag{4.11}$$

$$U_2 = \textstyle\sum_{i=x,y,z} \beta_i^2\Omega_i^2 r_i^2\,, \tag{4.12}$$

where $\Omega_i^2 = (m_1/2)\omega_{1i}^2 r_i^2$ and $f_{1i} = \omega_{1i}/(2\pi)$ is the harmonic trap frequency in the ith direction for the first species. For the horizontal two-color trap, with or without quadrupole confinement, the two radial directions are identical provided gravitational sag can be neglected; this is the case for the experiment in Fig. 4.10 since the calculated radial trap frequencies are 2.4 and 1.2 kHz for Yb and Rb, respectively; the 46 Hz axial trap for Rb is stiffer than Yb at 18 Hz. The potential is plotted in Fig. 4.11.

We have also initially explored mixtures of ^{87}Rb with ^{174}Yb and ^{176}Yb. However, due to large, repulsive interspecies interactions, we have observed phase separation once the temperature is low enough. Fig. 4.12 shows Yb clouds with and without Rb at a temperature of 7 μK. In the mixture, the Rb atoms exclude the Yb from the center of the trap. Mixtures with ^{176}Yb have also displayed phase separation. With both isotopes, phase separation occurred for thermal mixtures above the critical temperature for condensation.

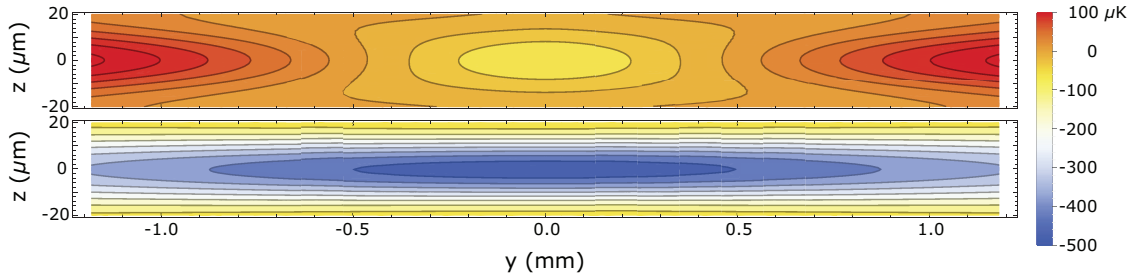

Figure 4.11: Rb (Yb) potential contours on top (bottom) for the dipole plus quadrupole trap used in Fig. 4.10 thermalization. The z-axis is the radial direction (identical to x as gravity is negligible), while y is along the axis of the beam; note the different unit scales. The trap consists of 4 W of 532 nm and 1.7 W of 1064 nm light, each with 20 μm waist. The repulsive lobes on either side of the Rb trap are due to the Rayleigh range difference between the two dipole wavelengths. Additionally, a 24 G/cm quadrupole trap provides additional Rb confinement.

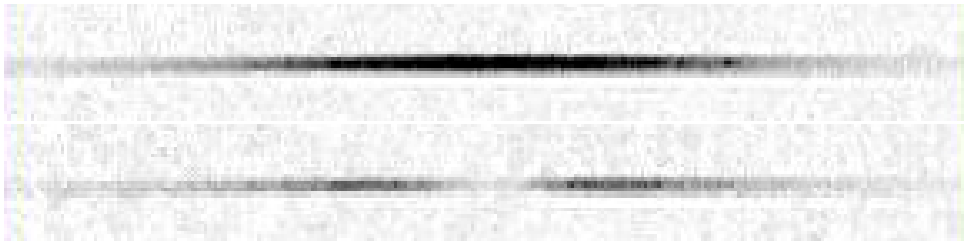

Figure 4.12: ^{174}Yb atoms in the two-color dipole trap without (top) and with (bottom) ^{87}Rb. The images are 3 mm wide and were taken after a short TOF. Well above T_C, the mixture still exhibits phase separation due to very large interspecies repulsion.

4.6 Future work

Despite fiber-coupling both horizontal dipole beams, the relative alignment tends to drift over a few hours, which may be an issue for long data runs. Having demonstrated thermalized mixtures with densities near 10^{14} cm^{-3} for both species, we have begun searching for RbYb* photoassociation on the $^3P_1$ transition. As discussed in Section 1.3, further molecular spectroscopy is needed to predict the viability of optical Feshbach resonances. There is also much work to do optimizing the Yb procedure for fermions. With the apparatus reliably producing ultracold mixtures, we are poised to introduce the 423 nm lattice and begin superfluid immersion investigations.

Chapter 5: Precision Measurement: Rb $6p$ Light Shift

During the extended construction of the RbYb mixture apparatus, we followed several side roads. The most fruitful resulted in the first experimental determination of the $\langle 5s \,\|\, D \,\|\, 6p_j \rangle$ matrix elements of Rb. Published in collaboration with Marianna Safronova [93], our new technique overcomes the limitations of existing lifetime and photoassociation measurements to extract higher-lying excited state matrix elements to better than 0.3 %. This chapter is largely based on [93] and adds a description of the numerical simulation I performed to extract light shifts from the diffraction data.

5.1 Motivation

Precise knowledge of atomic transition strengths is important in many current areas of research, including the development of ultra-precise atomic clocks [94–96], studies of fundamental symmetries [97,98] and degenerate quantum gases [99], quantum information [100, 101], plasma physics [102], and astrophysics [103, 104]. For example, one of the largest contributions to the uncertainty budget of atomic clocks is the uncertainty in the blackbody radiation (BBR) shift [95, 105]. The BBR shift is calculated from the difference in the electric-dipole polarizabilities between the clock states [106], and its accuracy is currently limited by uncertainty in atomic transition matrix elements. The dynamic correction to the BBR shift can also be determined accurately if the relevant matrix elements are known [94]. Studies of fundamental symmetries, such as atomic parity violation, need transition matrix

elements to evaluate parity-violating amplitudes and vector transition polarizabilities [97, 98]. Accurate atomic theory can also be indispensable to the design and interpretation of experiments, where direct measurement of all relevant parameters is infeasible. More complicated atoms, such as Er [107], Dy [108], and Ho [109] have recently become of interest, and development of new theoretical methods must be supported by the existence of high-precision experimental benchmarks.

5.2 Determining matrix elements

Transition matrix elements can be difficult to measure or calculate accurately. State-of-the art theory predictions are often limited to a few percent uncertainty, and the presently available experimental techniques typically measure matrix elements accurately only for one or two of the lowest transitions. To date, the most accurate determinations of atomic transition matrix elements are through excited state lifetime measurements or photoassociation spectroscopy [110]. The former is limited by uncertainty in branching ratios when multiple decay paths exist. As a result, although the $6p$ lifetime of rubidium was measured to 1%, no matrix elements were reported [111]. The latter requires species with purely long-range molecular excited states where molecular theory is sufficiently well known to extract atomic properties. In principle, transition matrix elements can be determined from the ac polarizability α by measuring the ac Stark (light) shift of an atom exposed to light of known intensity. However, unlike dc Stark shift measurements, where the applied electric field can be determined geometrically [95], it is difficult to accurately determine the optical intensity, limiting the efficacy of this approach. (Lifetime measurements avoid this calibration challenge by using a well known field, the vacuum.) For atoms with spin-dependent vector light shifts and two long-lived states, rf spectroscopy was used to accurately determine the *ratio* of two vector light shifts [112, 113], which when combined with theory constrained matrix elements [114]. New techniques are

needed to improve accuracy, extend the range of measurable matrix elements, and provide benchmarks for theory.

Here, we present a widely applicable method, recently suggested in [115], for constraining matrix elements at the 10^{-3} level through direct measurement of light shifts near "magic-zero" wavelengths (λ_{zero}), where the combined light shift from all transitions cancels.[1] These λ_{zero} wavelengths are distinct from the "magic" wavelengths used in optical clocks, where the light shift is identical for two states [116]. We measure small light shifts through diffraction off a standing wave, amplifying the diffracted populations by constructively interfering the effect of up to $n_p = 15$ pulses, resulting in an n_p^2 enhancement in the diffracted fraction. We make the first experimental determination of the rubidium $5s$-$6p_{1/2}$ and $5s$-$6p_{3/2}$ electric dipole matrix elements, to an accuracy of 0.3%, 10 times more accurate than the best theoretical values [115].

Measuring light shifts near a λ_{zero} to constrain matrix elements has a number of advantages over the approaches described earlier. It is insensitive to absolute calibration of the applied optical field, requiring only a stable intensity. Scalar light shifts are present for all atomic states, and λ_{zero} points are found near every atomic transition. That proximity increases sensitivity to the matrix element of the nearby transition in addition to decreasing sensitivity to uncertainty in hard-to-calculate theoretical values. Most importantly, ground (or metastable) state light shifts depend only on matrix elements directly to higher excited states, not on the coupling of the excited states to other states. Light shift measurements are thus independent of the branching ratios that limit the lifetime approach.

[1] These are the "tune-out" wavelengths proposed for species-selective traps by [24].

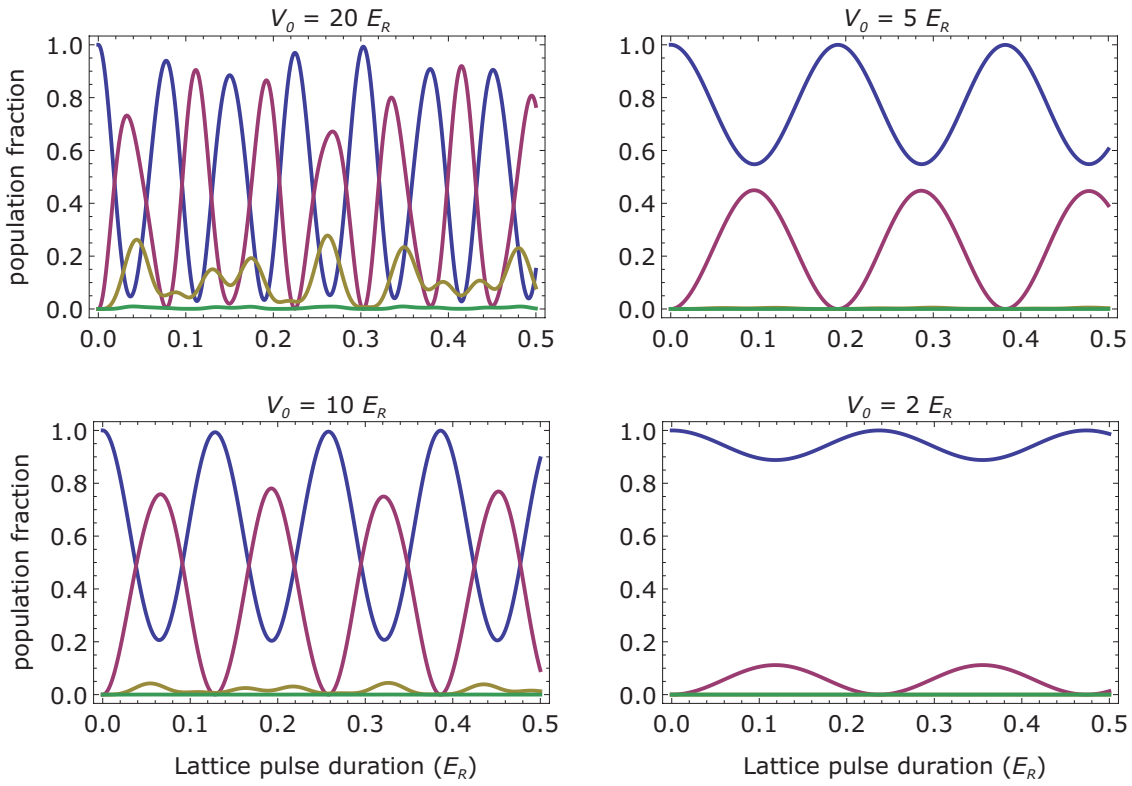

Figure 5.1: Kapitza-Dirac diffraction from a single lattice pulse. The expected populations with momenta 0 (blue), ±2 (purple), ±4 (yellow), and ±6 (green) $\hbar k$ are shown.

5.3 Measuring small light shifts with multi-pulse diffraction

Optical lattice depths (light shifts) are commonly measured by observing the population oscillations between momenta $2l\hbar k$, for integer l, as a function of lattice pulse duration (outside the Raman-Nath regime). The populations of these diffracted orders are straightforward to calculate numerically, as described in Appendix D. Fig. 5.1 shows our calculation of expected diffraction for a few typical lattice depths. For moderate lattice depths, the population oscillations are sinusoidal. However, for lattice depth $\gtrsim 10\ E_R$ (where the recoil energy $E_R = \hbar^2k^2/(2M)$ for wavevector $k = 2\pi/\lambda$, lattice laser wavelength λ, and atomic mass M), the patterns are more complicated but still periodic. Fig. 5.2 displays how the band energies for zero momentum ($E_{n,q=0}$) change with lattice depth. When only one diffracted order

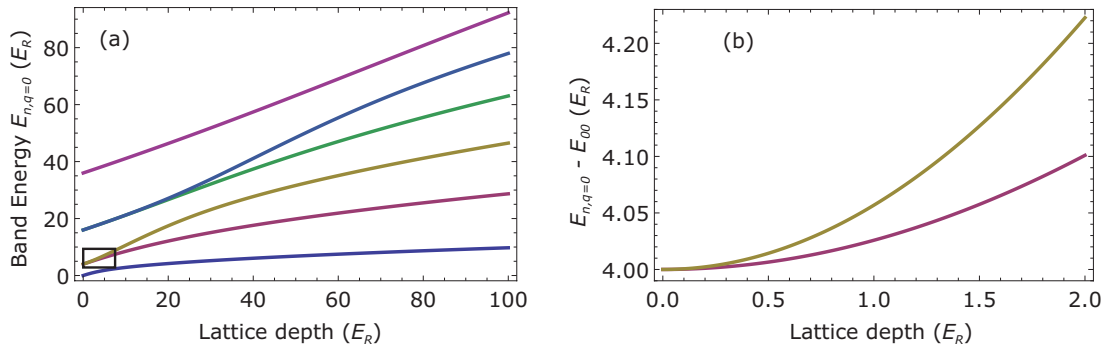

Figure 5.2: Band energies at $q = 0$ with increasing lattice depth. (a) Bands 0 through 5 are shown from bottom to top. Note how as the lattice deepens, the band spacings transition from irregular to equal (harmonic). (b) Detail of bands 1 and 2 at small lattice depth. The energy is now plotted relative to the ground band energy.

is present, the populations oscillate at the frequency $(E_{20} - E_{00})/h$. With higher orders, multiple oscillation frequencies result in complex diffraction patterns.

For lattice depths below 1 E_R, the diffracted populations are small, and the oscillation period saturates to $h/(4E_R)$ (see Fig. 5.2(b)). At 0.05 E_R, less than 0.008% of atoms are diffracted for a single lattice pulse. In order to increase the signal, we employ a multi-pulse diffraction sequence that coherently adds the effect of each pulse, similar to quantum resonances in delta-kicked rotors [117,118]. For weak lattices where only orders with $|l| \leq 1$ are populated, a Bloch sphere picture provides intuition [119] (Fig. 5.3). For initially stationary atoms, the $|l| = 1$ orders are equivalent and can be represented as a single state, which along with the $l = 0$ state are the two poles of the Bloch sphere. Free evolution corresponds to precession about the vertical axis with period $h/(4E_R)$, called the Talbot time [120]. During a weak lattice pulse, the precession axis is tilted by an angle proportional to the lattice depth with essentially the same $h/(4E_R)$ period; as described in Section 5.5, we account for the exact precession period numerically when determining the lattice depth. Alternating lattice and free evolution with duration $h/(8E_R)$ (one half precession period, $\simeq 9.75$ μs at 423 nm) efficiently increases the diffracted population (see

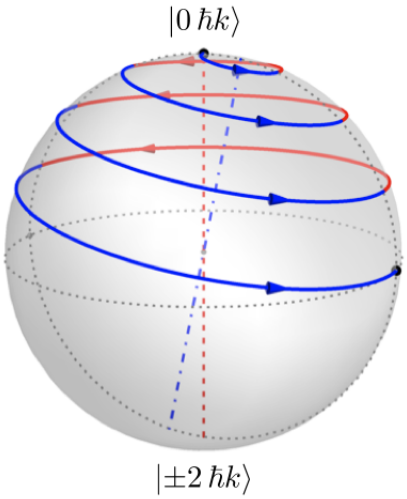

Figure 5.3: A Bloch sphere representation of the state vector's evolution during a pulse sequence. The state vector starts in $|0\hbar k\rangle$ (north pole). Lattice (free) evolution is shown in blue (red). Alternating lattice and free evolutions with duration $h/(8E_R)$, the diffracted population is maximized as described in the text. This sequence provides 50% population in $|\pm 2\hbar k\rangle$ after four pulses, corresponding to a lattice depth of $\simeq 1E_R$, much larger than depths we actually measured.

Fig. 5.3).

5.4 Measurement of the $6p$ light shift zeros of Rb

We extracted the transition matrix elements between the ground $5s_{1/2}$ and $6p_{1/2}$, $6p_{3/2}$ states in ^{87}Rb by measuring the light shift as a function of λ near the two λ_{zero} points neighboring the $6p$ states (see the inset in Fig. 5.4). We applied a sequence of standing wave (optical lattice) pulses to a Bose-Einstein condensate (BEC) containing $\simeq 3.5 \times 10^4$ $|F = 1, m_F = -1\rangle$ atoms with no discernible thermal fraction, produced in a hybrid optical and magnetic trap similar to [20]. At the end of the pulse sequence, we suddenly turn off the trap and measure the atom population in each diffracted order from an absorption image after 40 ms time of flight. By intentionally using a small condensate, we can neglect atom-atom interactions, and limit the optical depth so that all orders in the image are unsaturated. The measured population fractions, normalized to the total number in each image, are insensitive

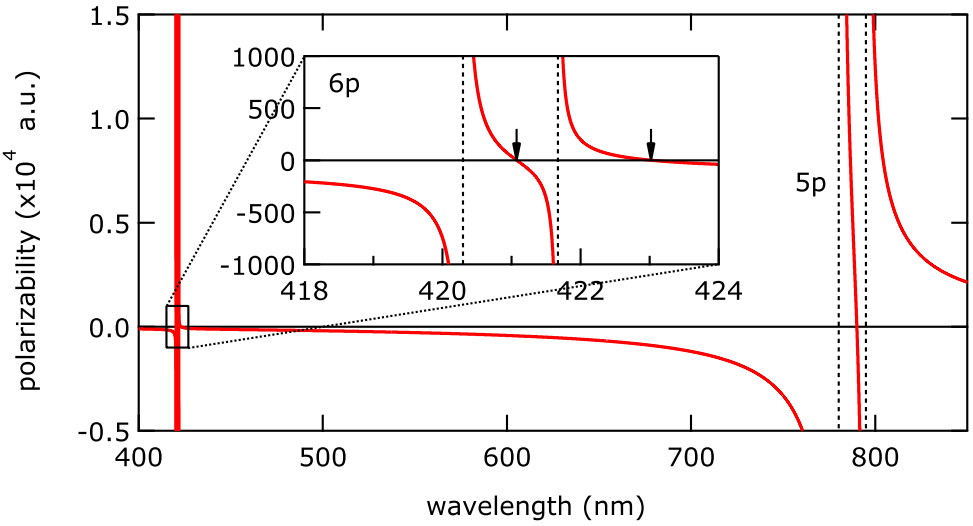

Figure 5.4: Calculated polarizability of Rb (atomic units of a_0^3). The vertical dashed lines are at the np-$5s$ transitions. Arrows indicate the positions of the relevant λ_{zero} points.

to small fluctuations in total atom number.

The lattice light is provided by a frequency-doubled diode laser, and is tunable between 419 nm and 424 nm. We measure the wavelength to 50 fm (90 MHz) accuracy with a wavemeter, calibrated to the known $5s$-$6p$ transition frequencies [121]. We form the lattice by reimaging a retroreflected beam on the atoms with an incident power of 60-120 mW and a waist of $\simeq 110$ μm. The lattice beam intensity varies only a few percent across the BEC, whose Thomas-Fermi radius is 18 μm transverse to the beam. Lattice alignment is performed at 421.700 nm where the light shift is reasonably large, $\simeq 7$ E_R. The input beam is carefully aligned to the BEC (with the retroreflected beam blocked) by minimizing the transverse displacement of the BEC induced by the beam. The retroreflected beam is then aligned by maximizing diffraction efficiency. Lattice depth measurements at the 5% uncertainty level are consistent with no drift during a data set, and the alignment is typically stable from day to day.

To minimize wavelength-dependent steering of the laser, we couple the light

through an optical fiber and focus the output of the fiber onto the BEC. We measured the residual steering after the fiber by monitoring the position of the beam 1 m downstream from the fiber tip. The observed deflection of the beam was < 30 μrad, which corresponds to at worst a 1% decrease in average beam intensity at the BEC and is included in our uncertainty analysis. Additionally, we monitor the power in each pulse sequence with a photodiode to account for different laser powers.

Lattice polarization also affects the measured light shift. Linearly polarized light has a nearly scalar light shift,[2] but elliptical polarization will have both vector and scalar light shifts for atoms with $|m_F| > 0$ [122], shifting the position of λ_{zero}. Although we used a Glan-laser polarizer to establish a clean linear polarization, analyzing the light after the chamber showed that the vacuum windows' slight birefringence created $\simeq 1\%$ ellipticity. To account for the possible systematic shift of λ_{zero}, we measured the light shift for two orthogonal, linear input polarizations, defined as S and P with respect to the plane of the last mirror before the chamber. By symmetry, the induced ellipticity from the window is opposite for the two input polarizations. We calculated that averaging the S and P measurements cancels the contribution of the vector light shift to a negligible 10 fm shift in λ_{zero}.

5.5 Analysis and results

To accurately determine the lattice depths from the measured populations, we numerically diagonalized the lattice Hamiltonian (see Appendix D, also [119]) in the plane wave basis including orders up to $|l| = 3$. From this we calculate the first-order diffracted population fraction P_1 as a function of pulse number n_p and lattice depth V_0 in units of E_R. In the weakly diffracting limit ($n_p V_0 \ll 4$), $P_1 \propto (n_p V_0)^2$, showing that multiple weak pulses are equivalent to one pulse n_p times stronger. Inverting

[2]The vector light shift is identically zero, while the tensor shift is less than 3×10^{-5} times the scalar shift over the range of our measurements. Additionally, the hyperpolarizability (proportional to intensity squared) is at the 10^{-7} level.

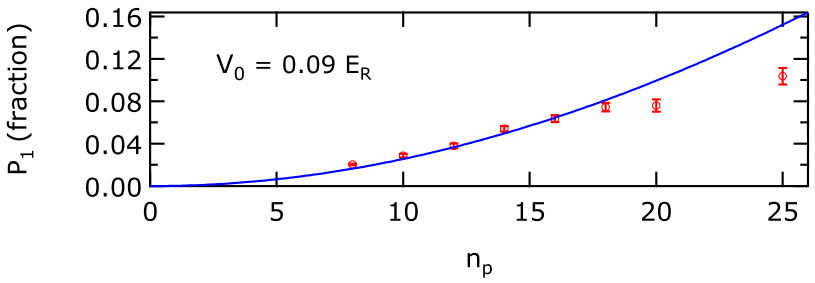

Figure 5.5: Diffracted population at fixed laser power and wavelength. As we vary the number of pulses, the diffracted population (our signal) initially increases as n_p^2. The solid line is is the theoretical calculation with V_0 as the only fit parameter, and error bars represent one standard error in the mean of 15 measurements. For accurate light shift measurements, we only used $n_p \leq 15$.

the numeric result for P_1, we extract the lattice depth $V_0(n_p, P_1)$ from the measured population fraction $P_1 = (N_{-1}+N_1)/(N_{-1}+N_0+N_1)$, with N_l the number of atoms in the lth order. Fig. 5.5 shows P_1 versus n_p at fixed V_0. The agreement with theory is excellent for n_p up to 18. We attribute deviations at larger n_p to the reduced overlap of the diffracted components, which travel a significant fraction of the size of the BEC, during the pulse sequence.

To determine the polarizability α, we extract the raw lattice depth $V_0(n_p, P_1)$ for each image, which is then divided by the measured photodiode power for that pulse sequence. Although this gives $|\alpha|$, theory is sufficiently accurate to unambiguously choose the sign. Fig. 5.6 shows the extracted polarizability as a function of λ for four data sets: two orthogonal polarizations, S and P, near each λ_{zero}. The lattice is aligned before each data set, and measurements after confirm consistent alignment within a data set. The measurement is repeated up to 20 times at each wavelength,[3] and the error bars in Fig. 5.6 represent purely statistical uncertainty of 1σ. For both sets around the 421 nm zero, we used 15 pulses, and for both sets around 423 nm we used 8 or 11 pulses.

[3]Some points exhibited decreased diffraction, correlated with the condensate position in each image, due to residual condensate motion. Thus we excluded the 22% of images where the condensate was more than 15 μm from the average position for each data set. The extracted matrix elements are insensitive to the exclusion value.

We fit the polarizability to the sum over states expression already presented in Eq. (4.2):

$$\alpha \propto \frac{1}{3}\sum_{n=5}^{8}\sum_{j=1/2}^{3/2}\frac{\left|d_{np_j}\right|^2\omega_{np_j}}{\omega^2-\omega_{np_j}^2}+C_{\text{tail}}+C_{\text{core}}\,, \tag{5.1}$$

where the $d_{np_j} \equiv \langle np_j||D||5s\rangle$ are reduced dipole matrix elements and ω is the lattice laser frequency. The matrix elements $d_{6p_{1/2}}$ and $d_{6p_{3/2}}$ are fit parameters, while $d_{5p_{1/2}}$ and $d_{5p_{3/2}}$ are fixed by the experimental lifetime measurement [123]. The $7p$ and $8p$ matrix elements and the contribution C_{core}, which includes the polarizability of the core electrons and their interaction with the valence electron, are calculated in [115]. We also included an improved calculation of C_{tail}, the valence contribution for $n > 8$, with reduced uncertainty, the result of which is published in the supplemental material to [93].

Fitting the data to Eq. 5.1 around a given λ_{zero} constrains the relationship among the parameters in the equation. For example, the position of the λ_{zero} near 421 nm, which is between the two $6p$ lines, depends strongly on the *ratio* of the $6p$ matrix elements, $R_{6p} = d_{6p_{3/2}}/d_{6p_{1/2}}$, but more weakly on their absolute value. On the other hand, the position of the λ_{zero} near 423 nm, which is red-detuned of both $6p$ lines, depends more on the average value of the $6p$ elements (in relation to the $5p$ elements). Fits around a single λ_{zero} constrain $6p$ elements with respect to the non-$6p$ parameters (d_{np}, C_{tail} and C_{core}), and the extracted values are sensitive to their uncertainties. Including data around multiple λ_{zero} points further constrains the fits. For our case, where the two λ_{zero}'s are close to each other, the effect of the non-$6p$ contributions is essentially identical for the two zeros, so that simultaneous fits to both zeros accurately determines R_{6p}, independent of the other parameters. With the addition of sufficiently accurate theoretical and experimental values for the other d_{np}, C_{tail} and C_{core}, we can also accurately determine absolute values for $d_{6p_{1/2}}$ and $d_{6p_{3/2}}$.

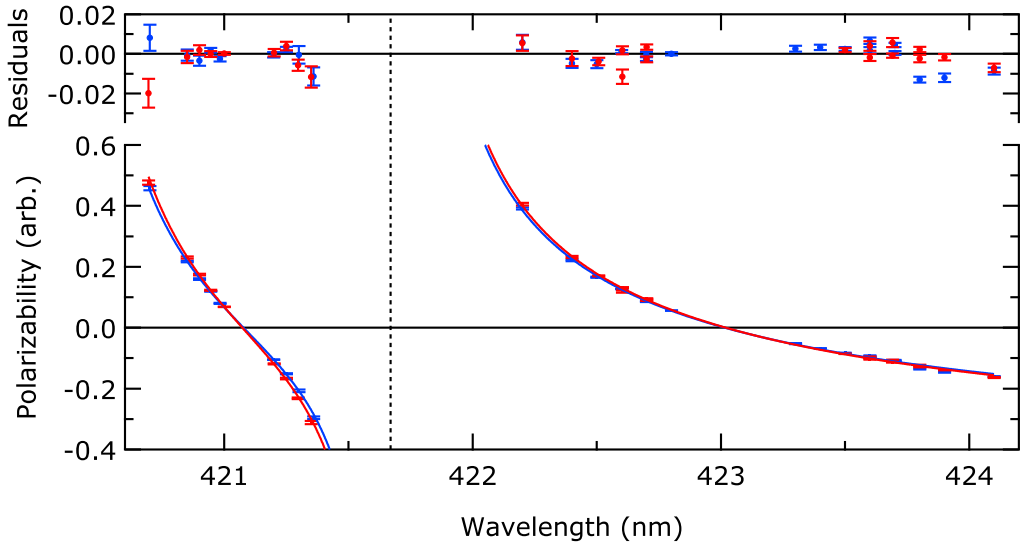

Figure 5.6: Measured polarizability (arb. units) versus wavelength for two linear, orthogonal input polarizations S (red) and P (blue). Each point is an average of up to 20 measurements, shown with 1σ statistical error bars (standard error of the mean). The solid lines (nearly indistinguishable) are fits to the expected form (Eq. 5.1) with the $6p$ matrix elements as free parameters; reduced χ^2 for the S and P fits is 4 and 11, respectively—see the text for a discussion of contributing systematics. Additionally, we allow a separate amplitude about each zero to account for different laser power. Fit residuals are shown at the top.

We simultaneously fit the 421 nm and 423 nm data sets for a given polarization. Due to possible differences in alignment and total power between sets, we fit with an independent amplitude, A_λ, around each λ_{zero} giving a total of four fit parameters: $A_{421}, A_{423}, d_{6p_{1/2}}, d_{6p_{3/2}}$. The fit values are then averaged for the two polarizations. (The small difference in extracted matrix elements for S and P polarization is consistent with the 1% ellipticity discussed earlier.) Table 5.1 summarizes the contributions to our final uncertainty in our measured values for R_{6p}, $d_{6p_{1/2}}$ and $d_{6p_{3/2}}$. The statistical uncertainty in R_{6p}, $d_{6p_{1/2}}$ and $d_{6p_{3/2}}$ are roughly the same, of order 0.1%. As expected, the contribution of the uncertainties of the other fixed parameters in Eq. 5.1 to R_{6p} is negligible, providing a good comparison with theory, which can predict ratios more accurately than matrix elements.The uncertainties in $d_{6p_{1/2}}$ and $d_{6p_{3/2}}$ do depend on the other parameters, and the two largest contributions are from the theoretical uncertainty in the $np_{3/2}$ component of C_{tail} and the experimental uncertainty in $d_{5p_{3/2}}$; these contribute at the 0.06% level.

To account for potential lattice alignment drift, we simulated the effect of a 5% linear drift in the extracted polarizability across a data set, which resulted in an additional 0.2% uncertainty in $d_{6p_{1/2}}$, and 0.1% in R_{6p} and $d_{6p_{3/2}}$. That reduced χ^2 for the fits in Fig. 5.6 is larger than 1 is accounted for by the additional uncertainty in alignment drift, which we expect also explains the disparity between S and P fits. Rescaling the statistical uncertainty to give reduced χ^2 of 1 produces similar total uncertainty.

Our light shift cancellation measurement technique accurately determines the ratio of the $6p$ matrix elements, with $R_{6p} = 1.617(2)$. The matrix elements are $d_{6p_{1/2}} = 0.3235(9)$ and $d_{6p_{3/2}} = 0.5230(8)$, in excellent agreement with the theoretical values (Table 5.1). From these we determine values for the λ_{zero} points: 421.075(2) nm and 423.018(7) nm.

Table 5.1: Absolute uncertainty contributions (in $ea_0 \times 10^{-4}$) for the $5s$-$6p$ matrix elements and their ratio ($\times 10^{-4}$). Note the insensitivity of R_{6p} to uncertainty in the fit parameters. Total uncertainty is summed in quadrature. Additionally, our $5s$-$6p$ matrix elements are compared to the theoretical values (in ea_0).

Contribution	$\delta d_{6p_{1/2}}$	$\delta d_{6p_{3/2}}$	δR_{6p}
statistical	1.79	1.90	11.1
$d_{5p_{1/2}}$	0.84	1.34	0.004
$d_{7p_{1/2}}$	0.08	0.13	0.012
$d_{8p_{1/2}}$	0.02	0.04	0.003
$np_{1/2}$ tail	0.56	0.92	0.029
$d_{5p_{3/2}}$	1.77	2.87	0.007
$d_{7p_{3/2}}$	0.22	0.36	0.031
$d_{8p_{3/2}}$	0.06	0.10	0.007
$np_{3/2}$ tail	2.01	3.28	0.104
core	1.25	2.05	0.064
alignment drift	7.82	6.18	19.9
Total	8.62	8.24	22.8
theoretical value [115]	0.325(9)	0.528(13)	1.624(7)
our results	0.3235(9)	0.5230(8)	1.617(2)

5.6 Conclusion

We have presented the first experimental measurement of the 5s-6p dipole transition matrix elements in Rb. Our technique of measuring the relative light shift near λ_{zero} is applicable to many important atoms. At a minimum, such measurements constrain matrix elements and provide benchmarks needed for atomic theory. Additionally, applying our measurement technique to metastable states, such as the $^3P_0$ clock state of Yb or Sr, could provide information about excited-excited state matrix elements.

Appendix A: Mechanical drawings

This appendix contains mechanical drawings for components of the apparatus described in Chapter 3. Figures start on the next page, and all dimensions are in inches unless otherwise noted.

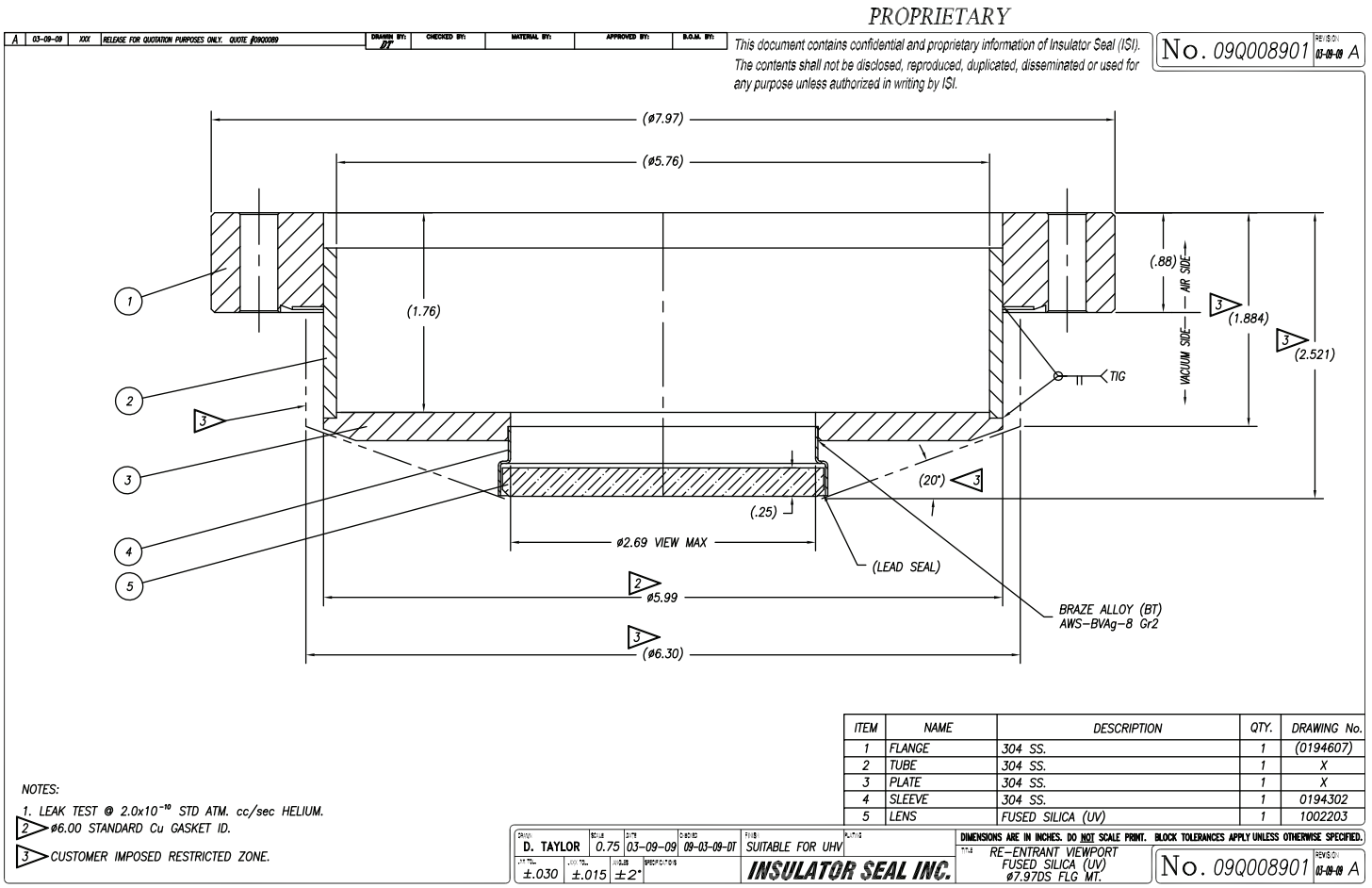

Figure A.1: Manufacturer's drawing for the recessed "bucket" windows. While a standard 8" copper gasket does fit per note 2, the clearance is so tight it would be easier to use a larger ID gasket, such as those sold by Kimball Physics. The lead glass-to-metal seal limits bakeout temperature to 150 °C. Written permission was obtained to include the drawing in this dissertation.

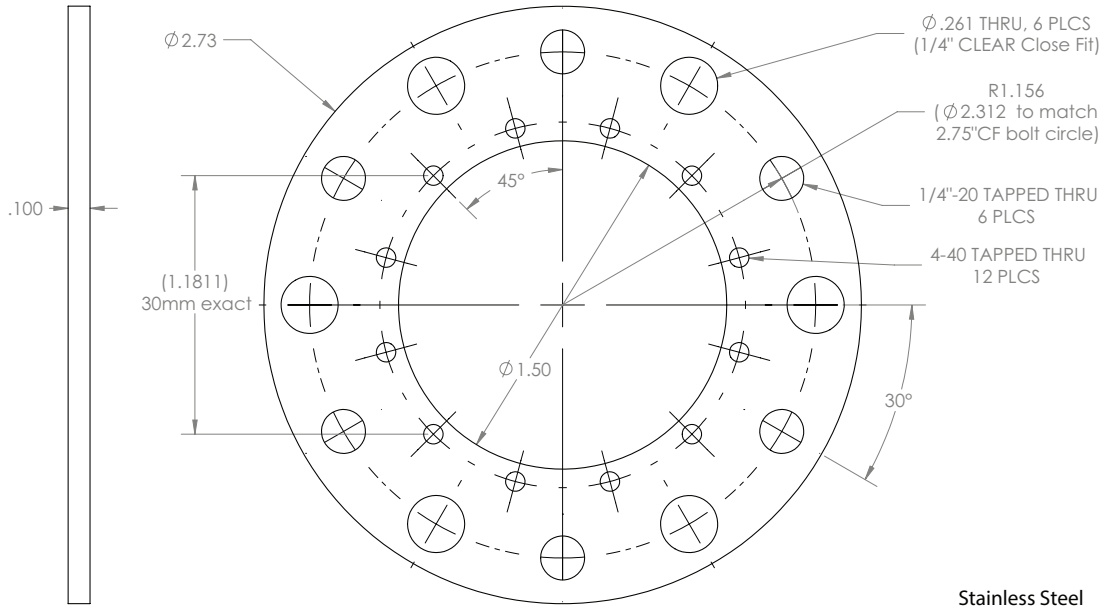

Figure A.2: 2.75" CF vacuum viewport "cage washers" to adapt to 30 mm cage system.

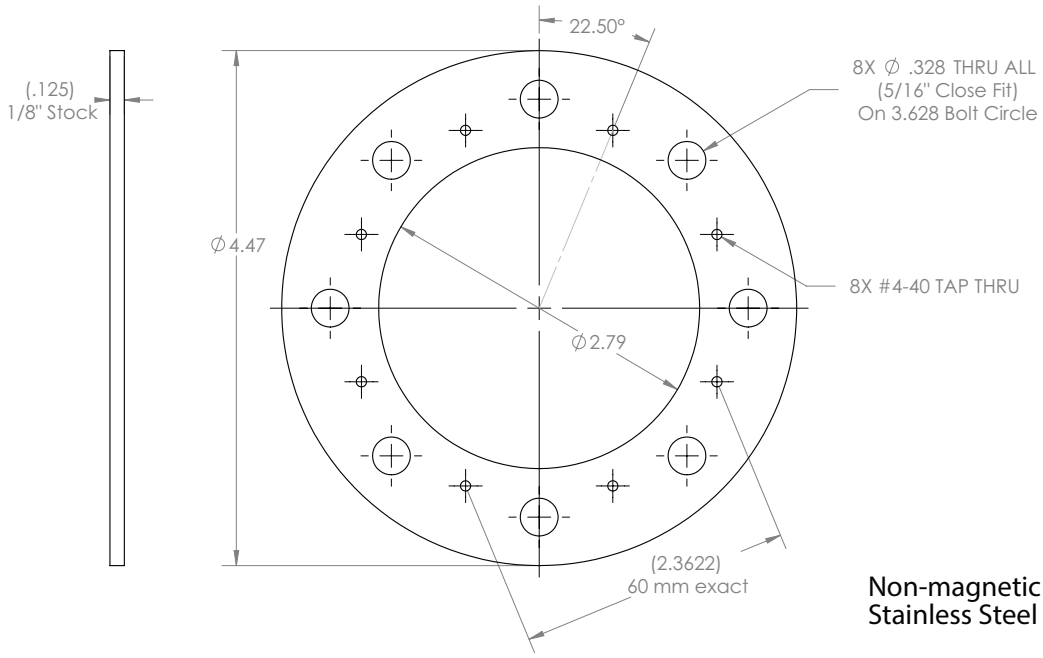

Figure A.3: 4.5" CF vacuum viewport "cage washers" to adapt to 60 mm cage system.

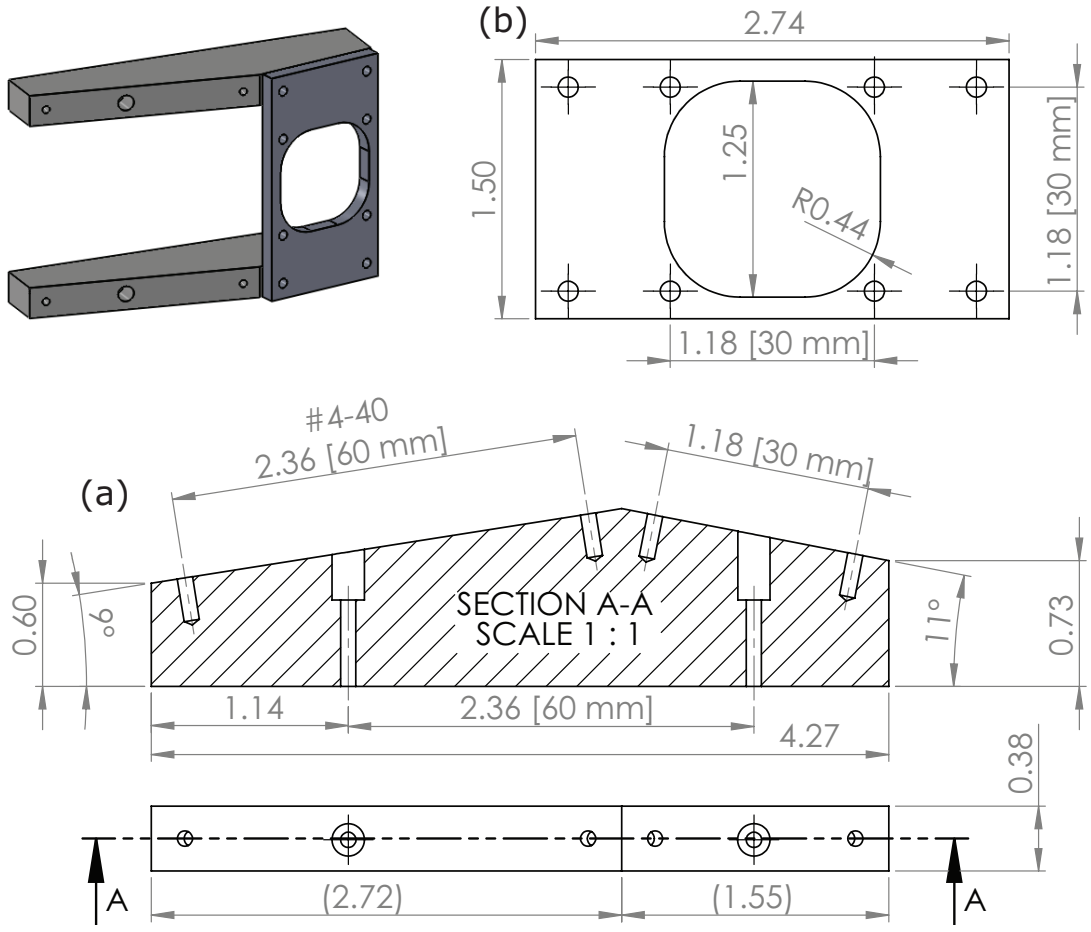

Figure A.4: Two of these angle plates (a) are attached to the 4.5" cage washers on each viewport around the chamber. To assist in sending multiple beams through each viewport, the adapters allow mounting with 60 mm cage system (MOT beams) alongside 30 mm cage (423 lattice), with the use of an additional plate (b).

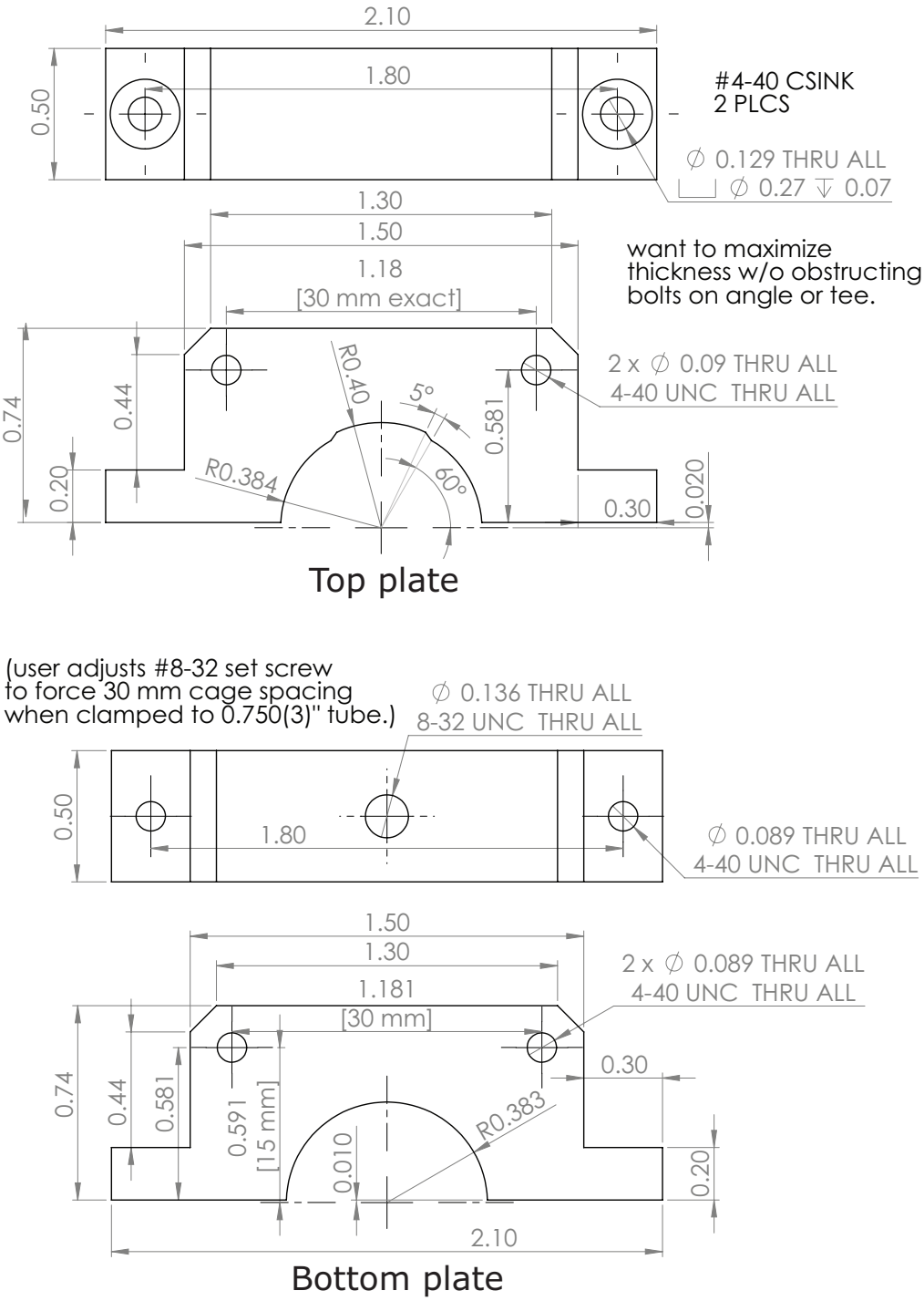

Figure A.5: Adapter for 0.75" tube (mini-CF) to 30 mm cage system. The separation between top and bottom clamp plates is intended to be defined by the set screw on the bottom plate. One should temporarily use a cage plate as close to the clamp to define the cage rod spacing when the clamp is installed. The clamp is shown attached to the chamber in the bottom left of Fig. 3.3.

Appendix B: Calculating Atomic Polarizability

Here we briefly describe calculating ac scalar polarizabilities (see also Section 3.5.3). When calculated from first principles [92], the polarizability is the sum of valance and core contributions [115]:

$$\alpha_0(\omega) = \alpha_0^v(\omega) + \alpha_{core} + \alpha_{vc}\,. \tag{B.1}$$

Since core electronic excitations are typically at much higher energies than available lasers, they are well approximated as frequency independent. Often, simply calculating the valence contribution $\alpha_0^v(\omega)$ is sufficient for dipole trap estimates. This is most conveniently computed as a sum over states (in atomic units):

$$\alpha_0^v(\omega) = \frac{2}{3(2J_v+1)} \sum_k \frac{\langle k \parallel D \parallel v \rangle^2 (E_k - E_v)}{(E_k - E_v)^2 - \omega^2} \tag{B.2}$$

Atomic transition energies are known to much higher precision than matrix elements and effectively have no uncertainty for our purpose. The atomic unit of energy is the hartree, however, spectroscopists often work in wave numbers, where $1E_h = 219\,474.631\ \mathrm{cm}^{-1}$. The NIST Atomic Spectra Database[1] (ASD) is a convenient source for both atomic energies and matrix elements. The database contains neutral and ionic data, so to restrict to neutral Yb lines one should search for "Yb I." Matrix elements are often expressed as line strengths S_{vk}, which are simply matrix

[1] http://physics.nist.gov/PhysRefData/ASD/lines_form.html

	$\alpha_{\mathrm{Yb}}(\omega = 0)$	$\alpha_{\mathrm{Yb}}(\lambda = 759.4\ \mathrm{nm})$
experiment	139(10) [94]	
theory	141(2) [125]	188
our calculation	141(6)	191(8)

Table B.1: There is close agreement between our polarizability calculation for Yb and known values. The ground state polarizability at the clock wavelength is from a private communication with Marianna Safronova.

Table B.2: Contributions to the frequency-dependent polarizability of the ground state of Yb at 532 and 1064 nm. Absolute values of electric-dipole matrix elements are expressed in a.u. (ea_0), and the corresponding energy differences are expressed in conventional wavenumber units (cm^{-1}). The matrix elements are from [124].

Contribution	$\lvert\langle k\lvert\lvert D\rvert\rvert 6s^2\rangle\rvert$	$E_k - E_{6s^2}$	α_{532}	α_{1064}
$6s6p\ ^3P_1$	0.5394(6)	17992.007	−25.86(5)	3.254(7)
$6s6p\ ^1P_1$	4.242(44)	25068.222	239.9(5.0)	122.2(2.6)
$4f^{13}5d6s^2\ J' = 1$	2.052(125)	28857.014	37.1(4.5)	23.9(2.9)
$4f^{13}6s^2?\ J' = 1$	0.636(82)	37414.59	2.12(55)	1.69(43)
$6s7p\ ^1P_1$	1.491(91)	40563.97	10.2(1.2)	8.5(1.0)
$6s8p\ ^3P_1$	0.279(17)	43659.38	0.32(4)	0.27(3)
$6s8p\ ^1P_1$	0.756(46)	44017.60	2.33(28)	1.99(24)
$6s9p\ ^3P_1$	0.300(18)	46078.91	0.34(4)	0.30(4)
$6s9p\ ^1P_1$	0.360(22)	46370.30	0.49(6)	0.43(5)
Total α			266.9(11.8)	162.5(7.3)

elements squared, or oscillator strengths f_{vk}, which are related by

$$\frac{\lambda_{vk}[\mathrm{nm}](2J_v + 1)}{30.3756} f_{vk} = S_{vk}[\mathrm{a.u.}] = \lvert\langle k\lvert\lvert D\rvert\rvert v\rangle\rvert^2, \tag{B.3}$$

where v is the lower state, and λ_{vk} is the transition wavelength in nm.

For Yb, we got closer agreement to the known static polarizability ($\omega = 0$) and ground state polarizability at the clock magic wavelength $\lambda = 759.4$ nm (see Table B.1) by using the data tabulated by Morton [124] instead of the ASD. The contribution from individual states to the dipole wavelength polarizabilities is summarized in Table B.2. The matrix elements and core contributions used for Rb are identical to the supplemental material in [93]. In Table B.3, the contributions to the total polarizability at each dipole trap wavelength are tabulated.

Table B.3: Contributions to the frequency-dependent polarizability of the ground state of Rb at 532 and 1064 nm. Absolute values of electric-dipole matrix elements are expressed in a.u. (ea_0), and the corresponding energy differences are expressed in conventional wavenumber units (cm^{-1}). The "tail" contribution from higher p states is also included and approximated as wavelength-independent.

Contribution	$\lvert\langle np_j\rvert\rvert D\rvert\rvert 5s\rangle\rvert$	$E_{np_j} - E_{5s}$	α_{532}	α_{1064}
$5p_{1/2}$	4.231(3)	12578.95	−84.44(12)	235.68(35)
$6p_{1/2}$	0.3235(9)	23715.08	0.868(5)	0.383(2)
$7p_{1/2}$	0.115(3)	27835.02	0.063(3)	0.039(2)
$8p_{1/2}$	0.060(2)	29835.00	0.014(1)	0.010(1)
$(n > 8)p_{1/2}$ tail			0.053(41)	0.053(41)
$5p_{3/2}$	5.978(5)	12816.55	−177.23(12)	441.29(35)
$6p_{3/2}$	0.5230(8)	23792.59	2.238(5)	0.997(2)
$7p_{3/2}$	0.202(4)	27870.11	0.197(8)	0.121(3)
$8p_{3/2}$	0.111(3)	29853.80	0.050(2)	0.034(2)
$(n > 8)p_{3/2}$ tail			0.195(145)	0.195(145)
Core			8.709(93)	8.709(93)
Total α			−249.28(70)	687.51(1.21)

Appendix C: Trap frequencies for crossed dipole traps

For a single beam dipole trap, it is easy to calculate the trap frequencies analytically. Our crossed-dipole trap is non-orthogonal and non-symmetric in the sense that as we adjust the relative powers between the horizontal and crossing beams, the principal trap axes rotate. The following excerpt of Mathematica code determines the principal axes and trap frequencies of the approximate ellipse (harmonic trap) for the trap minimum near `rmGuess` of the potential `Utot`, the sum of all dipole, magnetic, and gravitational potentials. The Hessian matrix or gradient of the Jacobian, is computed in the given coordinate system for the Taylor expansion of `Utot`. The eigenvectors of the Hessian are the trap axes, and the eigenvalues are proportional to the squared trap frequencies. All positions are in μm and `Utot` gives units of `units`, which converts from J to μK or kHz.

```
trapFreqs[rmGuess_] := Module[
  {e0, rm, r0, r, x, y, z, t, approxEll, freqs, axes},
  r = {x, y, z};
  {e0, rm} =
    FindMinimum[Utot[{x, y, z}], {x, rmGuess[[1]]},
      {y, rmGuess[[2]]}, {z, rmGuess[[3]]}];
  r0 = r /. rm;
  approxEll = Normal[
    Series[Utot[(r - r0) t + r0] 10^12/(mass units),{t, 0, 2}]
  ] /. t -> 1;(* to 2nd order in all variable combinations *)
  {freqs, axes} =
    Eigensystem[Grad[Grad[approxEll, {x, y, z}], {x, y, z}]];
    (* evals of this matrix are square trap frequencies *)
  freqs = Sqrt[freqs]/(2 \[Pi]);
  {freqs, {e0, r0}, axes}]
```

Note that `Utot`, `units`, and `mass` (in kg) are not defined here.

Appendix D: Calculating lattice diffraction

D.1 Lattice Hamiltonian

The Hamiltonian for an atom in a 1D optical lattice is

$$\hat{H}_{\text{lat}} = \frac{\hat{p}^2}{2M} + V_0 \sin^2 kx = \frac{\hat{p}^2}{2M} + \frac{V_0}{2} - \frac{V_0}{4}\cos 2kx \tag{D.1}$$

The eigenfunctions of this periodic Hamiltonian are Bloch functions

$$\hat{H}_{\text{lat}}\phi_{nq}(x) = E_{nq}\phi_{nq}(x) \tag{D.2}$$

with quasimomentum q and band label n. The Schrödinger equation for the Bloch functions is just the Mathieu equation [126]

$$\phi'' + [a + 2s\cos 2z]\,\phi = 0 \tag{D.3}$$

with $z = kx$, $s = V_0/(4E_R)$, and $a = (2E_{nq} - V_0)/(2E_R)$, where

$$E_R = \frac{\hbar^2 k^2}{2M} = \frac{h^2}{2M\lambda^2} \tag{D.4}$$

is the recoil energy of a lattice laser photon. Solutions of Eq. (D.3) are only periodic in z for particular values of a called Mathieu characteristics, which in turn determine allowed band energies E_{nq}.

An alternate approach approach to solving Eq. (D.2), is to expand the Bloch

functions in the plane wave basis

$$\phi_{nq}(x) = \sum_m c_{nq}^{(m)} \exp^{iqx} \exp^{i2mkx} \tag{D.5}$$

for integer m. And writing Eq. (D.1) in plane waves, it is clear that the lattice will only couple plane waves with momentum differing by $2k$. This leads to a matrix form of the Hamiltonian

$$H_{\text{lat}} = \begin{pmatrix} \ddots & -\frac{V_0}{4} & 0 & 0 & 0 \\ -\frac{V_0}{4} & \frac{\hbar^2(q+2k)^2}{2M} + \frac{V_0}{2} & -\frac{V_0}{4} & 0 & 0 \\ 0 & -\frac{V_0}{4} & \frac{\hbar^2 q^2}{2M} + \frac{V_0}{2} & -\frac{V_0}{4} & 0 \\ 0 & 0 & -\frac{V_0}{4} & \frac{\hbar^2(q+2k)^2}{2M} + \frac{V_0}{2} & -\frac{V_0}{4} \\ 0 & 0 & 0 & -\frac{V_0}{4} & \ddots \end{pmatrix} \tag{D.6}$$

In practice, one only includes plane waves up to some maximum m set by the lattice depth. Found by numeric diagonalization for a given V_0 as a function of q, the eigenvalues are band energies and their corresponding eigenvectors are the coefficients to the plane wave expansion Eq. (D.5).

To simulate the diffracted populations from a lattice pulse, one simply makes the sudden approximation. The initial state, a plane wave with zero momentum for a BEC, is projected into the Bloch basis (with with even n and $q = 0$). During the lattice pulse, each component is time-evolved based on its band energy, found by diagonalizing Eq. (D.6). Between lattice pulses in a sequence, each plane wave accumulated phase based on its momentum. The populations are found by squaring the plane wave amplitudes at the end of a pulse sequence. A minimal version of this procedure implemented in Mathematica is included in Section D.2.

D.2 Mathematica code for diffracted populations

We define the Hamiltonian (Eq. (D.6)) in recoil units for an atom in a sinusoidal potential do depth V (in E_R, defined in Eq. (D.4)) with momentum in units of k of the lattice laser:

```
NBase = 5; (* num plane waves (must be odd!) *)
Hamilt[q_, V_] = SparseArray[{
    {i_, i_} -> (q + 2 (i - (NBase + 1)/2))^2 + 0.5 V,
    {i_, j_} /; Abs[i - j] == 1 -> -0.25 V
   }, {NBase, NBase}];
```

Momenta up to $\pm 2l\hbar k$ are included where the maximum l is given by `(NBase-1)/2`. The `MatrixForm` of the Hamiltonian can be displayed using

```
Hamilt[q, V]//MatrixForm
```

We solve for the eigenvectors and eigenenergies (`NBase` of them) using `Eignesystem[]`. Provided the argument is numeric, Mathematica sorts the eigenvalues in *decreasing order* and the corresponding eigenvectors are normalized. Energy bands are labeled with starting with $n = 0$.

To save on computation, the diagonalization is only performed once and the result, `Esystem` is passed to the other functions. Additionally, we take advantage of fast matrix multiplication rather than writing sums explicitly. It's important that these functions are `:=` defined, otherwise Mathematica will take a long time solving for arbitrary q.

```
nBands = NBase; (* Number of bands to calculate; reduce if slow *)
kmax = (NBase - 1)/2;

Esystem[q_, V_] :=
 Eigensystem[Hamilt[q, V], -nBands];(* nBands lowest *)
En[n_, Esystem_] := Esystem[[1, -(n + 1)]];(* Band Energy *)
State[n_, Esystem_] :=
 Esystem[[2, -(n + 1)]];(* vector of plane wave coefs *)
Bloch[n_, q_, Esystem_] :=
 Exp[I q x] State[n, Esystem].Exp[I 2 Range[-kmax, kmax] x];
```

Time evolution matrices `LatEvoMat[]` and `FreeEvoMat[]` (both in the plane wave basis) give phase factors appropriate for time evolution of plane wave states with and without lattice light, respectively. The time evolved state is computed with the matrix multiplication `EvoMat.state`, and time is in units of recoil time $t_R = h/E_R$.

```
FreeEvoMat[q_, t_] :=
 DiagonalMatrix[Exp[-I 2 Pi (q + 2 Range[-kmax, kmax])^2 t]];

LatEvoMat[t_, Esystem_] :=
 Transpose[Esystem[[2]]].DiagonalMatrix[Exp[-I 2 Pi Esystem[[1]] t]].
   Conjugate[Esystem[[2]]];
```

The following function gives the population in each diffracted order $(0, +2, +4, \ldots)\hbar k$ for a series of `Np` pulses of lattice depth `V` with duration `tL`. The negative momentum orders are equal to the positive momentum because we assume the atoms start in $q = 0$. For maximum efficacy with a weak lattice, the delay time for free evolution between pulses is `TT/2` where the Talbot time `TT` $= 1/(4E_R) = 0.25t_R$.

```
popout[V_, tL_, Np_] := Module[
  {LatticeMat, PulseMat, esys, TT = .25, qin = 0, k0},
  k0 = Table[Switch[i, 0, 1, _, 0], {i, -kmax, kmax}];
  esys = Esystem[qin, V];
  LatticeMat = N[Chop[LatEvoMat[tL, esys]]];
  PulseMat = N[Chop[LatticeMat.FreeEvoMat[qin, TT/2]]];
  Part[
   Abs[MatrixPower[PulseMat, Np - 1].LatticeMat.k0]^2
   , kmax + 1 ;; kmax + Min[5, kmax + 1]](*result is symmetric list,
  only spit out the first five order's population*)
 ];
```

It is important to only ask Mathematica to evaluate numeric values of `tL`, or it will take a very long time to run (grows quickly with `Np`). This can be done in a continuous way with `Plot[Evaluate[<popout>],<trange>]`, where `Evaluate[]` forces specific t-values in `<trange>`, automatically determined by `Plot[]`. For more control one can also use the discrete method like `List(Line)Plot[Table[<popout>,<tlist>]]`

where optionally using `ListLinePlot[]` makes a connected trace like `Plot[]`. Evaluation becomes slow with too many plane waves, so one should use just enough so that the population in the highest order is negligible. For moderate to weak lattices, `NBase` $= 5 - 7$ should be plenty.

As an example, consider a lattice of depth $V = 2E_R$ with 10 pulse sequence with lattice pulse duration also equal to half a Talbot time (or $0.125t_R$). The output is population in $(0, 2, 4)\hbar k$:

```
Np = 10; popout[2, .125, Np]
```

One can also generate plots where one parameter is varied. Here, we demonstrate the expected populations from a 10 pulse sequence with lattice pulse time of $0.125t_R$ for lattice depths on $[0, 5]$:

```
Vmin = 0; Vmax = 5;
ListLinePlot[
 Transpose[Table[popout[V, 0.125, Np], {V, Vmin, Vmax, .01}]],
 DataRange -> {Vmin, Vmax},
 AxesLabel -> {"Pop. Frac.", "Lattice Depth [ER]"},
 PlotLabel -> ToString[Np] <> "pulses"
]
```

For our experiment, it was important to also simulate slight changes in lattice pulse duration as we kept the absolute pulse length fixed while varying the lattice wavelength (which changes t_R).

Bibliography

[1] M. H. Anderson, J. R. Ensher, M. R. Matthews, C. E. Wieman, and E. A. Cornell, "Observation of Bose-Einstein condensation in a dilute atomic vapor." *Science*, vol. 269, no. 5221, p. 198, Jul. 1995. [Online]. Available: http://www.ncbi.nlm.nih.gov/pubmed/17789847 1

[2] K. Davis, M. Mewes, M. Andrews, N. van Druten, D. Durfee, D. Kurn, and W. Ketterle, "Bose-Einstein condensation in a gas of sodium atoms," *Physical Review Letters*, vol. 75, no. 22, p. 3969, Nov. 1995. [Online]. Available: http://link.aps.org/doi/10.1103/PhysRevLett.75.3969 1

[3] A. Daley, P. Fedichev, and P. Zoller, "Single-atom cooling by superfluid immersion: A nondestructive method for qubits," *Physical Review A*, vol. 69, no. 2, p. 022306, Feb. 2004. [Online]. Available: http://link.aps.org/doi/10.1103/PhysRevA.69.022306 2

[4] A. Griessner, A. Daley, S. Clark, D. Jaksch, and P. Zoller, "Dark-state cooling of atoms by superfluid immersion," *Physical Review Letters*, vol. 97, no. 22, p. 220403, Nov. 2006. [Online]. Available: http://link.aps.org/doi/10.1103/PhysRevLett.97.220403 2, 3

[5] A. Griessner, A. J. Daley, S. R. Clark, D. Jaksch, and P. Zoller, "Dissipative dynamics of atomic Hubbard models coupled to a phonon bath: dark state cooling of atoms within a Bloch band of an optical lattice," *New Journal of Physics*, vol. 9, no. 2, p. 44, Feb. 2007. [Online]. Available: http://stacks.iop.org/1367-2630/9/i=2/a=044 2

[6] B. Kraus, H. Büchler, S. Diehl, A. Kantian, A. Micheli, and P. Zoller, "Preparation of entangled states by quantum Markov processes," *Physical Review A*, vol. 78, no. 4, p. 042307, Oct. 2008. [Online]. Available: http://link.aps.org/doi/10.1103/PhysRevA.78.042307 2

[7] S. Diehl, A. Micheli, A. Kantian, B. Kraus, H. P. Büchler, and P. Zoller, "Quantum states and phases in driven open quantum systems with cold

atoms," *Nature Physics*, vol. 4, no. 11, p. 878, Sep. 2008. [Online]. Available: http://www.nature.com/doifinder/10.1038/nphys1073 2

[8] S. Diehl, E. Rico, M. A. Baranov, and P. Zoller, "Topology by dissipation in atomic quantum wires," *Nature Physics*, vol. 7, no. 12, p. 971, Oct. 2011. [Online]. Available: http://www.nature.com/doifinder/10.1038/nphys2106 2

[9] C. A. Muschik, H. Krauter, K. Jensen, J. M. Petersen, J. I. Cirac, and E. S. Polzik, "Robust entanglement generation by reservoir engineering," *Journal of Physics B: Atomic, Molecular and Optical Physics*, vol. 45, no. 12, p. 124021, Jun. 2012. [Online]. Available: http://stacks.iop.org/0953-4075/45/i=12/a=124021 2

[10] Y.-J. Lin, K. Jiménez-García, and I. B. Spielman, "Spin-orbit-coupled Bose-Einstein condensates." *Nature*, vol. 471, no. 7336, p. 83, Mar. 2011. [Online]. Available: http://dx.doi.org/10.1038/nature09887 2

[11] T. Ramos, H. Pichler, A. J. Daley, and P. Zoller, "Engineering a chiral system-reservoir interaction with a 1D spin-orbit-coupled Bose-Einstein quasi-condensate," 2013, private communication. 2

[12] N. Bogoliubov, "On the theory of superfluidity," *Journal of Physics*, vol. 11, no. 1, p. 23, 1947. 2

[13] M. Bruderer, A. Klein, S. Clark, and D. Jaksch, "Polaron physics in optical lattices," *Physical Review A*, vol. 76, no. 1, p. 011605, Jul. 2007. [Online]. Available: http://link.aps.org/doi/10.1103/PhysRevA.76.011605 4

[14] A. Klein, M. Bruderer, S. R. Clark, and D. Jaksch, "Dynamics, dephasing and clustering of impurity atoms in Bose-Einstein condensates," *New Journal of Physics*, vol. 9, no. 11, p. 411, Nov. 2007. [Online]. Available: http://stacks.iop.org/1367-2630/9/i=11/a=411 4

[15] M. Bruderer, A. Klein, S. R. Clark, and D. Jaksch, "Transport of strong-coupling polarons in optical lattices," *New Journal of Physics*, vol. 10, no. 3, p. 033015, Mar. 2008. [Online]. Available: http://stacks.iop.org/1367-2630/10/i=3/a=033015 4

[16] E. Meyer and J. Bohn, "Electron electric-dipole-moment searches based on alkali-metal- or alkaline-earth-metal-bearing molecules," *Physical Review A*, vol. 80, no. 4, p. 042508, Oct. 2009. [Online]. Available: http://link.aps.org/doi/10.1103/PhysRevA.80.042508 6

[17] L. K. Sørensen, S. Knecht, T. Fleig, and C. M. Marian, "Four-component relativistic coupled cluster and configuration interaction calculations on the ground and excited states of the RbYb molecule," *The Journal of Physical Chemistry A*, vol. 113, no. 45, p. 12607, Nov. 2009. [Online]. Available: http://dx.doi.org/10.1021/jp904914m 6

[18] K. Aikawa, A. Frisch, M. Mark, S. Baier, R. Grimm, and F. Ferlaino, "Reaching fermi degeneracy via universal dipolar scattering," *Physical Review Letters*, vol. 112, no. 1, p. 010404, Jan. 2014. [Online]. Available: http://link.aps.org/doi/10.1103/PhysRevLett.112.010404 6

[19] P. S. Julienne, "Molecular states near a collision threshold," in *Cold Molecules: Theory, Experiment, Applications*, W. C. Stwalley, R. V. Krems, and B. Friedrich, Eds. Taylor and Francis, Feb. 2009, ch. 6. [Online]. Available: http://arxiv.org/abs/0902.1727 6

[20] Y.-J. Lin, A. Perry, R. Compton, I. Spielman, and J. Porto, "Rapid production of ^{87}Rb Bose-Einstein condensates in a combined magnetic and optical potential," *Physical Review A*, vol. 79, no. 6, p. 063631, Jun. 2009. [Online]. Available: http://link.aps.org/doi/10.1103/PhysRevA.79.063631 7, 12, 34, 111

[21] C. Myatt, E. Burt, R. Ghrist, E. Cornell, and C. Wieman, "Production of two overlapping Bose-Einstein condensates by sympathetic cooling," *Physical Review Letters*, vol. 78, no. 4, p. 586, Jan. 1997. [Online]. Available: http://link.aps.org/doi/10.1103/PhysRevLett.78.586 8

[22] A. Recati, P. O. Fedichev, W. Zwerger, J. von Delft, and P. Zoller, "Atomic quantum dots coupled to a reservoir of a superfluid Bose-Einstein condensate," *Physical Review Letters*, vol. 94, no. 4, p. 040404, Feb. 2005. [Online]. Available: http://link.aps.org/doi/10.1103/PhysRevLett.94.040404 8

[23] A. Griessner, A. Daley, D. Jaksch, and P. Zoller, "Fault-tolerant dissipative preparation of atomic quantum registers with fermions," *Physical Review A*, vol. 72, no. 3, p. 32332, Sep. 2005. [Online]. Available: http://link.aps.org/doi/10.1103/PhysRevA.72.032332 8

[24] L. LeBlanc and J. Thywissen, "Species-specific optical lattices," *Physical Review A*, vol. 75, no. 5, p. 053612, May 2007. [Online]. Available: http://link.aps.org/doi/10.1103/PhysRevA.75.053612 8, 108

[25] S. Tassy, N. Nemitz, F. Baumer, C. Höhl, A. Batär, and A. Görlitz, "Sympathetic cooling in a mixture of diamagnetic and paramagnetic atoms," *Journal of Physics B: Atomic, Molecular and Optical Physics*, vol. 43, no. 20, p. 205309, Oct. 2010. [Online]. Available: http://stacks.iop.org/0953-4075/43/i=20/a=205309 8

[26] M. Kitagawa, K. Enomoto, K. Kasa, Y. Takahashi, R. Ciuryło, P. Naidon, and P. Julienne, "Two-color photoassociation spectroscopy of ytterbium atoms and the precise determinations of s-wave scattering lengths," *Physical Review A*, vol. 77, no. 1, p. 012719, Jan. 2008. [Online]. Available: http://link.aps.org/doi/10.1103/PhysRevA.77.012719 10, 11, 14

[27] M. Borkowski, P. S. Żuchowski, R. Ciuryło, P. S. Julienne, D. Kędziera, Ł. Mentel, P. Tecmer, F. Münchow, C. Bruni, and A. Görlitz, "Scattering lengths in isotopologues of the RbYb system," *Physical Review A*, vol. 88, no. 5, p. 052708, Nov. 2013. [Online]. Available: http://link.aps.org/doi/10.1103/PhysRevA.88.052708 10, 11

[28] D. A. Brue and J. M. Hutson, "Prospects of forming ultracold molecules in $^2\Sigma$ states by magnetoassociation of alkali-metal atoms with Yb," *Physical Review A*, vol. 87, no. 5, p. 052709, May 2013. [Online]. Available: http://link.aps.org/doi/10.1103/PhysRevA.87.052709 10, 11

[29] N. Nemitz, F. Baumer, F. Münchow, S. Tassy, and A. Görlitz, "Production of heteronuclear molecules in an electronically excited state by photoassociation in a mixture of ultracold Yb and Rb," *Physical Review A*, vol. 79, no. 6, p. 061403, Jun. 2009. [Online]. Available: http://link.aps.org/doi/10.1103/PhysRevA.79.061403 10, 18, 19, 79

[30] F. Baumer, F. Münchow, A. Görlitz, S. E. Maxwell, P. S. Julienne, and E. Tiesinga, "Spatial separation in a thermal mixture of ultracold ^{174}Yb and ^{87}Rb atoms," *Physical Review A*, vol. 83, no. 4, p. 040702, Apr. 2011. [Online]. Available: http://link.aps.org/doi/10.1103/PhysRevA.83.040702 10

[31] E. G. M. van Kempen, S. J. J. M. F. Kokkelmans, D. J. Heinzen, and B. J. Verhaar, "Interisotope determination of ultracold rubidium interactions from three high-precision experiments," *Physical Review Letters*, vol. 88, no. 9, p. 093201, Feb. 2002. [Online]. Available: http://link.aps.org/doi/10.1103/PhysRevLett.88.093201 11

[32] J. Burke and J. Bohn, "Ultracold scattering properties of the short-lived Rb isotopes," *Physical Review A*, vol. 59, no. 2, p. 1303, Feb. 1999. [Online]. Available: http://link.aps.org/doi/10.1103/PhysRevA.59.1303 11

[33] H. J. Metcalf and P. van der Straten, *Laser Cooling and Trapping*. New York, NY: Springer-Verlag, 1999. 12, 40

[34] C. J. Pethick and H. Smith, *Bose-Einstein Condensation in Dilute Gases*. New York, NY: Cambridge University Press, Jun. 2002. [Online]. Available: http://scitation.aip.org/content/aip/magazine/physicstoday/article/56/6/10.1063/1.1595060 12

[35] S. L. Cornish, N. R. Claussen, J. L. Roberts, E. A. Cornell, and C. E. Wieman, "Stable ^{85}Rb Bose-Einstein condensates with widely tunable interactions," *Physical Review Letters*, vol. 85, no. 9, p. 1795, Aug. 2000. [Online]. Available: http://link.aps.org/doi/10.1103/PhysRevLett.85.1795 12

[36] A. L. Marchant, S. Händel, S. A. Hopkins, T. P. Wiles, and S. L. Cornish, "Bose-Einstein condensation of ^{85}Rb by direct evaporation in an optical

dipole trap," *Physical Review A*, vol. 85, no. 5, p. 053647, May 2012. [Online]. Available: http://link.aps.org/doi/10.1103/PhysRevA.85.053647 12

[37] J. L. Roberts, N. R. Claussen, J. P. Burke, C. H. Greene, E. A. Cornell, and C. E. Wieman, "Resonant magnetic field control of elastic scattering in cold ^{85}Rb," *Physical Review Letters*, vol. 81, no. 23, p. 5109, Dec. 1998. [Online]. Available: http://link.aps.org/doi/10.1103/PhysRevLett.81.5109 12

[38] A. Marte, T. Volz, J. Schuster, S. Dürr, G. Rempe, E. van Kempen, and B. Verhaar, "Feshbach resonances in rubidium 87: Precision measurement and analysis," *Physical Review Letters*, vol. 89, no. 28, p. 283202, Dec. 2002. [Online]. Available: http://link.aps.org/doi/10.1103/PhysRevLett.89.283202 12

[39] Y. Takasu, K. Maki, K. Komori, T. Takano, K. Honda, M. Kumakura, T. Yabuzaki, and Y. Takahashi, "Spin-singlet Bose-Einstein condensation of two-electron atoms," *Physical Review Letters*, vol. 91, no. 4, p. 040404, Jul. 2003. [Online]. Available: http://link.aps.org/doi/10.1103/PhysRevLett.91.040404 13

[40] C. J. Bowers, "Experimental investigation of the $6s_2\ ^1S_0$—$5d6s\ ^3D_1$ forbidden transition in atomic ytterbium," PhD, University of California at Berkeley, 1998. 13

[41] K. Honda, Y. Takahashi, T. Kuwamoto, M. Fujimoto, K. Toyoda, K. Ishikawa, and T. Yabuzaki, "Magneto-optical trapping of Yb atoms and a limit on the branching ratio of the $^1P_1$ state," *Physical Review A*, vol. 59, no. 2, p. R934, Feb. 1999. [Online]. Available: http://link.aps.org/doi/10.1103/PhysRevA.59.R934 13

[42] T. Kuwamoto, K. Honda, Y. Takahashi, and T. Yabuzaki, "Magneto-optical trapping of Yb atoms using an intercombination transition," *Physical Review A*, vol. 60, no. 2, p. R745, Aug. 1999. [Online]. Available: http://link.aps.org/doi/10.1103/PhysRevA.60.R745 13

[43] C. Bowers, D. Budker, E. Commins, D. DeMille, S. Freedman, A.-T. Nguyen, S.-Q. Shang, and M. Zolotorev, "Experimental investigation of excited-state lifetimes in atomic ytterbium," *Physical Review A*, vol. 53, no. 5, p. 3103, May 1996. [Online]. Available: http://link.aps.org/doi/10.1103/PhysRevA.53.3103 13

[44] R. Maruyama, R. Wynar, M. Romalis, A. Andalkar, M. Swallows, C. Pearson, and E. Fortson, "Investigation of sub-Doppler cooling in an ytterbium magneto-optical trap," *Physical Review A*, vol. 68, no. 1, p. 011403, Jul. 2003. [Online]. Available: http://link.aps.org/doi/10.1103/PhysRevA.68.011403 14

[45] X. Xu, T. Loftus, J. Dunn, C. Greene, J. Hall, A. Gallagher, and J. Ye, "Single-stage sub-Doppler cooling of alkaline earth atoms," *Physical*

Review Letters, vol. 90, no. 19, p. 193002, May 2003. [Online]. Available: http://link.aps.org/doi/10.1103/PhysRevLett.90.193002 14

[46] T. Fukuhara, Y. Takasu, M. Kumakura, and Y. Takahashi, "Degenerate Fermi gases of ytterbium," *Physical Review Letters*, vol. 98, no. 3, p. 030401, Jan. 2007. [Online]. Available: http://link.aps.org/doi/10.1103/PhysRevLett.98.030401 14

[47] K. Enomoto, K. Kasa, M. Kitagawa, and Y. Takahashi, "Optical Feshbach resonance using the intercombination transition," *Physical Review Letters*, vol. 101, no. 20, p. 203201, Nov. 2008. [Online]. Available: http://link.aps.org/doi/10.1103/PhysRevLett.101.203201 14

[48] A. Yamaguchi, S. Uetake, D. Hashimoto, J. Doyle, and Y. Takahashi, "Inelastic collisions in optically trapped ultracold metastable ytterbium," *Physical Review Letters*, vol. 101, no. 23, p. 233002, Dec. 2008. [Online]. Available: http://link.aps.org/doi/10.1103/PhysRevLett.101.233002 14

[49] Y. Takasu and Y. Takahashi, "Quantum degenerate gases of ytterbium atoms," *Journal of the Physical Society of Japan*, vol. 78, no. 1, p. 012001, Jan. 2009. [Online]. Available: http://journals.jps.jp/doi/abs/10.1143/JPSJ.78.012001 14

[50] T. Fukuhara, S. Sugawa, Y. Takasu, and Y. Takahashi, "All-optical formation of quantum degenerate mixtures," *Physical Review A*, vol. 79, no. 2, p. 021601, Feb. 2009. [Online]. Available: http://link.aps.org/doi/10.1103/PhysRevA.79.021601 14

[51] S. Sugawa, R. Yamazaki, S. Taie, and Y. Takahashi, "Bose-Einstein condensate in gases of rare atomic species," *Physical Review A*, vol. 84, no. 1, p. 011610, Jul. 2011. [Online]. Available: http://link.aps.org/doi/10.1103/PhysRevA.84.011610 14

[52] N. Lemke, A. Ludlow, Z. Barber, T. Fortier, S. Diddams, Y. Jiang, S. Jefferts, T. Heavner, T. Parker, and C. Oates, "Spin-1/2 optical lattice clock," *Physical Review Letters*, vol. 103, no. 6, p. 063001, Aug. 2009. [Online]. Available: http://link.aps.org/doi/10.1103/PhysRevLett.103.063001 14

[53] Y. Y. Jiang, A. D. Ludlow, N. D. Lemke, R. W. Fox, J. A. Sherman, L.-S. Ma, and C. W. Oates, "Making optical atomic clocks more stable with 10^{16}-level laser stabilization," *Nature Photonics*, vol. 5, no. 3, p. 158, Jan. 2011. [Online]. Available: http://www.nature.com/doifinder/10.1038/nphoton.2010.313 14

[54] N. Hinkley, J. A. Sherman, N. B. Phillips, M. Schioppo, N. D. Lemke, K. Beloy, M. Pizzocaro, C. W. Oates, and A. D. Ludlow, "An atomic clock with 10^{-18} instability," *Science*, vol. 341, no. 6151, p. 1215, Sep. 2013. [Online]. Available: http://www.ncbi.nlm.nih.gov/pubmed/23970562 14

[55] K. Pandey, K. D. Rathod, A. K. Singh, and V. Natarajan, "Atomic fountain of laser-cooled Yb atoms for precision measurements," *Physical Review A*, vol. 82, no. 4, p. 043429, Oct. 2010. [Online]. Available: http://link.aps.org/doi/10.1103/PhysRevA.82.043429 14

[56] A. Singh, D. Angom, and V. Natarajan, "Observation of the nuclear magnetic octupole moment of ^{173}Yb from precise measurements of the hyperfine structure in the $^3P_2$ state," *Physical Review A*, vol. 87, no. 1, p. 012512, Jan. 2013. [Online]. Available: http://link.aps.org/doi/10.1103/PhysRevA.87.012512 14

[57] K. D. Rathod, A. K. Singh, and V. Natarajan, "Continuous beam of laser-cooled Yb atoms," *Europhysics Letters*, vol. 102, no. 4, p. 43001, May 2013. [Online]. Available: http://stacks.iop.org/0295-5075/102/i=4/a=43001 14

[58] A. H. Hansen, A. Khramov, W. H. Dowd, A. O. Jamison, V. V. Ivanov, and S. Gupta, "Quantum degenerate mixture of ytterbium and lithium atoms," *Physical Review A*, vol. 84, no. 1, p. 011606, Jul. 2011. [Online]. Available: http://link.aps.org/doi/10.1103/PhysRevA.84.011606 14

[59] V. V. Ivanov, A. Khramov, A. H. Hansen, W. H. Dowd, F. Münchow, A. O. Jamison, and S. Gupta, "Sympathetic cooling in an optically trapped mixture of alkali and spin-singlet atoms," *Physical Review Letters*, vol. 106, no. 15, p. 153201, Apr. 2011. [Online]. Available: http://link.aps.org/doi/10.1103/PhysRevLett.106.153201 14

[60] A. Y. Khramov, A. H. Hansen, A. O. Jamison, W. H. Dowd, and S. Gupta, "Dynamics of Feshbach molecules in an ultracold three-component mixture," *Physical Review A*, vol. 86, no. 3, p. 032705, Sep. 2012. [Online]. Available: http://link.aps.org/doi/10.1103/PhysRevA.86.032705 14

[61] A. Hansen, A. Khramov, W. Dowd, A. Jamison, B. Plotkin-Swing, R. Roy, and S. Gupta, "Production of quantum-degenerate mixtures of ytterbium and lithium with controllable interspecies overlap," *Physical Review A*, vol. 87, no. 1, p. 013615, Jan. 2013. [Online]. Available: http://link.aps.org/doi/10.1103/PhysRevA.87.013615 14

[62] A. Khramov, A. Hansen, W. Dowd, R. J. Roy, C. Makrides, A. Petrov, S. Kotochigova, and S. Gupta, "Ultracold heteronuclear mixture of ground and excited state atoms," *Physical Review Letters*, vol. 112, no. 3, p. 033201, Jan. 2014. [Online]. Available: http://link.aps.org/doi/10.1103/PhysRevLett.112.033201 14

[63] S. Dörscher, A. Thobe, B. Hundt, A. Kochanke, R. Le Targat, P. Windpassinger, C. Becker, and K. Sengstock, "Creation of quantum-degenerate gases of ytterbium in a compact 2D-/3D-magneto-optical trap

setup," *The Review of Scientific Instruments*, vol. 84, no. 4, p. 043109, Apr. 2013. [Online]. Available: http://www.ncbi.nlm.nih.gov/pubmed/23635183 14

[64] L. Viverit, C. Pethick, and H. Smith, "Zero-temperature phase diagram of binary boson-fermion mixtures," *Physical Review A*, vol. 61, no. 5, p. 053605, Apr. 2000. [Online]. Available: http://link.aps.org/doi/10.1103/PhysRevA.61.053605 15, 16, 17

[65] W. Ketterle, D. S. Durfee, and D. M. Stamper-Kurn, "Making, probing and understanding Bose-Einstein condensates," Apr. 1999. [Online]. Available: http://arxiv.org/abs/cond-mat/9904034 16, 95

[66] F. Riboli and M. Modugno, "Topology of the ground state of two interacting Bose-Einstein condensates," *Physical Review A*, vol. 65, no. 6, p. 063614, Jun. 2002. [Online]. Available: http://link.aps.org/doi/10.1103/PhysRevA.65.063614 16

[67] D. Jezek and P. Capuzzi, "Interaction-driven effects on two-component Bose-Einstein condensates," *Physical Review A*, vol. 66, no. 1, p. 015602, Jul. 2002. [Online]. Available: http://link.aps.org/doi/10.1103/PhysRevA.66.015602 16

[68] A. Sartori and A. Recati, "Dynamics of highly unbalanced Bose-Bose mixtures: miscible vs. immiscible gases," *The European Physical Journal D*, vol. 67, no. 12, p. 260, Dec. 2013. [Online]. Available: http://link.springer.com/10.1140/epjd/e2013-40635-x 16

[69] G. Modugno, G. Roati, F. Riboli, F. Ferlaino, R. J. Brecha, and M. Inguscio, "Collapse of a degenerate Fermi gas," *Science*, vol. 297, no. 5590, p. 2240, Sep. 2002. [Online]. Available: http://www.ncbi.nlm.nih.gov/pubmed/12202686 18, 19

[70] K. Mølmer, "Bose Condensates and Fermi gases at zero temperature," *Physical Review Letters*, vol. 80, no. 9, p. 1804, Mar. 1998. [Online]. Available: http://link.aps.org/doi/10.1103/PhysRevLett.80.1804 18

[71] K. Kasamatsu and M. Tsubota, "Static and dynamic properties of multicomponent Bose-Einstein condensates of ytterbium atoms," *Journal of Low Temperature Physics*, vol. 150, no. 3-4, p. 599, Nov. 2007. [Online]. Available: http://link.springer.com/10.1007/s10909-007-9600-x 18

[72] P. Ruprecht, M. Holland, K. Burnett, and M. Edwards, "Time-dependent solution of the nonlinear schrödinger equation for bose-condensed trapped neutral atoms," *Physical Review A*, vol. 51, no. 6, p. 4704, Jun. 1995. [Online]. Available: http://link.aps.org/doi/10.1103/PhysRevA.51.4704 18

[73] A. Mosk, S. Kraft, M. Mudrich, K. Singer, W. Wohlleben, R. Grimm, and M. Weidemüller, "Mixture of ultracold lithium and cesium atoms in an

optical dipole trap," *Applied Physics B*, vol. 73, no. 8, p. 791, Mar. 2014. [Online]. Available: http://link.springer.com/10.1007/s003400100743 20, 21

[74] G. Delannoy, S. Murdoch, V. Boyer, V. Josse, P. Bouyer, and A. Aspect, "Understanding the production of dual Bose-Einstein condensation with sympathetic cooling," *Physical Review A*, vol. 63, no. 5, p. 051602, Apr. 2001. [Online]. Available: http://link.aps.org/doi/10.1103/PhysRevA.63.051602 20

[75] H. Wu and C. J. Foot, "Direct simulation of evaporative cooling," *Journal of Physics B: Atomic, Molecular and Optical Physics*, vol. 29, no. 8, p. L321, Apr. 1996. [Online]. Available: http://stacks.iop.org/0953-4075/29/i=8/a=003 20

[76] D. Snoke and J. Wolfe, "Population dynamics of a Bose gas near saturation," *Physical Review B*, vol. 39, no. 7, p. 4030, Mar. 1989. [Online]. Available: http://link.aps.org/doi/10.1103/PhysRevB.39.4030 20

[77] C. R. Monroe, E. A. Cornell, C. A. Sackett, C. J. Myatt, and C. E. Wieman, "Measurement of Cs-Cs elastic scattering at T=30 μK," *Physical Review Letters*, vol. 70, no. 4, p. 414, Jan. 1993. [Online]. Available: http://link.aps.org/doi/10.1103/PhysRevLett.70.414 20

[78] M. Arndt, M. Ben Dahan, D. Guéry-Odelin, M. Reynolds, and J. Dalibard, "Observation of a zero-energy resonance in Cs-Cs collisions," *Physical Review Letters*, vol. 79, no. 4, p. 625, Jul. 1997. [Online]. Available: http://link.aps.org/doi/10.1103/PhysRevLett.79.625 20

[79] T. Arpornthip, C. A. Sackett, and K. J. Hughes, "Vacuum-pressure measurement using a magneto-optical trap," *Physical Review A*, vol. 85, no. 3, p. 033420, Mar. 2012. [Online]. Available: http://link.aps.org/doi/10.1103/PhysRevA.85.033420 23

[80] P. L. Gould, G. A. Ruff, and D. E. Pritchard, "Diffraction of atoms by light: The near-resonant Kapitza-Dirac effect," *Physical Review Letters*, vol. 56, no. 8, p. 827, Feb. 1986. [Online]. Available: http://link.aps.org/doi/10.1103/PhysRevLett.56.827 29

[81] H. C. W. Beijerinck and N. F. Verster, "Velocity distribution and angular distribution of molecular beams from multichannel arrays," *Journal of Applied Physics*, vol. 46, no. 5, p. 2083, Sep. 1975. [Online]. Available: http://scitation.aip.org/content/aip/journal/jap/46/5/10.1063/1.321845 36

[82] D. J. Croucher and J. L. Clark, "Total collision cross sections and van der Waals constants for alkali atom interactions with atoms and non-reactive diatomic molecules at thermal energies," *Journal of Physics B: Atomic and Molecular Physics*, vol. 2, no. 5, p. 603, May 1969. [Online]. Available: http://iopscience.iop.org/0022-3700/2/5/313 36

[83] C. Lucas, "The production of intense atomic beams," *Vacuum*, vol. 23, no. 11, p. 395, Nov. 1973. [Online]. Available: http://www.sciencedirect.com/science/article/B6TW4-46WX5PK-2/2/dbe5beba36619187d6b9d5983d7d2eea 36

[84] W. Phillips and H. Metcalf, "Laser deceleration of an atomic beam," *Physical Review Letters*, vol. 48, no. 9, p. 596, Mar. 1982. [Online]. Available: http://link.aps.org/doi/10.1103/PhysRevLett.48.596 40, 41

[85] T. Tiecke, S. Gensemer, A. Ludewig, and J. Walraven, "High-flux two-dimensional magneto-optical-trap source for cold lithium atoms," *Physical Review A*, vol. 80, no. 1, p. 013409, Jul. 2009. [Online]. Available: http://link.aps.org/doi/10.1103/PhysRevA.80.013409 44

[86] S. E. Dörscher, "Creation of ytterbium quantum gases with a compact 2D-/3D-MOT setup," PhD, Hamburg, 2013. 46, 47

[87] L. P. Maguire, S. Szilagyi, and R. E. Scholten, "High performance laser shutter using a hard disk drive voice-coil actuator," *Review of Scientific Instruments*, vol. 75, no. 9, p. 3077, Sep. 2004. [Online]. Available: http://scitation.aip.org/content/aip/journal/rsi/75/9/10.1063/1.1786331 55

[88] X. Baillard, A. Gauguet, S. Bize, P. Lemonde, P. Laurent, A. Clairon, and P. Rosenbusch, "Interference-filter-stabilized external-cavity diode lasers," *Optics Communications*, vol. 266, no. 2, p. 609, Oct. 2006. [Online]. Available: http://linkinghub.elsevier.com/retrieve/pii/S0030401806004561 62

[89] M. Gilowski, C. Schubert, M. Zaiser, W. Herr, T. Wübbena, T. Wendrich, T. Müller, E. Rasel, and W. Ertmer, "Narrow bandwidth interference filter-stabilized diode laser systems for the manipulation of neutral atoms," *Optics Communications*, vol. 280, no. 2, p. 443, Dec. 2007. [Online]. Available: http://linkinghub.elsevier.com/retrieve/pii/S0030401807008577 62

[90] N. Nemitz, "Production and spectroscopy of ultracold YbRb* molecules," PhD, Heinrich-Heine-Universität Düsseldorf, 2008. [Online]. Available: http://docserv.uni-duesseldorf.de/servlets/DocumentServlet?id=10202 79

[91] R. Grimm, M. Weidemüller, and Y. B. Ovchinnikov, "Optical dipole traps for neutral atoms," *Advances in Atomic, Molecular, and Optical Physics*, vol. 42, p. 95, Feb. 1999. [Online]. Available: http://arxiv.org/abs/physics/9902072 81

[92] J. Mitroy, M. S. Safronova, and C. W. Clark, "Theory and applications of atomic and ionic polarizabilities," *Journal of Physics B: Atomic, Molecular and Optical Physics*, vol. 43, no. 20, p. 202001, Oct. 2010. [Online]. Available: http://stacks.iop.org/0953-4075/43/i=20/a=202001 81, 124

[93] C. D. Herold, V. D. Vaidya, X. Li, S. L. Rolston, J. V. Porto, and M. S. Safronova, "Precision measurement of transition matrix elements via light shift

cancellation," *Physical Review Letters*, vol. 109, no. 24, p. 243003, Dec. 2012. [Online]. Available: http://link.aps.org/doi/10.1103/PhysRevLett.109.243003 106, 115, 125

[94] K. Beloy, J. A. Sherman, N. D. Lemke, N. Hinkley, C. W. Oates, and A. D. Ludlow, "Determination of the 5d6s $^3D_1$ state lifetime and blackbody-radiation clock shift in Yb," *Physical Review A*, vol. 86, no. 5, p. 051404, Nov. 2012. [Online]. Available: http://link.aps.org/doi/10.1103/PhysRevA.86.051404 106, 125

[95] J. A. Sherman, N. D. Lemke, N. Hinkley, M. Pizzocaro, R. W. Fox, A. D. Ludlow, and C. W. Oates, "High-accuracy measurement of atomic polarizability in an optical lattice clock," *Physical Review Letters*, vol. 108, no. 15, p. 153002, Apr. 2012. [Online]. Available: http://link.aps.org/doi/10.1103/PhysRevLett.108.153002 106, 107

[96] S. Porsev, A. Ludlow, M. Boyd, and J. Ye, "Determination of Sr properties for a high-accuracy optical clock," *Physical Review A*, vol. 78, no. 3, p. 032508, Sep. 2008. [Online]. Available: http://link.aps.org/doi/10.1103/PhysRevA.78.032508 106

[97] S. G. Porsev, K. Beloy, and A. Derevianko, "Precision determination of electroweak coupling from atomic parity violation and implications for particle physics," *Physical Review Letters*, vol. 102, no. 18, p. 181601, May 2009. [Online]. Available: http://link.aps.org/doi/10.1103/PhysRevLett.102.181601 106, 107

[98] A. Vasilyev, I. Savukov, M. Safronova, and H. Berry, "Measurement of the 6s-7p transition probabilities in atomic cesium and a revised value for the weak charge Q_W," *Physical Review A*, vol. 66, no. 2, p. 020101, Aug. 2002. [Online]. Available: http://link.aps.org/doi/10.1103/PhysRevA.66.020101 106, 107

[99] M. S. Safronova, U. I. Safronova, and C. W. Clark, "Magic wavelengths for optical cooling and trapping of lithium," *Physical Review A*, vol. 86, no. 4, p. 042505, Oct. 2012. [Online]. Available: http://link.aps.org/doi/10.1103/PhysRevA.86.042505 106

[100] A. Gorshkov, A. Rey, A. Daley, M. Boyd, J. Ye, P. Zoller, and M. Lukin, "Alkaline-earth-metal atoms as few-qubit quantum registers," *Physical Review Letters*, vol. 102, no. 11, p. 110503, Mar. 2009. [Online]. Available: http://link.aps.org/doi/10.1103/PhysRevLett.102.110503 106

[101] M. Saffman and T. Walker, "Analysis of a quantum logic device based on dipole-dipole interactions of optically trapped Rydberg atoms," *Physical Review A*, vol. 72, no. 2, p. 022347, Aug. 2005. [Online]. Available: http://link.aps.org/doi/10.1103/PhysRevA.72.022347 106

[102] H. P. Summers, N. R. Badnell, M. G. O'Mullane, A. D. Whiteford, R. Bingham, B. J. Kellett, J. Lang, K. H. Behringer, U. Fantz, K.-D. Zastrow, S. D. Loch, M. S. Pindzola, D. C. Griffin, and C. P. Ballance, "Atomic data for modelling fusion and astrophysical plasmas," *Plasma Physics and Controlled Fusion*, vol. 44, no. 12B, p. B323, Dec. 2002. [Online]. Available: http://stacks.iop.org/0741-3335/44/i=12B/a=323 106

[103] D. Verner, E. Verner, and G. Ferland, "Atomic data for permitted resonance lines of atoms and ions from H to Si, and S, Ar, Ca, and Fe," *Atomic Data and Nuclear Data Tables*, vol. 64, no. 1, p. 1, Sep. 1996. [Online]. Available: http://linkinghub.elsevier.com/retrieve/pii/S0092640X96900182 106

[104] J. Pickering, R. Blackwell-Whitehead, A. Thorne, M. Ruffoni, and C. Holmes, "Laboratory measurements of oscillator strengths and their astrophysical applications," *Canadian Journal of Physics*, vol. 89, no. 4, p. 387, Apr. 2011. [Online]. Available: http://www.nrcresearchpress.com/doi/abs/10.1139/p11-044 106

[105] M. S. Safronova, M. G. Kozlov, and C. W. Clark, "Precision calculation of blackbody radiation shifts for optical frequency metrology," *Physical Review Letters*, vol. 107, no. 14, p. 143006, Sep. 2011. [Online]. Available: http://link.aps.org/doi/10.1103/PhysRevLett.107.143006 106

[106] S. Porsev and A. Derevianko, "Multipolar theory of blackbody radiation shift of atomic energy levels and its implications for optical lattice clocks," *Physical Review A*, vol. 74, no. 2, p. 020502, Aug. 2006. [Online]. Available: http://link.aps.org/doi/10.1103/PhysRevA.74.020502 106

[107] K. Aikawa, A. Frisch, M. Mark, S. Baier, A. Rietzler, R. Grimm, and F. Ferlaino, "Bose-Einstein condensation of erbium," *Physical Review Letters*, vol. 108, no. 21, p. 210401, May 2012. [Online]. Available: http://link.aps.org/doi/10.1103/PhysRevLett.108.210401 107

[108] M. Lu, N. Q. Burdick, and B. L. Lev, "Quantum degenerate dipolar Fermi gas," *Physical Review Letters*, vol. 108, no. 21, p. 215301, May 2012. [Online]. Available: http://link.aps.org/doi/10.1103/PhysRevLett.108.215301 107

[109] M. Saffman and K. Mølmer, "Scaling the neutral-atom Rydberg gate quantum computer by collective encoding in holmium atoms," *Physical Review A*, vol. 78, no. 1, p. 012336, Jul. 2008. [Online]. Available: http://link.aps.org/doi/10.1103/PhysRevA.78.012336 107

[110] N. Bouloufa, A. Crubellier, and O. Dulieu, "Photoassociative molecular spectroscopy for atomic radiative lifetimes," *Physica Scripta*, vol. T134, no. T134, p. 014014, May 2009. [Online]. Available: http://stacks.iop.org/1402-4896/2009/i=T134/a=014014 107

[111] E. Gomez, S. Aubin, L. A. Orozco, and G. D. Sprouse, "Lifetime and hyperfine splitting measurements on the 7s and 6p levels in rubidium," *Journal of the Optical Society of America B*, vol. 21, no. 11, p. 2058, Nov. 2004. [Online]. Available: http://www.opticsinfobase.org/abstract.cfm?URI=josab-21-11-2058 107

[112] J. Sherman, T. Koerber, A. Markhotok, W. Nagourney, and E. Fortson, "Precision measurement of light shifts in a single trapped Ba^+ ion," *Physical Review Letters*, vol. 94, no. 24, p. 243001, Jun. 2005. [Online]. Available: http://link.aps.org/doi/10.1103/PhysRevLett.94.243001 107

[113] J. Sherman, A. Andalkar, W. Nagourney, and E. Fortson, "Measurement of light shifts at two off-resonant wavelengths in a single trapped Ba^+ ion and the determination of atomic dipole matrix elements," *Physical Review A*, vol. 78, no. 5, p. 052514, Nov. 2008. [Online]. Available: http://link.aps.org/doi/10.1103/PhysRevA.78.052514 107

[114] B. Sahoo, L. Wansbeek, K. Jungmann, and R. Timmermans, "Light shifts and electric dipole matrix elements in Ba^+ and Ra^+," *Physical Review A*, vol. 79, no. 5, p. 052512, May 2009. [Online]. Available: http://link.aps.org/doi/10.1103/PhysRevA.79.052512 107

[115] B. Arora, M. S. Safronova, and C. W. Clark, "Tune-out wavelengths of alkali-metal atoms and their applications," *Physical Review A*, vol. 84, no. 4, p. 043401, Oct. 2011. [Online]. Available: http://link.aps.org/doi/10.1103/PhysRevA.84.043401 108, 115, 118, 124

[116] M. Takamoto, F.-L. Hong, R. Higashi, and H. Katori, "An optical lattice clock," *Nature*, vol. 435, no. 7040, p. 321, May 2005. [Online]. Available: http://dx.doi.org/10.1038/nature03541 108

[117] F. M. Izrailev and D. L. Shepelyanskii, "Quantum resonance for a rotator in a nonlinear periodic field," *Theoretical and Mathematical Physics*, vol. 43, no. 3, p. 553, Jun. 1980. [Online]. Available: http://link.springer.com/10.1007/BF01029131 110

[118] F. Moore, J. Robinson, C. Bharucha, B. Sundaram, and M. Raizen, "Atom optics realization of the quantum δ-kicked rotor," *Physical Review Letters*, vol. 75, no. 25, p. 4598, Dec. 1995. [Online]. Available: http://link.aps.org/doi/10.1103/PhysRevLett.75.4598 110

[119] S. Wu, Y.-J. Wang, Q. Diot, and M. Prentiss, "Splitting matter waves using an optimized standing-wave light-pulse sequence," *Physical Review A*, vol. 71, no. 4, p. 043602, Apr. 2005. [Online]. Available: http://link.aps.org/doi/10.1103/PhysRevA.71.043602 110, 113

[120] L. Deng, E. Hagley, J. Denschlag, J. Simsarian, M. Edwards, C. Clark, K. Helmerson, S. Rolston, and W. Phillips, "Temporal, matter-wave-dispersion

Talbot effect," *Physical Review Letters*, vol. 83, no. 26, p. 5407, Dec. 1999. [Online]. Available: http://link.aps.org/doi/10.1103/PhysRevLett.83.5407 110

[121] A. Shiner, A. Madej, P. Dubé, and J. Bernard, "Absolute optical frequency measurement of saturated absorption lines in Rb near 422 nm," *Applied Physics B*, vol. 89, no. 4, p. 595, Nov. 2007. [Online]. Available: http://link.springer.com/10.1007/s00340-007-2836-y 112

[122] I. H. Deutsch and P. S. Jessen, "Quantum control and measurement of atomic spins in polarization spectroscopy," *Optics Communications*, vol. 283, no. 5, p. 681, Mar. 2010. [Online]. Available: http://linkinghub.elsevier.com/retrieve/pii/S0030401809010517 113

[123] U. Volz and H. Schmoranzer, "Precision lifetime measurements on alkali atoms and on helium by beam-gas-laser spectroscopy," *Physica Scripta*, vol. T65, no. T65, p. 48, Jan. 1996. [Online]. Available: http://stacks.iop.org/1402-4896/1996/i=T65/a=007 115

[124] D. C. Morton, "Atomic Data for Resonance Absorption Lines. II. Wavelengths Longward of the Lyman Limit for Heavy Elements," *The Astrophysical Journal Supplement Series*, vol. 130, no. 2, p. 403, Oct. 2000. [Online]. Available: http://stacks.iop.org/0067-0049/130/i=2/a=403 125

[125] M. S. Safronova, S. G. Porsev, and C. W. Clark, "Ytterbium in quantum gases and atomic clocks: van der Waals interactions and blackbody shifts," *Physical Review Letters*, vol. 109, no. 23, p. 230802, Dec. 2012. [Online]. Available: http://link.aps.org/doi/10.1103/PhysRevLett.109.230802 125

[126] A. M. Rey, "Ultracold bosonic atoms in optical lattices," PhD, University of Maryland, 2004. [Online]. Available: http://hdl.handle.net/1903/1802 128